DISSERTATION

Design and Exploration of Radio Frequency Identification Systems by Rapid Prototyping

Conducted for the purpose of receiving the academic title
"Doktor der technischen Wissenschaften"

Submitted to the
Vienna University of Technology
Faculty of Electrical Engineering and Information Technology

by

Dipl.-Ing. Christoph Angerer
Schulgasse 86/5b, 1180 Wien
born in Linz, October 24th, 1980

July 27, 2010 .....

Advisor

Univ.Prof. Dipl.-Ing. Dr.techn. Markus Rupp
Vienna University of Technology
Institute of Communications and Radio-Frequency Engineering

Examiner

Prof. Dr.-Ing. Dr.-Ing. habil. Robert Weigel
University of Erlangen-Nürnberg
Institute for Electronics Engineering

to Katharina and Emil

ABSTRACT

In this thesis I describe the setup and design of a flexible rapid prototyping platform for RFID systems to provide an experimental verification environment for RFID systems, that allows their real-time exploration in distinct measurement setups. Furthermore, I use this system to test the feasibility of novel signal processing algorithms for RFID reader receivers, which promise a performance increase to state-of-the-art-receivers.

Three different scenarios are considered:

1. In the first scenario, a single tag communicates with a single receive antenna reader. The performance of the optimal maximum likelihood sequence decoder is identified, and losses due to channel estimation and synchronisation are discussed. Due to the wide deviation from the nominal data rate in the uplink communication, especially synchronisation shows to be a critical issue.

2. In the second scenario, the single tag communicates with a multiple receive antenna RFID reader. This multiple receive antenna system allows for mainly two advances: in a strong line of sight environment I demonstrate that a direction of arrival estimation of the tag signal is feasible, while for an environment with strong multipath components, I propose a maximum ratio combining for diversity combining at the reader receiver. Hence, in the line of sight case I address localisation of RFID tags, while the diversity combining addresses the topic of reliability of the communication in a high fading environment.

3. Finally, in the third scenario multiple tags communicate with the reader simultaneously and generate a collision. Such collisions are modeled on the physical layer, and different receivers with either a single or multiple receive antennas are proposed to recover from a collision at the physical layer. Hence, the topic of throughput in multiple tag communications is addressed here, which is shown to increase by a factor of 1.6 compared to the throughput of a conventional system, in the case a reader can recover from collisions of up to two tags. Moreover, performance tradeoffs regarding throughput, reliability and receiver complexity are shown.

For all three scenarios, models for the signal constellations at the reader receiver are developed and supported by measurement data. Implementation aspects of the receivers are discussed, and performance comparisons not only by means of simulations but also by measurements are presented.

ZUSAMMENFASSUNG

Die vorliegende Dissertation befasst sich mit dem Aufbau und Design einer flexiblen Rapid Prototyping Umgebung für RFID Systeme. Diese Testumgebung erlaubt die experimentelle Evaluierung von RFID Systemen sowie deren Erforschung in Echtzeit in verschiedenen Versuchsanordnungen. Zusätzlich wird diese Testumgebung benutzt, um neuartige Signalverarbeitungsalgorithmen für RFID Lesegeräte zu testen, welche eine Verbesserung der Leistungsfähigkeit von Empfängern versprechen.

Drei verschiedene Szenarien werden in dieser Dissertation betrachtet:

1. Das erste Szenario behandelt die Kommunikation eines einzelnen RFID Tags mit dem Lesegerät. Die Effizienz des optimalen Maximum-Likelihood Empfängers wird gezeigt und Verluste durch Kanalschätzung und Synchronisation werden diskutiert. Wegen der großen Abweichung von der nominalen Datenrate in der Tag-Reader Kommunikation zeigt sich, dass Synchronisation den kritischsten Aspekt im Empfängerdesign darstellt.

2. Im zweiten Szenario kommuniziert das RFID Tag mit einem Lesegerät mit mehreren Empfangsantennen. Das Verwenden mehrerer Empfangsantennen ermöglicht zwei Vorteile: Erstens zeigt die Dissertation, dass eine Richtungslokalisierung mit nur zwei Empfangsantennen am Lesegerät möglich ist, sofern der Übertragungskanal geringem Schwund ausgesetzt ist. Zweitens können mehrere Empfangsantennen in einer Umgebung, die stark von Mehrwegeausbreitung geprägt ist, für Diversitätsempfang benutzt werden. Dieses Szenario adressiert das wichtige Thema der Zuverlässigkeit von RFID Systemen in Schwundkanälen.

3. In einem dritten Szenario wird die gleichzeitige Kommunikation eines Lesegeräts mit mehreren RFID Tags untersucht. Solche Signalkollisionen werden modelliert, und verschieden Empfängerstrukturen werden entwickelt, um die einzelnen Signalkomponenten der Kollision separieren zu können. Dieses Thema adressiert den Datendurchsatz in RFID Systemen. Es wird gezeigt, dass ein Lesegerät, welches Kollisionen von zwei Tags auflösen kann, eine Datendurchsatzerhöhung um den Faktor 1,6 erreicht. Die Leistungsfähigkeit der einzelnen Empfänger wird gezeigt.

Für alle drei Szenarios wurden Modelle von Signalkonstellationen im Basisband des Lesegeräts entwickelt, welche auch durch Messdaten unterstützt werden. Implementierungsaspekte werden diskutiert, und die Leistungsfähigkeit wird in Simulation und Messung verglichen.

ACKNOWLEDGEMENT

First of all, I would like to express my gratitude to my advisor Markus Rupp for his support and encouragement regarding my research throughout the time I spent at the Vienna University of Technology, and for his supervision of my thesis. Likewise I thank Robert Weigel for agreeing to review the thesis and to serve as examiner in the defense of the thesis.

I greatly benefited from the fruitful discussions with my colleagues Robert Langwieser, María Victoria Bueno Delgado, Bastian Knerr, Martin Holzer, Lukas Mayer, Robert Dallinger, Gregor Lasser, Georg Maier and Mostafa Ibrahim. They provided an atmosphere for profitable scientific exchange, and introduced me in related topics of this thesis.

Furthermore, I thank Infineon Technologies for their enduring support. Especially, I want to mention Thomas Herndl for his suggestive input during the past years.

With some rock evenings apart from the scientific life at the university, my colleagues of the institute's band always provided a welcoming diversion.

This work has been funded by the Christian Doppler Laboratory for Wireless Technologies for Sustainable Mobility, and the Christian Doppler Laboratory for Design Methodology of Signal Processing Alogrithms, headed by Christoph Mecklenbräuker and Markus Rupp, respectively.

CONTENTS

1 INTRODUCTION

1.1 An Overview of State-of-the-Art RFID Systems

At the time of writing this thesis, Radio Frequency Identification (RFID) is a very fast emerging technology for applications demanding identification or tracking of goods. Clearly, for human beings it is simple to recognise a certain object amongst others, for instance a certain bar of chocolate in a rack of a supermarket. For machines on the other hand such an identification is a severe problem, so that RFID can be viewed as a means of "perception" of the surrounding of computing devices. In contrast to other identification technologies, such as the magnetic strip or the bar code, no line of sight connection is required to identify an item, and multiple goods can be inventoried almost simultaneously. Its potential for various applications in the field of identification or tracking of items, that in general is logistics, is very promising [1–3]. Many of such applications have already been realised [4], as for instance document tracking and identification (in electronic passports or automated library systems [5–7]), road tolling [8], access control applications, animal tracking [9] or manufacturing line applications [10], just to name a view.

In a basic RFID system, we distinguish between RFID readers (also called interrogators), RFID tags (also called transponders) and the RFID middleware, which provides high level interfaces to applications and databases and an abstraction of the underlying physical equipment. Furthermore, we distinguish between active, semi-active and passive RFID systems, depending on whether the RFID tag is equipped with its own power supply and by the communication technology. In passive RFID systems, the tags receive the energy needed for processing from an electromagnetic field provided by the reader. The advantage of passive RFID systems is that tags are low cost and that they do not need to be recharged if their battery is empty. In both, semi-passive and passive systems, data transmission from the tag to the reader is achieved by a backscatter or load modulation. These modulations rely on the principle of either absorbing or reflecting power at the RFID tags by matching or unmatching the antenna to the input impedance of the transponder applying a so called shunt transistor [11–13]. The idea of communication by means of reflected power, dates back to 1948, when it first was proposed by H. Stockman [14].

RFID systems are operated in various frequency bands: In the low frequency (LF) domain at around 125 kHz and in the high frequency (HF) domain at 13.56 MHz passive tags are coupled with the reader via a dominantly magnetic field, and transmit information to the reader by a load modulation technique. The ultra high frequency (UHF) domain operates in the band of 860-960 MHz. Here, the RFID tags utilise backscatter modulation for

	LF	HF	UHF	Microwave
Frequency Domain	125-134 kHz	13.56 MHz	860-950 MHz	2.45-5.8 GHz
Read Range	10 cm	1 m	2-7 m	1m
Standards	ISO 14223	ISO 14443, ISO 15693, EPCglobal	ISO 18000-6, EPCglobal C1G2	ISO 18000-4 (withdrawn), ISO 18000-5
Applications	Smart ticketing, animal tagging, laundry, access control	transportation, libraries, access control, anti-theft	libraries, supply chain, road tolling	supply chain, security

Table 1.1: RFID system classification into frequency domains, read range, standards and applications.

communication [15]. Finally, RFID has been extended to the microwave band at 2.4 and 5.8 GHz [16]. In each of those many frequency bands several different standards have emerged (see Table 1.1).

In the quest of low cost and extremely low power consumption, passive RFID tags exhibit relatively limited computational complexity. They essentially consist of a shunt transistor to short-circuit the antenna, a rectifier, a demodulation circuit, a voltage supply circuit comprising an accumulation of capacitors to store energy, a digital control circuit and a small on-chip memory. While only a limited amount of user data is stored on the tag itself, its main purpose is to return its unique identifier upon request of RFID readers. This unique identifier (for example up to 496 bits [17]) then serves as a pointer to a database entry. The UHF tag NXP UCODE G2XM [18] e.g provides a 240 bit identifier, exhibits 512 bits of user memory, and requires -15 dBm of operating power. The Hitachi Mu Chip [19] operates at 2.45 GHz and follows a proprietary standard. Its dimension is only $0.4 \times 0.4 \times 0.06$ mm.

While RFID tags adhere to minimal functionality, the signal processing complexity is shifted to RFID readers. Several RFID reader manufacturers who offer products in the UHF domain, such as Kathrein [20] make use of the integrated baseband transceiver chips of Impinj [21], Austria Mircrosystems [22] or WJ Communications [23]. Their products hence only differ in RF sections, interfaces or the intended application domain, while a few manufacturers (as for instance Feig electronics [24]) also develop digital baseband signal processing.

1.2 Motivation

While many RFID applications have already been established in practice, the potential of this technology envisions even many more applications in the fields of logistics. These include for instance automated parcel tracking services, automatic inventory of whole cargo containers filled with different goods, identification of products in an assembly

line, automated identification of products of a customer in a shop at the cash desk, or in general tracking of goods throughout the entire supply chain. Such applications could enormously facilitate logistic processes and make them by far more efficient. However, the provided performance of current RFID technology still lacks behind the demands on high data rates, large readout ranges and especially high reliability. A multitude of problems still exists in making RFID ubiquitous in our every day life.

1.2.1 Compatibility of Present-Day RFID Systems

The different RFID technologies, whether active, semi-active and passive together with the various frequency bands and the variety of RFID standards lead to compatibility and interoperability issues of today's RFID systems. Furthermore, regional radio regulation policies complicate the design of a system that is globally functional. Currently, RFID equipment is often developed to support one specific application in a certain frequency domain following one particular standard. This makes the equipment improper for other RFID applications. The challenge of untangling these compatibility issues and designing a *one fits all* RFID equipment hence is of major interest and will drive future RFID technology [25–28].

1.2.2 Exploration of System Parameters

Today's RFID technology however is not yet ready for such a general purpose RFID equipment and lacks behind the market demands. Typical goals for such a general purpose system are high reliability, high data throughput, large readout distance, efficient communication in multi-tag scenarios, full performance in various different environments and full functionality, independent on the characteristics of the objects the tags are attached to [29–32]. In order to further push technology forward, detailed understanding of the dependency of these design goals on various system parameters is essential. Such system parameters include modulation schemes and encoding parameters or hardware configurations, like the antenna decoupling concept or the adjusted transmit power. Moreover, in depth knowledge about the mutual impact of the design goals and the available tradeoffs is fundamental. Important issues are for example tradeoffs between data rate, readout distance and reliability.

1.2.3 The Venture of Novel Technological Frontiers

Newly introduced wireless technologies and concepts in general, and especially RFID technology in particular, potentially hide unforeseen challenges due to a lack of experience on implementation and behavior in realistic scenarios. Consider for example the wireless channel in RFID systems, that only recently has been described by models for multiple antennas in [33, 34], but has hardly been investigated experimentally. The missing experience with such novel technologies hampers the development of high performance RFID systems. In order to establish multiple antenna algorithms in RFID, a thorough evaluation and a detailed exploration of such novel concepts is strongly desired in an experimental setup. With an advanced progression in the design, the penalty of

discovering a wrong design decision or an error in the drafted concept dramatically increases [35]. Hence an exploration of the envisioned system early in the design process strongly reduces the risk of such a conceptual error. This is true for new algorithms (such as beamforming or anti-collision algorithms), as well as for new hardware designs. In order to gain experience with a novel technology, the envisioned algorithms need to be studied in depth not only in simulations, but also in real-time experiments. Furthermore, as implementation of new algorithms in hardware lacks the experience of the design teams, an exploration of various design alternatives is of major interest for achieving the desired functionality in an implementation.

1.2.4 Dealing with Increased Complexity

In order to meet the high demands on technological performance for future RFID equipment, complex signal processing techniques are required. Such techniques include for example beamforming, higher order modulation schemes, complex anti-collision algorithms and tag population estimators or channel estimation algorithms at RFID readers. With the rising complexity of the signal processing algorithms, naturally also the complexity of the implementation increases.

The demands and advantages of a general purpose RFID equipment have been pointed out. In order to tackle the increasing complexity, to fully explore the physical characteristics of RFID systems and their parameters, and to design general purpose RFID systems, researchers aim for a highly flexible and configurable test environment. Such a system should permit to rapidly rate various system architectures and their behavior under real world conditions, as well as to detect influences of implementation details. To keep up with this growing challenges in implementing prototypes and the stringent time constraints for bringing a product on the market the design paradigms have changed towards rapid prototyping in wireless systems [36]. Conventional design methods are often time consuming and do not offer the possibility to explore the new system a designer has in mind in different configurations. Rapid prototyping on the other hand allows for a fast turnaround from simulation to real-time experiments by means of a highly automated design flow.

Thus, the scope of this thesis is to explore novel signal processing concepts for RFID readers by means of an experimental test platform. Performance benchmarks of various RFID reader receiver architectures are compared not only by simulation, but also by measurements. In order to facilitate the generation of meaningful experimental results, an automated design flow for the configuration of the established rapid prototyping platform is shown. The rapid prototyping system supports two frequency domains and multiple RFID standards to tackle interoperability issues. System parameters like transmit power, modulation and encoding settings or data rates are fully accessible and hence the system is perfectly suited for exploring their interdependency and influence on other performance goals, like data throughput or readout reliability. Finally, the thesis focuses on the establishment of multiple antenna techniques such as diversity receivers or spa-

tial multi-tag communication. Performance benchmarks of these novel techniques are provided on basis of measurement data.

1.3 The Concept of Rapid Prototyping

As pointed out, test environments for both, exploring physical parameters as well as evaluating different implementation variants, are strongly required in order to push RFID system development forward. Often, prototypes are pre-studies for the final product. They are demonstrators to show the feasibility of such a product as well as for marketing purposes for future products. Such prototypes often include the entire functionality of the final product [37] and thus, in particular for highly complex systems, their development may be as challenging and time consuming as the development of the final product. Especially the advantage of an exploration of the system on an *early* design stage is not supported.

Hence *rapid prototyping* seeks to accelerate the design process in several ways:

- In order to realise a highly configurable setup, most of the signal processing tasks are accomplished in the digital domain on reconfigurable components rather than on custom Printed Circuit Boards (PCBs) with analogue components (such as filters, modulators and demodulators, encoders, and more). Essentially the entire baseband processing on both transmitter and receiver side is realised by digital components, which strongly facilitates a rapid configuration and allows for an exploration of implementation variants. An analogue frontend is required for further tasks as up- and downconversion, power amplification, carrier suppression, signal conditioning or antenna matching.

- The concept of rapid prototyping aims to include only what is of specific interest, but not the entire functionality in the prototype. These could for example be certain signal processing algorithms that are newly introduced, as for example a synchronisation and decoding concept. A certain evaluation and measurement concept is developed and thereafter the required functionality for that specific measurement is designed.

- Similarly, the focus is not pointed towards a very resource efficient implementation, but rather to a demonstration of the feasibility of the implementation and the functionality. Certain structures can also be optimised in terms of hardware resource consumption, if this is of specific interest, however this is not the primary goal for the overall design. Furthermore, form factors, assembly issues and more are usually only of secondary interest [37].

- Therefore, easily configurable and rather oversised hardware platforms are utilised instead of custom PCBs equipped with optimised ASICs and analogue components. Due to the use of powerful platforms, the designers do not need to bother about certain implementation details or especially resource efficient implementations, but can concentrate on the implementation of the innovative algorithms [38]. Typical

platforms are composed of a set of digital signal processors (DSPs), field programmable gate arrays (FPGAs), microcontrollers and analogue to digital (ADC) and digital to analogue (DAC) converters. These platforms are not designed for a specific application, but suitable for a wide range of different implementations. Such prototyping boards are provided by several companies, including Lyrtech [39], Pentek [40] or Nallatech [41].

- Finally, the electronic design automation (EDA) industry offers several tools to automate and speed up the design process (such as MATLAB / Simulink [42], Synopsys [43], Mentor Graphics [44], Xilinx ISE and System Generator for DSP [45], Altera Quartus and DSPBuilder [46], Coware [47] or LabVIEW [48], just to name a view). Following a rapid prototyping approach, algorithms are designed on high level of abstraction (for example in MATLAB / Simulink or SystemC) and are subsequently modified to more detailed descriptions. The process of stepping from one level to the next more detailed level of description is highly automated [49]. This on the one hand speeds up the design process, while on the other hand it ensures consistency between the various description layers.

With these design acceleration concepts rapid prototyping meets the demands for an early exploration and evaluation of wireless systems.

1.4 Survey of Test and Verification Environments

While this thesis concentrates on the rapid prototyping concept, system exploration is also realised by system simulators and test environments based on off-the-shelf components and measurement devices. In the following, a short survey about established RFID simulation environments, RFID test environments using off-the-shelf components and finally rapid prototyping platforms is given.

1.4.1 System Simulators

Several powerful simulation environments for RFID have been reported recently, focusing on different goals. Simulation basically is part of every development and verification process, in this survey I concentrate on system simulators. Typical questions of research here include the evaluation of single components of RFID equipment, as for example RFID tags [50–52], readers [53], or antennas and analogue parts [54], physical and logical layer simulation and its impact to the performance of the RFID system in different frequency domains [51, 55–59]. Simulators further call attention to multi-tag and multi-reader environments [60–67]. Additionally, simulators concentrating on specific applications have been shown, for instance in [68]. The potential of generating misleading facts because of inaccurate modeling of underlying physical conditions, such as the wireless channel is discovered in [69]. Hence, in order to cross-verify the simulation assumptions an approach of validating simulation results by commercially available RFID equipment or rapid prototyping environments is pursued, as presented in the following.

1.4.2 Test Environments by Off-The-Shelf Components

Researchers cross-check simulation results with measurement data, generated by off-the-shelf RFID components [55, 70], or a controlled environment composed of prototypes, commercially available RFID components, and measurement equipment [71]. Moreover, several groups reported measurement results by off-the-shelf RFID equipment: Pentilla et al. [31] study the impact of fast moving objects in RFID systems, Ramakrishnan et al. [72] provide benchmarks on multi-tag and long range system performance while the LANDMARC demonstrator shows results on tag localisation with multiple readers and multiple tags [73], and recently a person tracking system based on RFID and wireless sensor networks was shown [74]. This approach however has the disadvantage that the designers do not have full access to all the parameters of interest in their measurement equipment, for example for adapting modulation parameters or accessing anti-collision schemes. Researchers cannot deploy novel signal processing concepts on the physical layer, and, especially for physical layer experiments, need to accept the provided performance of the available equipment. Only experiments with already existing equipment can be carried out, while novel concepts cannot be directly evaluated by experiments.

1.4.3 Rapid Prototyping Environments for RFID

As an alternative, researchers also follow the concept of rapid prototyping, mapping the simulation code consistently to embedded devices and examine the functionality of the *same* code (gold code) in simulations as well as in a measurement environment. This approach, transferring simulation code to embedded microcontrollers, DSPs or FPGAs is followed in [50, 52, 75–77] for RFID tags, or in [56, 78] for RFID readers. Furthermore, the approach of an automatic generation of hardware modules out of high level descriptions is demonstrated on the example of decoding and encoding units in [78] and [79], respectively. Untangling standard compatibility issues and automating the design-flow for a multi-standard active RFID tag is addressed in [80]. The setup of a generic measurement and test platform based on LabVIEW is shown in [81]. Compared with the previously described approach employing commercially available RFID components, this approach has the advantage, that new algorithms and concepts can be rapidly evaluated for their functionality and feasibility in implementation.

Examples of automated design flows for RFID tag designs have been shown by the RFID center of excellence at the University of Pittsburgh (http://www.engr.pitt.edu/SITE/rfid) and by the Graz University of Technology (http://www.iti.tugraz.at/). The first group shows a design flow for active RFID tags based on a microprocessor or custom hardware processor, out of a high level ANSI C code description [76]. The group from Graz University of Technology reports on a cosimulation framework of system level (Matlab and Simulink) and hardware description level (VHDL / AMS) for novel RFID tag architectures [52].

1.5 Characteristics of RFID Systems

Compared to other communication environments, differing characteristics of RFID systems are identified, which demand specific signal processing algorithms, and thus influence the rapid prototyping of RFID systems:

1. Passive tags and backscatter technology demand reader architectures for handling the inherent carrier leakage from the transmitter to the receiver. This is true for the development of both, analogue frontends as well as digital receiver structures.

2. The use of passive tags results in limited processing capabilities on tags, and hence requires complex signal processing algorithms to be accomplished on RFID readers. The required interaction between the reader and the tag for computing a sophisticated transmission scheme, is not available with low complexity tags. For example, such advanced transmission schemes require a feedback information for channel estimation from the tag to the reader, to realise multiple antenna transmit schemes at the reader. This feedback information however cannot be processed on the tags, such that signal processing algorithms for RFID need to be designed to meet with the imbalance of processing capabilities between readers and tags.

3. The wireless channel shows a fundamentally different structure to the regular point-to-point wireless channel: due to the backscatter modulation of passive tags, the uplink communication channel coefficient consists of the reader-to-tag and tag-to-reader channel. Thus, the link quality is effected by the forward and the backward channel coefficient simultaneously (see Chapter 3 for details). The tag realises a pinhole in this dyadic channel from the transmitter to the receiver of the RFID reader [34, 82]. In contrast to other wireless systems, where a point-to-point connection from Device 1 to Device 2 may be considered, the sole consideration of the tag-to-reader channel is not useful in the context of RFID.

4. RFID systems are operated in scenarios with moving tags. Thus, the channel experiences a Doppler spread ν, which is upper bounded by the maximum doppler shift $\nu_{max} = 2f_c v_{max}/c_0$. Here, v_{max} is the maximum velocity of the tag moving in direction towards the reader, f_c denotes the carrier frequency and c_0 denotes the speed of light. Note, that in the dyadic channel of RFID systems the Doppler shift due to a moving tag affects the forward and the backward direction. The time the channel is assumed to be static is called the coherence time $T_c \approx 1/\nu_{RMS}$, where $\nu_{RMS} < \nu_{max}$ is the root mean square bandwidth of the doppler spread [83, 84]. Equating the coherence time T_c with the readout time of one uplink packet $T_{readout}$, allows to calculate the maximum tag velocity v_{max} for which the channel is not changing considerably :

$$v_{max} = \nu_{max}\frac{c_0}{2f_c} > \nu_{RMS}\frac{c_0}{2f_c} \approx \frac{c_0}{2f_c T_c}. \tag{1.1}$$

   Assuming FM0 encoding in the uplink channel and the lowest data rate of 40 kbit/s, the readout time $T_{readout}$ of the first uplink packet of a communication is 1.1 ms.

With the UHF carrier frequency of 868 MHz, this allows for a maximum tag velocity of v_{max}=156 m/s, which is much faster than the expected tag velocity. Hence, for realistic tag velocities the Doppler shift is not relevant and the channel can be assumed to be static during $T_{readout}$.

5. In a multipath propagation environment, such as the UHF RFID environment, signal components with various delays result in a delay spread. If we consider, that signal components from reflectors that are further away than two times the maximum readout distance d_{max} are not influencing the channel considerably, the maximum delay τ_{max} of any signal component contributing to the channel coefficient is: $\tau_{max} = d_{max}/c_0$. The bandwidth, within the correlation between fading at the included frequencies is assumed to change less than 3 dB is called the coherence bandwidth B_c. It is approximated by $B_c \approx 1/\tau_{RMS} > 1/\tau_{max}$, where $\tau_{RMS} < \tau_{max}$ is the root mean square delay spread. With a maximum readout distance of 10 m in UHF RFID systems, the coherence bandwidth is: $B_c > 30$ MHz. The required signal bandwidth for the maximum data rate of 640 kbit/s is approximately 2.56 MHz, and thus much smaller than B_c. Hence, the channel can be assumed to be frequency flat in UHF RFID systems, which is also confirmed by measurements in [85]. Thus, UHF RFID systems are considered as narrow-band systems, where a system is considered to be narrow-band, if the inverse of the system bandwidth is much greater than the maximum excess delay of the various multipath components [84].

1.6 Outline of the Thesis

This thesis is based on the following publications, which will be referred to in the overview of the chapters at the end of this section.

- C. Angerer, B. Knerr, M. Holzer, A. Adalan, M. Rupp, "Flexible Simulation and Prototyping for RFID Designs," in Proc. First International EURASIP Workshop on RFID Technology, RFID 2007, p. 51-54, Vienna, Sept. 2007.

- C. Angerer, M. Holzer, B. Knerr, M. Rupp, "A Flexible Dual Frequency Testbed for RFID", in Proc. 4th International Conference on Testbeds and Research Infrastructures for the Development of Networks and Communities, Innsbruck, Austria, March 2008.

- C. Angerer, "A Digital Receiver Architecture for RFID Readers," in Proc. 3rd International Symposium on Industrial Embedded Systems (SIES), pages 97-102, Montpellier, France, 2008.

- C. Angerer, M. Rupp, "Advanced Synchronisation and Decoding in RFID Reader Receivers," in Proc. IEEE Radio and Wireless Symposium 2009, San Diego, USA, January 2009 (invited).

- C. Angerer, R. Langwieser, "Flexible Evaluation of RFID System Parameters using Rapid Prototyping," in Proc. 2009 IEEE International Conference on RFID, Orlando, USA, April 2009.
- C. Angerer, R. Langwieser, G. Maier, M. Rupp, "Maximal Ratio Combining Receivers for Dual Antenna RFID Readers," in Proc. 2009 IEEE MTT-S International Microwave Workshop Series on Wireless Sensing, Local Positioning and RFID, p. 21-24, Cavtat, Croatia, Sept. 2009.
- C. Angerer, G. Maier, M. V. Bueno-Delgado, M. Rupp, J. Alonso-Vales, "Single Antenna Physical Layer Collision Recovery Receivers for RFID Readers," in Proc. 2010 IEEE International Conference on Industrial Technology, Viña del Mar, Chile, March 2010.
- C. Angerer, R. Langwieser, M. Rupp "RFID Reader Receivers for Physical Layer Collision Recovery", accepted for publication in the IEEE Transactions on Communications.
- C. Angerer, R. Langwieser, M. Rupp "Direction of Arrival Estimation by Phased Arrays in RFID", in Proc. of the Third International EURASIP Workshop on RFID Technology, Spain, Sept. 2010.
- C. Angerer, R. Langwieser, M. Rupp "Experimental Performance Evaluation of Dual Antenna Diversity Receivers for RFID Readers", in Proc. of the Third International EURASIP Workshop on RFID Technology, Spain, Sept. 2010.
- C. Angerer, R. Langwieser, M. Rupp, "Evaluation and Exploration of RFID Systems by Rapid Prototyping", submitted to Personal and Ubiquitous Computing.

The content of the individual chapters is briefly described in the following:

Chapter 1 introduces RFID systems, showing the features of state-of-the-art RFID equipment and different applications in use. Various problems and demands on the way for RFID technology to become ubiquitous in every day life are pointed out: compatibility issues of RFID equipment, the exploration of RFID system parameters, the evaluation of signal processing algorithms in experiments and the need for an automated design process. The pros and cons of simulation environments, measurement platforms using off-the-shelf RFID equipment and rapid prototyping solutions are introduced.

Chapter 2 presents the rapid prototyping design methodology for the setup of an experimental research platform [56, 78]. While several groups focus on automated design flows for RFID tags [50, 52, 75, 76], this chapter describes the setup and design flow of an RFID test environment, which allows to test RFID systems in various different real-time setups and configurations, as well as to rate different reader receiver architectures by simulation and measurement. During the time of writing this thesis, other authors developed similar experimental setups based on Labview [81, 86]. Moreover, several RFID simulation environments and setups using off the shelf components have

been reported [51, 55, 57–59, 70, 71]. Compared to that work, the design flow suggested in Chapter 2 does not focus solely on simulation or experimental setup, but combines both by consistently mapping simulation models to the rapid prototyping platform. The target hardware platform is described in detail. Finally an exemplary measurement for the exploration of RFID system parameters using this setup is shown [87].

Chapter 3 focuses on the implementation of optimum RFID reader receiver architectures: in a first step, a model for receive signal constellations at RFID reader receivers is given. Based on that model, a digital receiver architecture is presented, consisting of a preprocessing step for conversion to baseband, a channel estimation and equalisation, and finally a synchronisation and decoding part [78, 88, 89]. The performance of the optimal maximum likelihood receiver with FM0 encoding is identified and losses due to channel estimation, and especially synchronisation are illuminated. Related work on theoretical performance comparison of RFID reader receivers includes [57, 90], who propose Viterbi and differential decoders, and also address the topic of synchronisation [57]. Additionally, limited work on practical realisations of FPGA based RFID readers is given by Huang et al. [91, 92]. As RFID systems feature deviations of symbol rates that are much stronger than in other wireless communications systems, synchronisation is a complicated issue. The major contribution in this chapter is the application and modification of state-of-the-art synchronisation techniques [93] to RFID in order to meet with this challenge. Additionally I develop a channel estimation algorithm which allows for the separation of the carrier leakage and tag signal, and to subsequently equalise the channel. The receiver is implemented on the introduced target platform, and details about its implementation are given.

Chapter 4 treats the extension of the single antenna to a dual antenna receiver. Equipping the RFID reader with multiple receive antennas, allows to combat multipath propagation and fading using receive diversity techniques, especially maximal ratio combining. Thus, the topic of increased reliability of RFID systems is addressed in this chapter. While this thesis focuses on diversity combining on the RFID reader receiver [94, 95], Griffin et al. [33, 34] and Nikitin et al. [96] investigate the performance increase due to multiple antenna RFID tags. Ingram et al. [97] moreover propose a model for both, multiple antenna tags and readers. The multiple antenna receiver that I propose is additionally suitable for direction of arrival estimation of the tag signal in low fading environments [98]. This addresses the topic of tag localisation, which has only been addressed very recently (spring 2010) by multiple antennas [99, 100], but previously by installing multiple RFID readers and localising tags using range estimates [73, 101]. Again, a digital architecture of the dual antenna receiver is implemented on the rapid prototyping platform and performance figures from measurements are presented.

Chapter 5 finally discusses a further extension of the single and multiple receive antenna system to a separation of several colliding RFID tags in the uplink channel (on the reader receiver side). The potential of signal separation on the physical layer during a

multiple tag collision has also been identified by Shen et al. [102] and Khasgiwale et al. [86], however they do not propose any receivers for recovering from the collisions. I extend the previously developed signal model to slots of the framed slotted aloha protocol, where multiple tags generate a collision. Two types of receivers for recovering from such collision slots are proposed: the first class are single antenna receivers [103], which separate the signals from the colliding tags by exploiting the properties of the tag modulation and the resulting signal constellation in the I/Q plane. The second class of receivers propose to utilise multiple receive antennas for discriminating the tags due to their spatial signature [104]. A channel estimation algorithm for such systems is proposed. Additionally, both classes of receivers are verified with measurement data and a performance analysis is given. If the reader is able to recover from collisions of two tags, a theoretical throughput increase of 1.6 times the throughput of a conventional reader is achieved. Thus, the topic of throughput in high volume tag applications is addressed in this chapter.

2 RAPID PROTOTYPING CONCEPT

This chapter introduces the hardware setup with its digital baseband and exchangeable analogue frontends. Moreover, the established design flow following the rapid prototyping approach is presented. An exemplary measurement for exploring RFID system parameters and achievable tradeoffs completes this chapter.

2.1 Hardware Description

This first section is devoted to the description of the underlying hardware components of the established rapid prototyping platform. Due to the limited processing capabilities with the limited available energy of state-of-the-art tags, RFID systems feature a highly imbalanced share of signal processing capability. Therefore, complex algorithms, such as MIMO signal processing, beamforming or anti-collision schemes cannot be realised on passive RFID tags at a current state. Hence, I focus on a compensation of this imbalance by rapid prototyping of advanced signal processing schemes on RFID readers. The focus of this thesis is to increase performance by developing and deploying digital signal processing algorithms on RFID readers, which are novel to the field of RFID.

As a hardware platform for the digital part rapid prototyping system I use a development board from Austrian Research Centers [105]. Figure 2.1 depicts the basic structure of this prototyping board. Its main reconfigurable components are a fixed-point DSP from Texas Instruments (TMS320C6416) and a Xilinx Virtex II FPGA. Additionally, it exhibits two digital to analogue converters (16 bits) and two analogue to digital converters (14 bits). The DSP is clocked with 600 MHz while the FPGA, DACs, and ADCs are sourced by a single clock of 40 MHz. An Ethernet interface connects the DSP to a PC, thus allowing for an external communication to an application running on a PC.

The exchangeable analogue frontends have been developed in house, and support the frequency bands at 13.56 MHz (HF) and 866-868 MHz [106–108] (UHF). The frontends exhibit a carrier suppression module and the option to use an analogue envelope demodulator. The interface between the digital part and the analogue frontends is realised at an intermediate frequency of 13.56 MHz for the HF band and at 13.33 MHz for the UHF band (compare with Section 3.6.1). The carriers are directly synthesised in the digital domain and the modulated transmit sequence is output to the DAC. The ADC input signal is a bandpass signal centered at the same frequency as the transmit signal. In case of

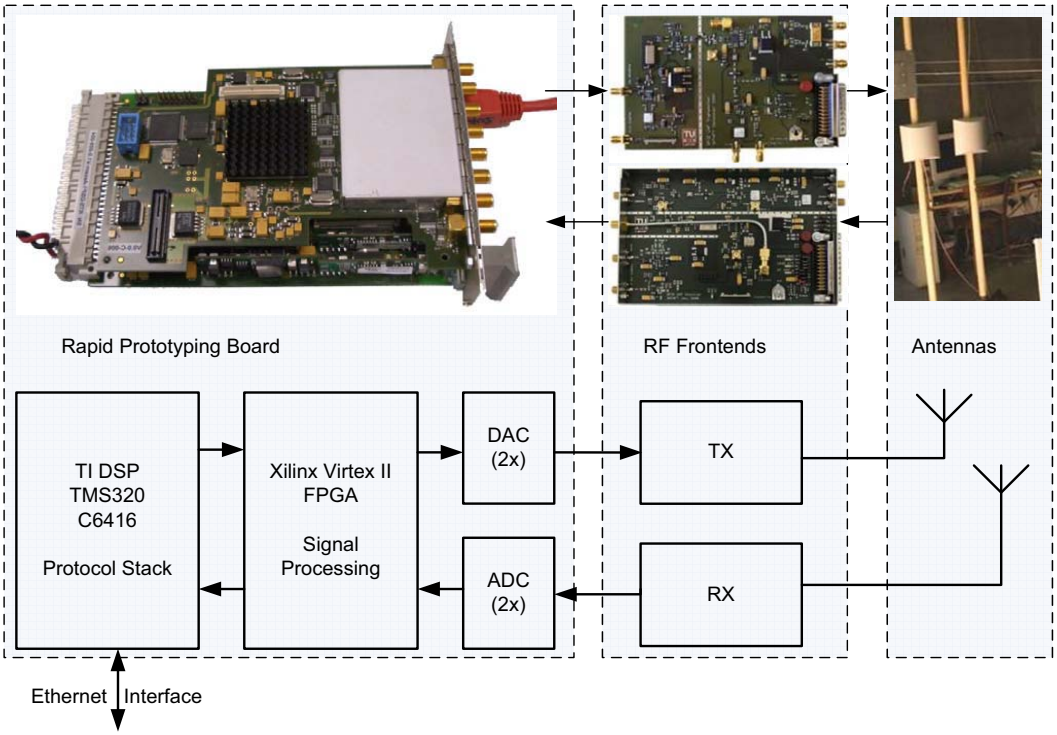

Figure 2.1: Photograph and block diagram of the target hardware. The UHF frontends on the picture are custom developments and described in [106–108]

.

a UHF RFID implementation the output signal at the intermediate frequency is additionally upconverted to 868 MHz applying a heterodyne conversion, and the 868 MHz receive signal is downconverted by the same principle. A further extension of the frontend to 2.4 GHz is foreseen.

2.1.1 Requirements for the Digital Baseband

As stated previously, the digital baseband section should be designed to be highly modular, easily parameterisable and consistent with simulation layers. A modular design ensures the easy exchange of certain blocks, such as modulators, demodulators or filters, and thereby rating various architectures and algorithms. In order to explore the influence of certain system parameters, it is necessary to provide access from an application to change these parameters. In DSPs these parameters are reflected by variables, while in FPGAs this is achieved providing register banks to a controlling software application, that accesses the parameters via those registers during run-time. A list of accessible parameters and FPGA registers is found in Appendix E.

The established rapid prototyping environment accomplishes the following tasks in the digital baseband:

- Protocol processing: Naturally protocol processing needs to be carried out on digital components, such as microcontrollers or DSPs. It includes the generation of transmit signals on a logical (bit-) level and the correct processing of the protocol state machine. In order to support a wide range of RFID applications, the support of multiple protocols is desired.

- Transmit signal generation: In order to realise a flexible setup, the transmit signal is generated in the digital domain. All parameters of interest affecting the shape of the transmit signal are accessible by a controlling software, as for example data rate, encoding, modulation and filter parameters.

- Modulation: In the transmitter amplitude shift keying (ASK) or phase shift keying (PSK) need to be supported. The modulation index is desired to be controlled for the establishment of a flexible test platform.

- Encoding and decoding: Several encoding types are standardised, including pulse interval encoding (PIE) and one-out-of-four encoding in reader-to-tag communication, and FM0, various Miller and Manchester subcarrier encodings in tag-to-reader communications. In order to explore the influence of the defined coding parameters, full control over these encoding parameters is guaranteed. A major interest is in rating various decoding algorithms on subcarrier or FM0 encodings [57, 89–91].

- Up- and downconversion: As the digital to analogue interface is realised at an intermediate frequency of 13.56 MHz and 13.33 MHz, for the HF and UHF band respectively, up- and downconverters are required. An interface at an intermediate frequency has the advantage of realising I/Q demodulation in the digital domain, thus just requiring one ADC for sampling the receive signal, and decreasing the distortion of I/Q imbalance at the tradeoff of a higher required sampling rate.

- Filtering: Digital filters with given parameters are realised rapidly with the assistance of high level filter design tools, as for instance the filter and design analysis toolbox of MATLAB.

- Signal detection: A major challenge in RFID reader receivers is the detection of the receive signals, due to the following facts: first, in passive RFID, the reader needs to supply the tags with power, resulting in a strong leakage of this energy supplying carrier into the receiver. This undesired leaking carrier can be up to a factor of 90 dB stronger than the desired receive signal [11, 109]. Second, the receive signal has a high dynamic range, depending on the reader to tag distance, the state of the channel and finally on the backscatter efficiency of the tag. Eventually, noise can severely degrade the detection performance, which is especially an issue

in industrial environments. Due to these factors, a channel and carrier leakage estimation algorithm for proper signal detection is required [57, 88].

- Synchronisation: Finally, synchronisation is a major issue in wireless communications in general, and in particular in RFID, due to the wide tolerances in backscatter symbol length [17]. Several structures have been proposed and rated, utilising the properties of the encoding formats and correlator structures [57, 89, 92].

Details about these various tasks and their implementation are provided in Chapter 3. Additional related work describing digital RFID reader solutions include FPGA based RFID readers [110, 111] and system-on-chip RFID readers [111–114].

2.2 Design Concept

The design flow developed for configuring the target hardware is highly automated, in order to permit a fast (re-) configuration of the system. Three layers in the design flow are defined, which model the system on different abstraction levels with an increasing level of detail, from abstract system simulations down to the implemented prototype [56]. The design flow supports a consistent evaluation process on these layers. The automation of the process of stepping from one layer to the next lower layer supports a rapid configuration of the prototype, and ensures consistency in between the layers. The proposed design flow is depicted in Figure 2.2. The three layers are named the link layer model, the physical layer model and finally the rapid prototype. The link layer and physical layer model serve as simulation layers for the protocol processing and the signal processing, respectively. The reader and tag part of the link layer model are coded in `C++` and `SystemC`, respectively, and several RFID standards are supported, namely EPCglobal Generation 1, Class 2 [17], the EPCglobal draft for the HF domain [115] and ISO15693 [116]. The physical layer is modeled in Matlab/Simulink and serves as a refinement of the link layer model. It evaluates specifics of the physical layer transmission, such as modulation and encoding settings, effects of channels or specific details of the receiver architectures. Finally, on the rapid prototype, real-time measurements are conducted to verify both, protocol and signal processing. The results of the two simulation layers, for example influence of different RFID system parameters like protocol parameters, distinct receiver architectures, different environmental conditions, or hardware configurations (like single or separated receive and transmit antennas) and more, are crosschecked and assumptions for simulations are validated.

The various layers in the design flow do not only work as stand-alone simulations, but are strongly interconnected to each other. On the one hand, generated sequences and a set of configuration parameters from the link layer model can serve as an input to the transmitter in the physical layer model, to generate the appropriate transmit signal. On the other hand, samples of tag sequences that are captured on the prototype during

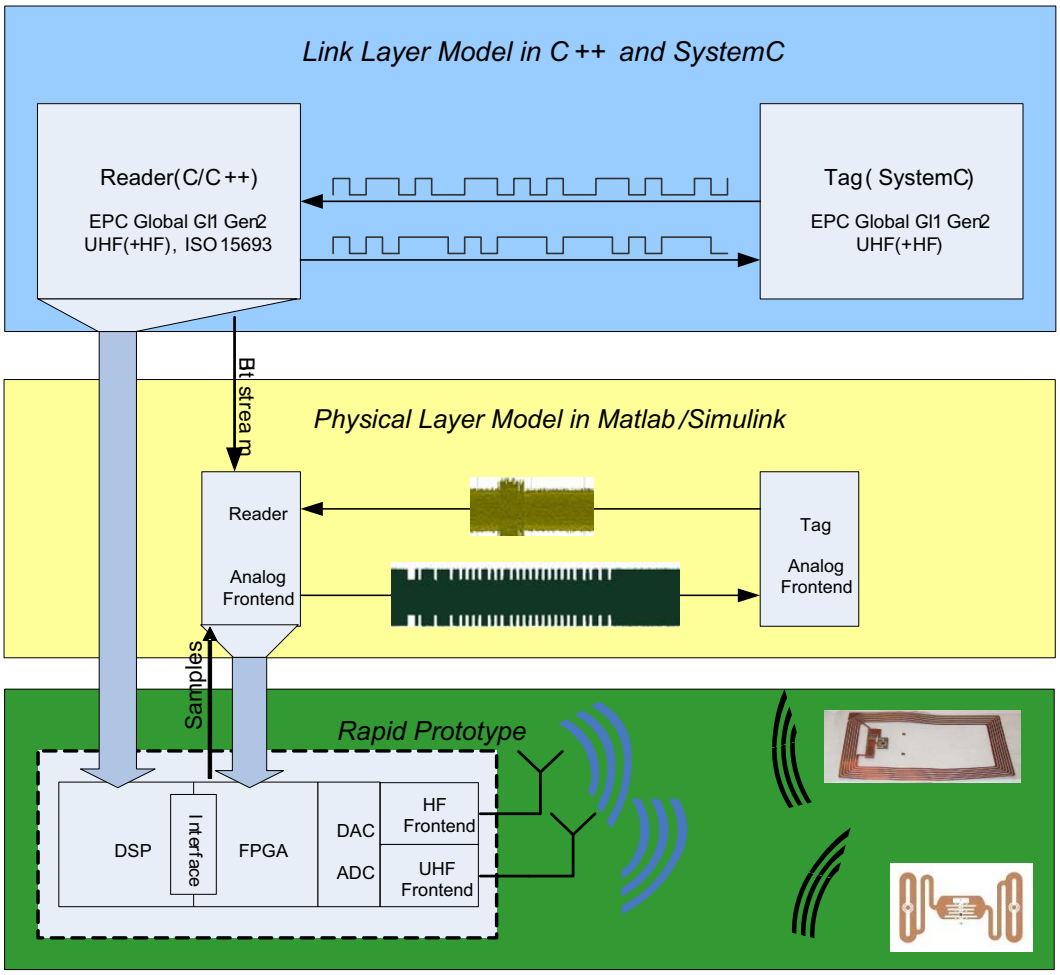

Figure 2.2: Design flow for the RFID prototyping system.

real-time measurements serve as a simulation input for the receiver on the physical layer model.

The automation of the design flow is achieved by the following process: The code of the RFID reader on the link layer model is directly embedded on the DSP on the rapid prototyping board. As the reader part of the model is coded in C++, only the interfaces of the simulation model and the DSP software have to be adjusted. This is readily achieved using globally defined variables. For the physical layer, at least some parts of the code are automatically converted to VHDL and embedded on the FPGA of the board, using Simulink to VHDL conversion tools. This conversion is either provided by the HDLCoder toolbox of MATLAB or the System Generator of Xilinx [45]. These tools are well suited for data-flow oriented code, such as digital filters, modulators or up- and downconverters. Modeling of control-flow oriented code, for example Finite State Machines (FSM) is supported by the state-flow package of Simulink, however the

description of complex code has shown to be very tedious. Hence, these parts of the design are modeled using a traditional, hand-written VHDL description. The code of the RFID reader is finally embedded into a VHDL framework, providing the interfaces to the surrounding components on the FPGA (like DSP, ADCs and DACs). These interfaces are independent of the currently implemented reader architecture and do not need to be adapted for different designs. Furthermore, with a testbench for the emulation of these interfaces, a functional verification of the entire VHDL description in Mentor Graphics' Modelsim is enabled. The testbench provides the transmit bits and control parameter settings in form of register accesses as an input for the transmitter, and captured receive samples from the hardware setup as an input of the receiver of the RFID reader.

With this approach various signal processing architectures have been rated to each other, for example receivers with envelope demodulators and I/Q demodulators, different signal detection schemes, or different synchronisation units [78, 89]. Measurement results for rating the performance tradeoffs in RFID systems are shown in the following Section 2.3.

2.3 Exploration of System Parameters based on Measurements

Today's RFID applications demand performance goals such as a high level of readout reliability or a high data throughput in the desired readout range, detection of all tags in a multi-tag scenario or full functionality in adverse environments. As illustrated above, thorough understanding of influencing parameters affecting these goals, as well as the available tradeoffs is essential in order to further improve RFID technology. An exemplary question of interest is the influence of transmit power ($\mathrm{P_{TX}}$) and backscatter link frequency (BLF, proportional to data rate) on readout reliability, reflected by the received energy per bit to noise power spectral density ratio E_b/N_0 of the RFID reader on the one hand and by the errors in the communication on the other hand. The receive E_b/N_0 is expected to follow the form:

$$E_b/N_0 = c\frac{\mathrm{P_{TX}}}{\mathrm{BLF}}\frac{1}{N_0}. \tag{2.1}$$

It is proportional to $\mathrm{P_{TX}}$ and inverse proportional to BLF, as with an increasing symbol period (proportional to 1/BLF) the accumulation time of energy for one bit increases, assuming a constant receive power. The proportionality constant c includes all losses of the system, such as the channel attenuation. The selection of the parameters BLF and $\mathrm{P_{TX}}$ just serves as an example, in principle the influence of all parameters of interest can be evaluated.

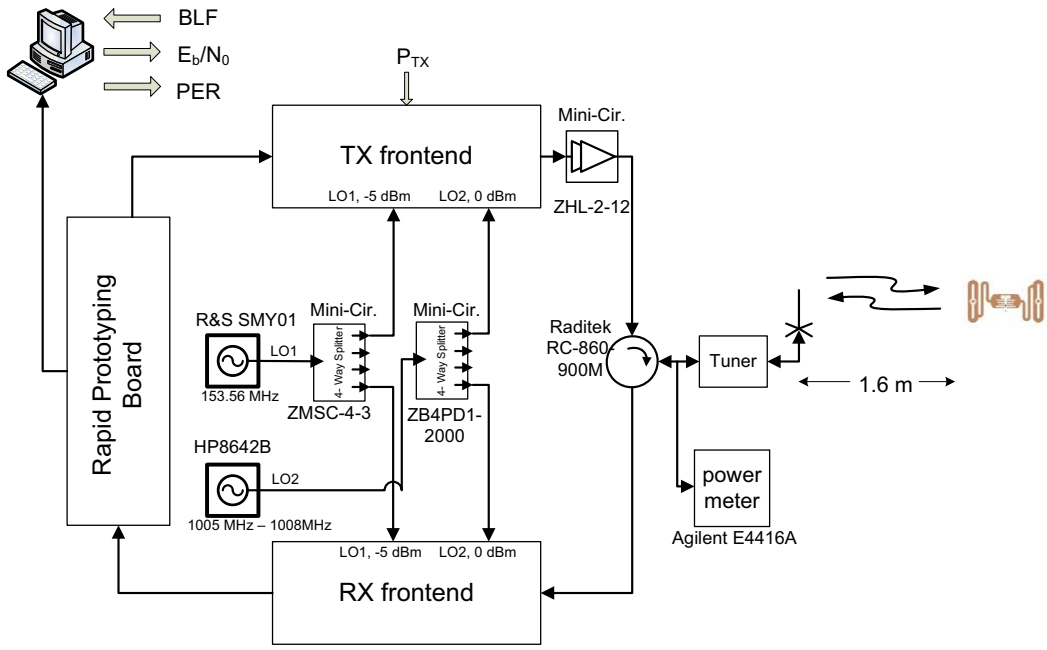

Figure 2.3: Measurement setup for evaluating influence of certain parameters on the overall performance. The applied transmit power $\mathrm{P_{TX}}$ and backscatter link frequency serve as tuned input parameters, while the energy per bit to noise power spectral density ratio E_b/N_0 and Packet Error Ratio (PER) serve as observation values.

2.3.1 Setup

In order to achieve reproducible measurements and to avoid influence from changing environments and hence to measure only the influence of the intended parameters, the measurements have been conducted in a measurement room with a static measurement setup. Figure 2.3 shows the measurement setup, which includes the digital rapid prototyping environment, the analogue frontend, an external Power Amplifier (PA) and finally the antenna. In order to minimise reflections of the transmit signal back into the transmitter of the frontend, an impedance tuner improves the impedance matching of the antenna. A circulator decouples transmitter and receiver, while the output power is monitored by means of a power meter. To measure the correct unmodulated carrier power of the transmitter, the power meter was gated to the so called lead-in-phase of the test signal which is depicted in Figure 2.4. During this time period, only the unmodulated carrier at 866 MHz was transmitted. The tag was placed at a distance of 1.6 m from the antenna of the reader. Throughout the measurement the same single tag was employed [117]. Hence, the results are typical but it is expected that a set of tags leads to slight variations in measurements. Thus, the results shown here are exemplarily. The output of the UHF receiver was connected directly to the ADC input of the rapid

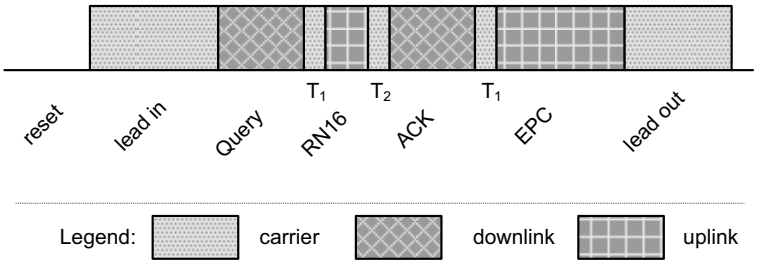

Figure 2.4: Interrogation sequence in measurements.

prototyping board. Additionally, the output was monitored by an oscilloscope. While the antennas of the reader and the tag were placed inside of the measurement room, the rapid prototyping environment with its frontends and measurement equipment was placed outside of the room.

For this campaign the varied system input parameters were the Backscatter Link Frequency (BLF) and the transmit power ($\mathrm{P_{TX}}$). The monitored output parameters were the estimated E_b/N_0 and the Packet Error Ratio (PER), which are both computed on the digital receiver of the rapid prototyping board. During the measurement the BLF was varied from 160 kHz to 640 kHz, for different adjusted transmit power values. The reader reads out the electronic product code (EPC code) of the tag periodically, applying the same parameter settings, in order to compute an average of E_b/N_0 and PER. For the next set of input parameters, the procedure is repeated. Each parameter set has been applied for 10^4 EPC code readouts, where each of these readouts consisted of the following intervals: reset, lead-in, Query, T_1, RN16, T_2, Acknowledge, T_1, EPC code, lead-out (Figure 2.4). During the reset phase, the tag was not supplied with energy, while the lead-in-phase powers the tag before reading its EPC code. After the EPC code readout the tag was still supplied with energy during the lead-out-phase, before the next interrogation started with a reset phase. During the time interval T_1 the noise power is estimated which is further required to estimate the E_b/N_0. This estimation is described in detail in the following Chapter 3.

Additionally, the settings shown in Table 2.1 have been applied (according to the EPC-global standard [17], also compare with Appendix C). The divide ratio (DR) and tag-to-reader calibration symbol (TRCal) control the backscatter link frequency of the tag, and hence are varied. The reader-to-tag calibration symbol (RTCal) calibrates the tag to distinguish between '0' and '1' bits in reader to tag communication. As also the link timing T_1 is dependent on this RTCal value, and the period T_1 is used to estimate the noise in the digital receiver, I set RTCal to maximise T_1. Finally, the reader-to-tag communications encoding parameters tari (type A reference interval) and pulse width (PW) are set to RTCal/3 and tari/2, respectively. Throughout this measurement, FM0 encoding for the tag-to-reader communication has been selected. This maximises the data rate among all possible uplink encoding schemes, with the data rate being equal

parameter	range according to EPCglobal UHF standard	value
reset	-	10ms
lead-in	-	3ms
lead-out	-	2ms
encoding	-	FM0
DR	8, 64/3	8, 64/3
BLF	40 - 640 kHz	variable
TRCal	17.2 - 225 μs	variable
RTCal	TRCal/1.1 - TRCal/3	maximum
tari	6.25 - 25μs	RTCal/3
PW	max(0.265 tari,2) - 0.525 tari	0.5 tari

Table 2.1: Parameter settings for measurement.

to the backscatter link frequency.

2.3.2 Results

For the evaluation of the readout quality the E_b/N_0 and PER have been considered. The E_b/N_0 has been calculated by dividing the average of both, the estimated receive signal power ($\hat{E}_b$) and the estimated noise power ($\hat{N}_0$) during the 10^4 readout attempts ($E_b/N_0 = \hat{E}_b/\hat{N}_0$). The PER is calculated by dividing the successful EPC code readouts by the 10^4 readout trials. A correct readout implies the correct reception of both, the 16 bit random number as a response to the query command as well as the 128 bit EPC code. It is important to mention that the sequence as shown in Figure 2.4 has been applied to readout the EPC code, not demanding any retransmissions by means of the Not Acknowledged (NAK) command if the CRC check of the EPC code did not succeed. Hence, only the successful readouts at the first attempt are considered, such that the PER is the PER performance of the physical layer only.

Figure 2.5 and Figure 2.6 show the E_b/N_0 and PER depending on the backscatter link frequency. It can clearly be observed that for increasing BLF the E_b/N_0 decreases: On the one hand, the receive energy per bit $E_b = P_S T = P_S/\mathrm{BLF}$ decreases with increasing BLF, if we assume a constant receive signal power P_S (compare with Equation (2.1)). Equivalently, a higher BLF can be viewed as a wider bandwidth in the matched filter, passing a higher amount of noise power, while a very large T leads to a tight spectrum, and hence permits tight filtering (compare with the following Chapter 3). On the other hand the tag requires more power for processing its data at a higher clock frequency. Finally, a third reason for this behaviour is the wider tolerance for the backscatter link frequency accuracy at increasing BLF values, as defined by the EPCglobal standard, complicating the accumulation of energy during T and the synchronisation in the digital receiver.

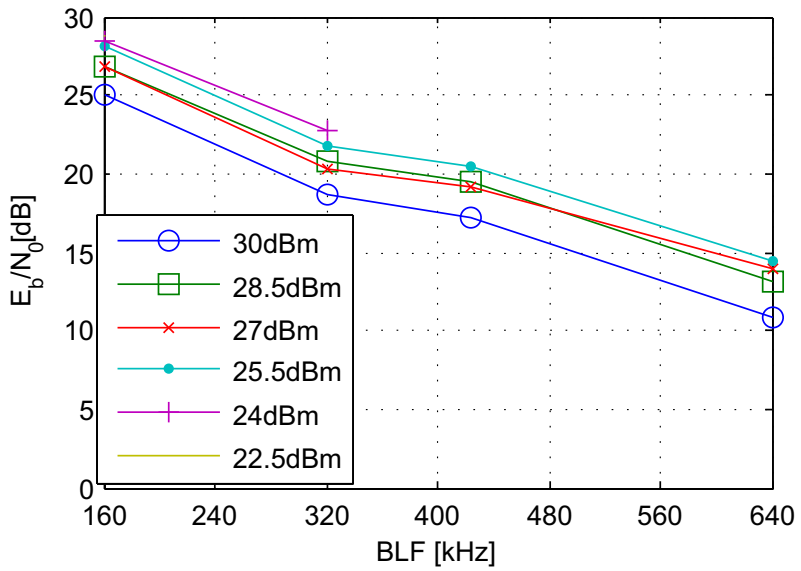

Figure 2.5: Estimated E_b/N_0 as a function of BLF.

Similarly, the PER increases with increasing BLF (Figure 2.6). Additionally, there is a slight increase at small backscatter link frequencies. This has been investigated to be caused from the long total response time at small BLFs: As the digital receiver assumes block fading, it estimates the channel just at the very beginning of the packet, but it does not track any additional changes during the reception [88]. The channel estimate also includes the backscatter behaviour of the tag. It is however observed, that during long tag response times, the backscatter behaviour of the tag slightly changes over time due to the changing internal power budget. Thus the assumption of block fading is violated, leading to an incorrect channel estimate in the receiver and therefore an increased packet error probability. Such a measurement result uncovers assumptions that are easily overlooked in simulations. The PER saturates at a value below 0.001, which is reasonable considering the reception of 128 + 16 bits at the RFID reader for the reception of one correct packet, and the expected functionality of the tag.

For setting a certain BLF value, there are overlapping configurations for a different setting of the divide ratio (DR) bit. The BLF point at 160 kHz has been evaluated using both configurations, however not showing any performance difference for the distinct settings.

The different curves in Figures 2.5 and 2.6 belong to distinct transmit power levels. It is adverted, that at higher BLF and lower output power, the tag has not sufficient energy left to respond. These points are not plotted in the graphs. This behaviour could also be observed on the oscilloscope, showing that at higher BLF and low transmit power, the tag is not capable to transmit its total EPC code, but stops after some fractions of it.

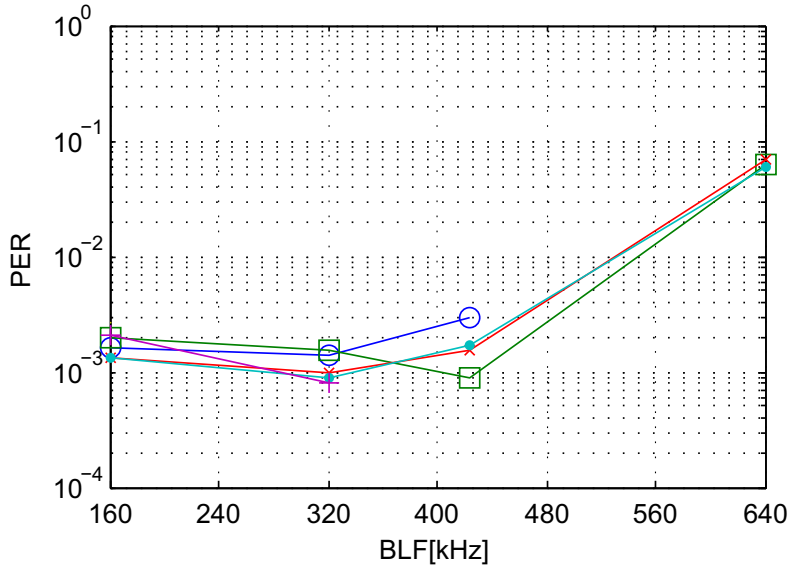

Figure 2.6: Packet errors as a function on BLF.

Figure 2.7 and Figure 2.8 show the results of the measurement, but plotted in a different fashion: PER and E_b/N_0 depending on the transmit power, with BLF as a parameter. In both figures it is observed, that the tag starts to communicate at a certain transmit power level. The E_b/N_0 is slightly decreasing with rising transmit power. The reason for this unintuitive effect is, that the energy storing capacitors at the tags are full at a certain output power, and thereafter the excessive energy is drained off in the shunt transistor, also during energy absorbing phases. This slightly decreases the normalised differential radar cross section $\sqrt{|\Delta\sigma|}$ of the tag [118], which describes the efficiency of the backscatter modulation as the difference between the tag's reflection coefficients in the *"reflect"* (ρ_r) and *"absorb"* (ρ_a) state: $|\Delta\sigma| = |\rho_r - \rho_a|^2$. This effect has also been observed by Mayer [119, 120], and is also depicted in Figure 3-6 of the tag datasheet [121]. A second reason for this slight E_b/N_0 decrease is the external power amplifier, that saturates at higher transmit power.

Similarly, the PER (Figure 2.8) shows a week increase at the higher transmit power. Again it is observed, that at low transmit power values, the communication at higher data rates ceases first.

The measurement results show that the expected model of $E_b/N_0(\mathrm{BLF}, \mathrm{P_{TX}})$ as described in Equation (2.1) does not fit well with the actual behaviour. Thus, a more realistic model is proposed:

$$E_b/N_0 = c\frac{\mathrm{P_{TX}}^{-\alpha}}{\mathrm{BLF}^{\beta}}. \tag{2.2}$$

By fitting the measurement data of Figures 2.5 and 2.7 the two coefficients α and β are determined as $\alpha = 0.51$ and $\beta = 2.12$. The two-dimensional fitting utilises the Least

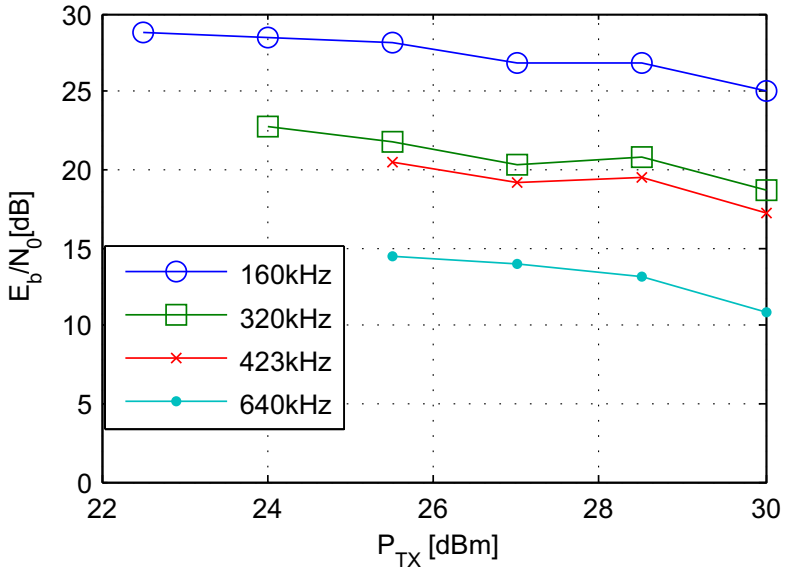

Figure 2.7: Estimated E_b/N_0 as a function of $\mathrm{P_{TX}}$.

Squares method of the Matlab curve-fitting toolbox, resulting in a Root Mean Square Error (RMSE) of 0.86 dB.

2.4 Discussion and Conclusion

The lack of experience with novel technologies such as RFID, and the concomitant absence of accurate simulation models are identified as crucial factors, hampering the progression of RFID to become ubiquitous in everyday life. By means of an exemplary measurement, the flaw of simplistic modeling is demonstrated. We observe, that RFID is fundamentally different to other wireless technologies, regarding the imbalanced share of the processing complexity between readers and tags as well as the dyadic pinhole channel with backscatter modulation and the severe carrier leakage. In order to understand such a system, which was only explored to a limited extent at the time of starting with this thesis (2007), a flexible test environment is highly desired. Its setup and underlying hardware is described, and the designflow for configuring the rapid prototyping system is presented. In order to increase consistency between simulation and measurement results and to deal with the complexity of novel signal processing algorithms, the design flow is automated to support a translation from high level simulation models to a synthesisable hardware description. The drawback of this approach is the relatively long time required to establish such a system (compared to simulators or off-the-shelf experimental environments), meaning the time to design interfaces and to prepare the hardware for experiments. For instance, several months of the work for this thesis were required to preserve a clean carrier signal from the digital hardware, which was finally

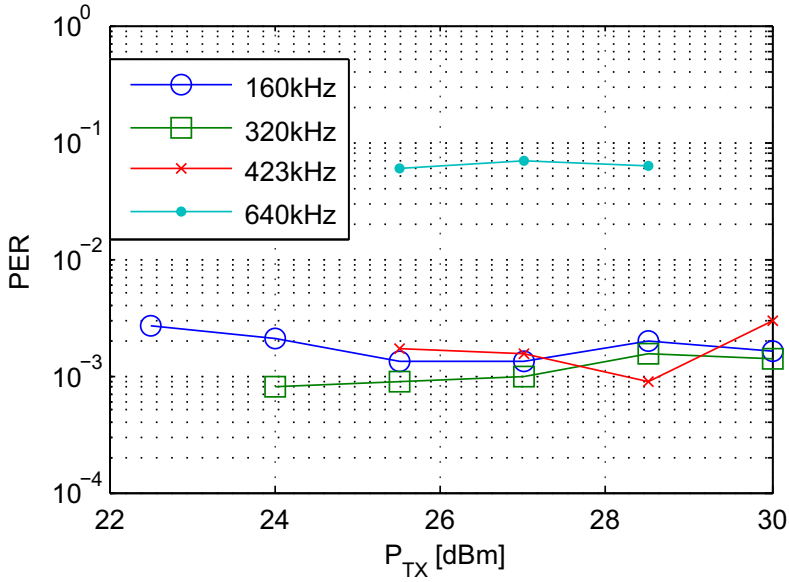

Figure 2.8: Packet Errors as a function of $\mathrm{P_{TX}}$.

solved by clocking the hardware with a very pure external source and by implementing the right digital direct synthesiser (compare with Section 3.6). Another shortcoming is the available EDA tools. Though a conversion from Matlab to VHDL is possible, sometimes it is not feasible due to the inconvenient graphic design process of complex systems. In general, up to today only basic functions are supported for the translation, and, although the process is very well suited for certain data-flow modules (such as filters or up- and downconverters), control-flow oriented blocks are not well supported by these tools. Eventually, the measured performance benchmarks clearly depend on a wide range of parameters, including the measurement environment and the performance of the underlying hardware with the RF frontends, as well as the employed specific RFID tag. As parts of the hardware are custom designs for this setup, it is difficult for other researchers to reproduce the presented results. However, it is expected that the variations are small and the qualitative behaviour of the results is unisonous.

3. RFID READER RECEIVER ARCHITECTURES

This chapter introduces receiver structures for a reader with a single receive antenna, communicating with a single tag, while the following chapters extend the architectures to multiple receive antennas (Chapter 4) and simultaneous communication to multiple tags (Chapter 5). In the following, the first Section 3.1 models signal constellations in the reader receiver baseband, and introduces the specifics of RFID signals, such as the energy supplying carrier leakage, the backscatter modulation and the data encoding. The optimal maximum likelihood receiver is presented in Section 3.2, while the rest of the chapter discusses the performance losses of the receiver due to channel estimation and due to missing synchronisation information. Furthermore, this chapter introduces the various steps of downconversion, filtering, channel estimation, synchronisation and decoding, as well as its implementation details on the rapid prototyping platform.

3.1 Model of Signal Constellations

In this section, the signal constellations at RFID reader receivers are modeled. First, the communication between reader and tag is analysed. Then, relevant definitions according to the EPCglobal standard [17], which effect the shape of the receive signals are introduced. Eventually, the constellation in the baseband of the receiver is discussed.

3.1.1 Communication between Reader and Tag

Figure 3.1 shows a tag-to-reader communication. Passive RFID tags are powered by an electromagnetic field of the RFID reader. In the LF and HF frequency domain, the tags are within the near-field of the reader. The reader and the tag form a loosely coupled transformer, and the powering field of the reader is dominantly magnetic. In the UHF frequency domain however, the tags are usually located in the far-field of the antenna of the reader and the powering field propagates to the tags [15]. If tags are within the coverage range of an RFID reader, they commutate the incoming carrier and supply their internal circuitry. At a certain level of receive power (approx. -15dBm [18]) they are ready to process information and communicate with the RFID reader.

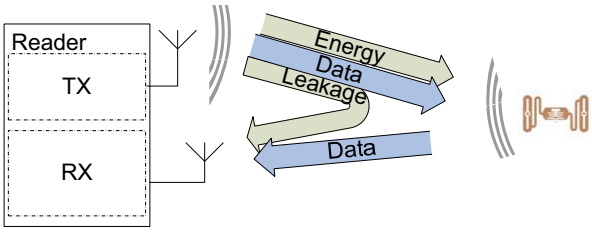

Figure 3.1: Communication between an RFID reader with a single tag.

Figure 3.2 depicts a measured communication signal between a reader and a tag. The signal was measured by an oscilloscope before sampling by the ADC at an intermediate frequency of 13.33 MHz. In RFID, the communication between reader and tag is half-duplex and initiated by the reader. The downlink (reader-to-tag) communication uses Amplitude Shift Keying (ASK) modulation and Pulse Interval Encoding (PIE) [17] or 1-out-of-4 encoding as an encoding format [116]. These encodings ensure a high amount of power supply during the communication process, since most of the time full power is transmitted to the tags (see Appendix C).

While the carrier is modulated during the downlink communication, an unmodulated carrier $s_{TX}(t)$ is provided to the tag during the rest of the time:

$$s_{TX}(t) = \sqrt{2}\sin(\omega_c t), \tag{3.1}$$

where $\omega_c = 2\pi f_c$ and f_c is the carrier frequency. The unmodulated carrier is transmitted by the reader during "pause" intervals which occur between the communication packets as indicated by T_1 in Figure 3.2 as well as during the uplink (tag-to-reader) communication. For convenience, the power of the constant transmit carrier signal is normalised to one, and the phase is set to zero.

During this entire process, the transmit signal also leaks into the receive path. While the carrier is modulated during downlink communication, the carrier leakage $s^{leak}(t)$ into the receiver is static during the rest of the time:

$$s^{leak}(t) = \sqrt{2}|L|\sin(\omega_c t + \varphi^{leak}). \tag{3.2}$$

Here, φ^{leak} is the phase shift, which results from the propagation delay between the transmit and the receive path. The amplitude $|L|$ of the leakage depends on the transmitter to receiver decoupling concept. Mono-static scenarios, apply a single, common antenna for the transmit (TX) and receive (RX) path, which are separated by a circulator or a directional coupler. Clearly, the uplink and downlink channel are expected to be strongly correlated in this case [122]. In bi-static scenarios, two separated antennas for the transmit and receive paths are employed. The amplitude of the leakage $|L|$ depends on the isolation of the circulator or directional coupler and the antenna matching in the mono-static case, and on the spatial antenna configuration in the bi-static case.

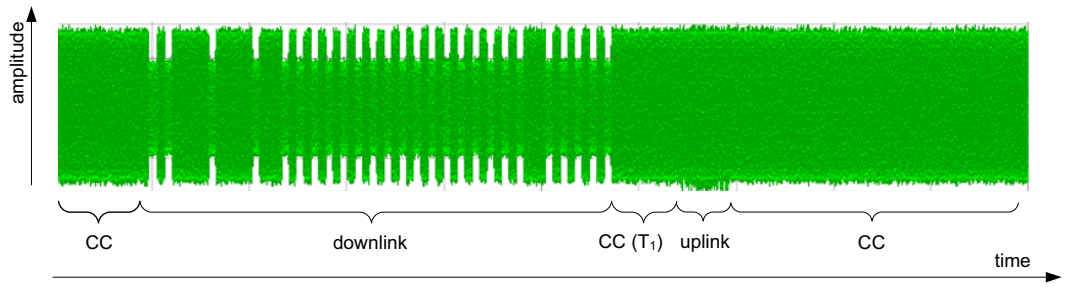

Figure 3.2: Oscilloscope screenshot of the communication signals between a reader and a tag measured before sampling by the ADC at the intermediate frequency of 13.33 MHz. Prior to the data exchange, a continuous carrier (CC) wave is transmitted to power the tag. After the downlink command, a short break of length T_1 is defined, before the tags transmit their response data.

Additionally the leakage signal $s^{leak}(t)$ includes scattered signal components from static scatters as well as the static reflection at the tag antenna. It has been quantified to be up to 65-90 dB stronger than the receive signal [123–125].

The uplink communication applies backscatter (UHF case) or load modulation (LF / HF case). During the times the tag is not communicating, the input impedance of the tag is matched to the antenna impedance for maximum energy absorption[1]. During communication cycles, the tag backscatters energy by switching its input impedance between the matched state and an unmatched state [15]. This backscattered signal at the tag is given by:

$$\begin{aligned} s_{tag}(t) &= \sqrt{2}a(t)\sqrt{|\Delta\sigma|}|h^f|\sin(\omega_c t + \varphi^f + \varphi^{\Delta\sigma}), \\ a(t) &= \sum_{k=0}^{K-1} S^k(t) * \delta(t - kT - \tau), \\ &= \sum_{k=0}^{K-1} S^k(t - kT - \tau). \end{aligned} \tag{3.3}$$

Here $|h^f|$ and φ^f denote the forward channel attenuation and phase shift. The modulation $a(t)$ switches between the matched an the unmatched state of the tag and realises an on-off keying ($a(t) \in \{0, 1\}$). It starts after a delay τ, with $S^k(t)$ being the pulse shape of the k'th encoded symbol, which is picked among the possible pulse shapes $\mathcal{S} = \{S_0(t), S_1(t), S_2(t), S_3(t)\}$. Moreover, T is the symbol period, $\delta(t)$ denotes the Dirac impulse and $*$ the convolution operation. The properties of the pulses $S_n(t)$ are discussed in the following subsection. The term $\varphi^{\Delta\sigma}$ describes the phase shift introduced by the tag modulation, while $|\Delta\sigma|$ is the normalised differential radar cross section as

[1] If the input impedance is not perfectly matched, a fraction of the received power is reflected continuously. This reflected signal contributes to the carrier leakage.

described by Nikitin et al. [118], which basically describes the modulation efficiency:

$$|\Delta\sigma| = |\rho_r - \rho_a|^2, \tag{3.4}$$

where ρ_r and ρ_a are the complex reflection coefficients for the tag's reflect and absorb state, respectively.

In the proposed model, no noise components in the forward path are considered, but all noise components are modeled additively at the receiver. Hence, at the reader receive antenna, the tag signal adds with the carrier leakage and the passband noise $n^{pb}(t)$:

$$\begin{aligned} s^{pb}(t) = \sqrt{2}|h^b|\sqrt{|\Delta\sigma|}|h^f|a(t)\sin(\omega_c t + \varphi^f + \varphi^b + \varphi^{\Delta\sigma}) \\ +\sqrt{2}|L|\sin(\omega_c t + \varphi^{leak}) + n^{pb}(t), \end{aligned} \tag{3.5}$$

where $|h^b|$ and φ^b denote the backward channel attenuation and phase shift, respectively. Figure 3.2 shows that at the reader RX antenna the tag signal is hardly visible, due to the additive carrier leakage, which is up to several magnitudes stronger.

In our system model, and for the following development of receiver architectures, I assume that both, the carrier leakage and the channel do not change significantly during the transmission of one uplink packet (block fading). During the transmission of the first uplink packet for channel arbitration in a communication with the tag, a 16 bit random number (RN16) with a 6 bit preamble is transmitted, leading to a readout time $T_{Readout} = 22\,T$ of:

$$33\mu s = 22 \cdot 1.5\mu s \leq T_{Readout} \leq 22 \cdot 50\mu s = 1.1ms, \tag{3.6}$$

where the symbol period $T = 1/\mathrm{BLF}$ (with FM0 encoding) varies from 1.5μs to 50μs according to [17], and as explained in Appendix C.

3.1.2 Baseband Signal Constellations at the Reader Receiver

At the receiver the receive signal is first downconverted to the baseband. This complex-valued baseband signal is:

$$s(t) = h^b\sqrt{\Delta\sigma}h^f a(t) + L + n(t), \tag{3.7}$$

where $h^b = |h^b|e^{j\varphi^b}$ and $h^f = |h^f|e^{j\varphi^f}$ are the complex-valued backward and forward channel coefficients, respectively, $\Delta\sigma = |\Delta\sigma|e^{j2\varphi^{\Delta\sigma}}$ is the complex-valued normalised differential radar cross section, $L = |L|e^{j\varphi^{leak}}$ denotes the static and complex-valued carrier leakage, and $n(t)$ is the complex-valued circularly symmetric additive white Gaussian noise (AWGN) with noise power spectral density N_0. Equivalently, one can reformulate Equation (3.7) to:

$$s(t) = ha(t) + L + n(t), \tag{3.8}$$

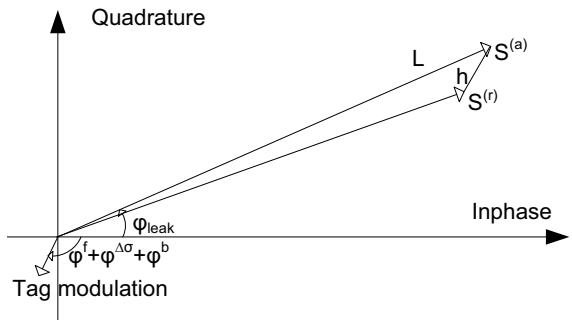

Figure 3.3: Exemplary baseband constellation at RFID reader receiver: During time periods the input impedance is well matched to the antenna impedance, the tag absorbs energy. Then, the reader finds the tag absorb state $S^{(a)}$ in its I/Q baseband plane, which is essentially the carrier leakage L. If the tag backscatters data to the reader, it unmatches its input impedance and thus reflects energy to the reader. Then, the reader encounters the tag reflect state $S^{(r)}$, which is basically composed of the channel coefficient h and the carrier leakage L.

where $h = h^f \sqrt{\Delta\sigma} h^b$ is the channel coefficient of the equivalent dyadic channel. Thus, also the modulation behaviour of the tag is modeled by the channel coefficient h.

The described RFID system features some important inherent properties:

1. The carrier frequency of both signal components at the receiver, the static carrier leakage and the reflected tag signal, is equal, as it originates from a *single* source, namely the transmitter of the reader (Equation (3.1)). As the same oscillator is also available at the receiver, a downconversion without any frequency offset is readily possible.

2. The modulation signal of UHF systems features a symbol rate, which deviates up to $\pm 22\%$ from its nominal value [17]. Additionally, the start of the modulation shows variations of the delay term τ in Equation (3.3), which is up to $\pm 22\%$ of the interval T_1. Therefore synchronisation in RFID readers is a complex and important task.

3. The tag receive signal is impaired by the carrier leakage and noise. In a practical system, the carrier leakage can be up to 65-90dB stronger than the backscattered signal [124, 126], making it necessary to estimate its extent and subtract it from the signal constellation.

Figure 3.3 shows the signal constellation in the baseband I/Q plane of the reader receiver. If the tag is absorbing energy ($a(t) = 0$ in Equation (3.8)), we find the tag absorb state $S^{(a)} = L$, which is equal to the carrier leakage. If the tag starts to modulate ($a(t) \in \{0, 1\}$ in Equation (3.8)), we find a second state in the I/Q plane, the tag

reflect state $S^{(r)} = L + h$. The location of these two states is in general arbitrary to the RFID reader receiver: first, $S^{(a)}$ depends on the extent of the carrier leakage L and second, $S^{(r)}$ additionally depends on the channel coefficient h. Hence, the reader receiver needs to estimate these two states in order to discriminate between the tag absorb and reflect states, as described in Section 3.3.

I explicitly want to stress, that in the used notation $S^{(a)}$ and $S^{(r)}$ are the two states in the I/Q plane that result from the on-off keying modulation, the carrier leakage and the channel coefficient, such that $|S^{(r)} - S^{(a)}|$ is the amplitude of the tag receive signal. This should not be confused with $S_n(t)$, which denotes the pulse shape of the symbol according to the applied FM0 encoding.

In this model I assume on-off keying on the tag, meaning that the tag absorb state $S^{(a)}$ corresponds to full absorption at the tag (that is a zero receive signal at the reader, $a(t) = 0$) while the tag absorb state $S^{(r)}$ corresponds to full reflection at the tag (that is a full receive signal at the reader, a(t)=1). This assumption fosters the picture of backscatter modulation to either absorb or reflect power. Especially during the cycles the tag is not communicating, the model assumes no reflection signal from the tag. A constant mismatch of the input impedance of the tag (also in the absorb state $S^{(a)}$) results in a component that is considered to contribute to the carrier leakage rather than to the tag response signal. The actual amplitude of the reflected signal at the tag is modeled by $\sqrt{|\Delta\sigma|}$. Other authors model the modulation without offset, for example as Binary Phase Shift Keying (BPSK) [57, 90]. That means that the one tag state corresponds to $a(t) = 1$ while the other tag state corresponds to $a(t) = -1$. As explained in the following section, due to the assumed on-off keying modulation in my model, only half of the received energy actually contributes to data transmission, while the other half of the received energy is spent for the non-zero mean modulation signal $a(t)$ in my model. In contrast to that, with the assumption of BPSK modulation all the received energy from the tags is exploited for data transmission. However, assuming BPSK modulation also implies that energy is received from the tag during cycles the tag is not communicating, which actually corresponds to one of the states, either $a(t) = -1$ or $a(t) = 1$. As this does not fit well to the physical conditions on tags, I decided to model the modulation as on-off keying, even though a 3 dB penalty due to the non-zero mean modulation signal $a(t)$ has to be accepted.

3.1.3 Definitions by the EPCglobal Standard

The information in the uplink channel is represented by the modulation signal $a(t)$ of Equation (3.3). According to the standards by EPCglobal [17, 115], the pulse shapes $S_n(t)$ follow an FM0, Manchester or Miller encoding. As the FM0 encoding features the highest data rate, the rest of the thesis concentrates on this encoding scheme. The properties of the other encoding schemes are similar, such that an extension to the other encoding schemes is straightforward. In FM0 encoding the pulse shapes $S_n(t)$ for the

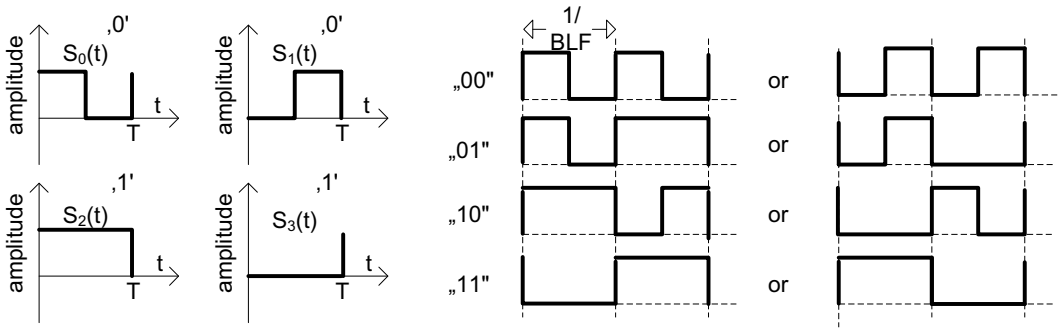

Figure 3.4: FM0 encoding in RFID uplink communications.

symbols are selected among the following pulse shapes:

$$S_0(t) = \begin{cases} 1 & 0 \leq t < T/2 \\ 0 & T/2 \leq t < T \end{cases}, \qquad S_1(t) = \begin{cases} 0 & 0 \leq t < T/2 \\ 1 & T/2 \leq t < T \end{cases},$$

$$S_2(t) = \quad 1 \quad 0 \leq t < T, \qquad S_3(t) = \quad 0 \quad 0 \leq t < T. \tag{3.9}$$

The two pulses $S_0(t)$ and $S_1(t)$ with a level transition at the half symbol period $T/2$ encode a logic '0', while the two pulses $S_2(t)$ and $S_3(t)$ without any transition within the symbol encode a logic '1'. Additionally, the symbols are arranged to feature a level transition at each symbol boundary, as depicted in Figure 3.4. That means, that for example the pulse $S_0(t)$ with a zero level in the second half symbol period can only be followed by $S_0(t)$ or $S_2(t)$, with a one level in the following half symbol period, but not by the symbols $S_1(t)$ or $S_2(t)$.

The rectangular pulse shapes of Equation (3.9) are generated by the on-off keying modulation $a(t)$, which features the offset of $E\{S_n\} = 0.5$. Furthermore, the energy per bit is $E_b = E\{(S_n)^2\} = E_c + E_a = 0.5$. Here, $E\{\cdot\}$ denotes the expected value, and $E_c = E\{S_n\}^2 = 0.25$ and $E_a = E\{(S_n - E\{S_n\})^2\} = 0.25$ denote the energy of the constant and alternating component of the modulation, respectively. The constant part E_c in fact does not carry any information. Hence, half of E_b is consumed by the non-zero mean on-off keying modulation, while only the other half of E_b (that is E_a), is used for transmitting information.

The nominal symbol duration depends on the selected encoding, and is a multiple of the inverse of the Backscatter Link Frequency (BLF). In case of FM0 encoding, the symbol period is related to the BLF by: $T = 1/\text{BLF}$. Following the EPCglobal standard for UHF RFID, the nominal value of the BLF is adjusted continuously between 40 kHz and 640 kHz, with a maximum deviation from this nominal value of up to $\pm 22\%$. Additionally the modulation of a tag may start with a certain delay, as indicated by the term τ in Equation (3.3). Following the EPCglobal standard in the HF domain, the BLF can be selected to be 423 kHz or 847 kHz. As the symbol clock in tags here is derived by dividing

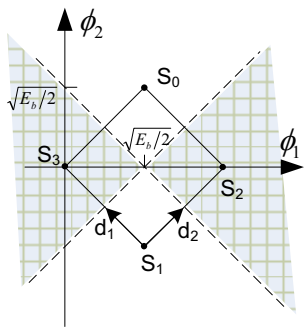

Figure 3.5: Signal space for FM0 encoded signals.

the 13.56 MHz carrier by 16 or 32, no symbol rate deviation is expected in that case. In contrast to that, UHF RFID tags exhibit an oscillator, with a relatively low frequency (for example 1.92 MHz), leading to a coarse time resolution for generating the data rate in the defined continuous frequency range from 40 kHz to 640 kHz [127, 128] (also compare with Appendix C). Moreover, the oscillator frequency shows a drift with the supply voltage[2].

3.2 Optimal Receiver

The discussion on the performance on RFID reader receivers is started with a theoretical analysis of the receiver with full knowledge about the channel coefficient, the carrier leakage and the exact symbol rate. Reviewing the definitions of the FM0 encoding and the respective pulse forms of Subsection 3.1.3, two orthogonal signal components with the basis functions $\phi_1(t) = (1/\sqrt{E_b/2})(S_2(t) - 0.5)$ and $\phi_2(t) = (1/\sqrt{E_b/2})(S_0(t) - 0.5)$ are identified. Figure 3.5 shows the four symbols S_n of the FM0 encoding in the signal space with the basis functions $\phi_1(t)$ and $\phi_2(t)$:

$$S_0 = \left(\sqrt{\frac{E_b}{2}},\ \sqrt{\frac{E_b}{2}}\right) \qquad S_1 = \left(\sqrt{\frac{E_b}{2}},\ -\sqrt{\frac{E_b}{2}}\right)$$
$$S_2 = \left(\sqrt{2E_b},\ 0\right) \qquad S_3 = (0,\ 0) \tag{3.10}$$

where

$$S_n(t) = S_n\left(\phi_1(t),\ \phi_2(t)\right)^T. \tag{3.11}$$

Here, $(\cdot,\ \cdot)$ denotes a row vector with two entries and $(\cdot)^T$ denotes the transpose of the vector.

[2] The actual deviations from τ and BLF depend on several settings in the standard, mainly the range of the selected BLF and downlink encoding value TRCal. The value of $\pm 22\%$ is the maximum value of deviations, while certain settings guarantee smaller deviations (also compare with Appendix C, Figure C.4).

The modulation signal $a(t)$ is recovered from the receive signal s(t) from Equation (3.8) by subtracting the static carrier leakage L and scaling the signal to one:

$$\hat{a}(t) = \Re\left\{\frac{h^*}{||h||^2}(s(t) - L)\right\}, \tag{3.12}$$

where h^* denotes the complex conjugate of h, and $\Re\{\cdot\}$ selects the real part. The zero-mean part of the modulation signal $a'(t) = a(t) - E\{a(t)\}$ is correlated with the zero-mean part of the various FM0 symbols $S_n^{'} = S_n - E\{S_n\}$ to yield $r_n(t)$:

$$r_n(t) = \int_0^T S_n^{'}(\tau)a'(t+\tau)d\tau. \tag{3.13}$$

With the assumption of additive white Gaussian noise, the symbol-by-symbol maximum likelihood (ML) decoder decides on the k'th receive symbol $S^k \in \{S_0, S_1, S_2, S_3\}$ by:

$$\hat{n} = \arg\max_n r_n[k], \quad \hat{S}^k = S_{\hat{n}}, \tag{3.14}$$

where $r_n[k]$ is $r_n(t)$ sampled at $t = kT$.

With the constellation as shown in Figure 3.5, a bit error conditioned on the transmitted symbol S_1 occurs if the received symbol is located in the shaded regions. As the symbols S_1 and S_0 encode the same bit, no symbol error occurs if the received symbol is located in the decision region of S_0. Hence, the conditional probability of an error $P(e|S_1)$ is:

$$P(e|S_1) = P(d_1 > \sqrt{E_b}/2)P(d_2 < \sqrt{E_b}/2) + P(d_1 < \sqrt{E_b}/2)P(d_2 > \sqrt{E_b}/2) \tag{3.15}$$

As the error probability conditioned on the other symbols is equal, the bit error probability P_b of the symbol-by-symbol ML receiver is:

$$P_b = 2Q\left(\sqrt{\frac{E_b}{2N_0}}\right)\left(1 - Q\left(\sqrt{\frac{E_b}{2N_0}}\right)\right), \tag{3.16}$$

with $Q(\cdot)$ denoting the Q-function. The pink curve in Figure 3.9 plots this function (labeled as "ML symbol-by-symbol decoder"). Note that authors who assume binary Pulse Amplitude Modulation (PAM) instead of on-off keying [57, 90] achieve a 3 dB better result, as the modulation signal $a(t)$ is zero mean in that case (compare with Section 3.1).

As due to the encoding rules each symbol can only be followed by certain symbols (those which generate a level transition at the symbol boundaries), an inter-symbol correlation is exhibited. The performance of the receiver is further improved by taking into account this inter-symbol correlation, which results in the ML sequence decoder. Considering the structure of the FM0 encoding (Figure 3.4), three methods for exploiting this inter-symbol correlation are identified:

- First, to realise the ML sequence decoder, the Viterbi decoder is applied to the FM0 encoding, resulting in a performance gain of 3 dB [57].
- One however notices, that the inter-symbol correlation just affects the preceding and trailing half symbol, which is essentially known. Thus a performance increase of 3 dB is also exploited, if the receive sequence is correlated with a reference symbol extended to the preceding and trailing half symbol, which doubles the correlation length. Due to this specific characteristic of the encoding, this extended correlation in fact also realises the ML sequence decoder.
- Eventually, a third solution to benefit from the inter-symbol correlation is shown by Simon et al. [90]: At the symbol boundaries t=kT-T/2, the encoding always defines a level inversion. A positive or negative edge is detected by considering the correlation with the reference pulses $S_0(t)$ and $S_1(t)$ at t=kT-T/2, respectively. By means of differentially decoding these values, the available 3 dB gain is realised. This structure is basically identical with the above described structure of the extended correlation length to the preceding and following half symbols.

The realised performance of these three methods under AWGN conditions hence is (plotted in blue in Figure 3.9 and labeled as "ML sequence" decoder):

$$P_b = 2Q\left(\sqrt{\frac{E_b}{N_0}}\right)\left(1 - Q\left(\sqrt{\frac{E_b}{N_0}}\right)\right), \tag{3.17}$$

showing the achievable performance of the ML sequence decoder with full knowledge of the channel coefficient, the carrier leakage and full synchronisation information. In the following sections the performance loss of receivers without channel knowledge (Section 3.3) and without perfect synchronisation (Section 3.4) is shown.

3.3 Channel Estimation

Reviewing Equation (3.8), the tag signal of interest is degraded by the static carrier leakage and the noise. While the tag signal is only present during times of backscatter modulation, the carrier always leaks into the receiver (compare with Figure 3.2). The carrier leakage is estimated during an interval the tag is absorbing energy (that is the tag state $S^{(a)}$). Such a period is defined in [17] (and similarly by others) immediately before the start of the uplink communication (defined as T_1). The proposed receiver estimates the carrier leakage $L = S^{(a)}$ and the noise power σ_n^2 as the temporal mean $E\{\cdot\}_{T_1}$ and temporal variance during this interval T_1:

$$\begin{aligned} \hat{S}^{(a)} &= E\{s(t)\}_{T_1}, \\ \hat{\sigma}_n^2 &= E\{|s(t) - S^{(a)}|^2\}_{T_1}. \end{aligned} \tag{3.18}$$

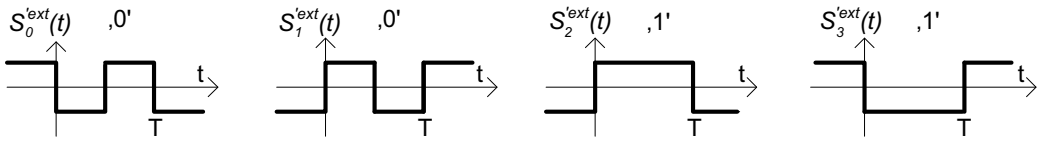

Figure 3.6: Extended zero-mean reference pulse forms $S_n^{'ext}(t)$.

The first symbol of the preamble of the uplink sequence is symbol S_2. Hence, the tag realises its reflect state $S^{(r)}$, which is estimated as the temporal mean $E\{\cdot\}_{t_{1symb}}$ during the interval of the first symbol t_{1symb}:

$$\hat{S}^{(r)} = E\{s(t)\}_{t_{1symb}}. \tag{3.19}$$

As in our model any artifacts of the tag that deviate from perfect on-off keying are reflected by the term $\Delta\sigma$ which are included in the channel coefficient, the channel coefficient directly calculates to:

$$\hat{h} = \hat{S}^{(r)} - \hat{S}^{(a)}. \tag{3.20}$$

The performance of the estimation scheme is plotted in green and labeled as "channel estimation" in Figure 3.9.

3.4 Synchronisation and Decoding

As shown in Section 3.2, the receive pulse forms exhibit an orthogonal part. This orthogonality is exploited by the described synchronisation schemes, utilising correlations with the various reference symbols. The ML sequence decoder performance is realised by an equivalent symbol-by-symbol decision on these extended correlation values r_{ext}^n, as discussed above:

$$r_n^{ext}(t) = \int_{-T/2}^{3T/2} S_n^{'ext}(\tau) a'(t+\tau) d\tau, \tag{3.21}$$

with the zero-mean part of the FM0 encoded extended pulse forms $S_n^{'ext}(t)$, as depicted in Figure 3.6:

$$S_0^{'ext}(t) = \begin{cases} 0.5 \text{ if } 0 \leq t < T/2 & \text{and} \quad T < t \leq 3T/2 \\ -0.5 \text{ if } -T/2 \leq t < T & \text{and} \quad T/2 \leq t < T \end{cases}, \qquad S_1^{'ext}(t) = -S_0^{'ext}(t),$$

$$S_2^{'ext}(t) = \begin{cases} -0.5 \text{ if } -T/2 \leq t < 0 & \text{and} \quad T \leq t < 3T/2 \\ 0.5 \text{ if } 0 \leq t < T \end{cases}, \qquad S_3^{'ext}(t) = -S_2^{'ext}(t). \tag{3.22}$$

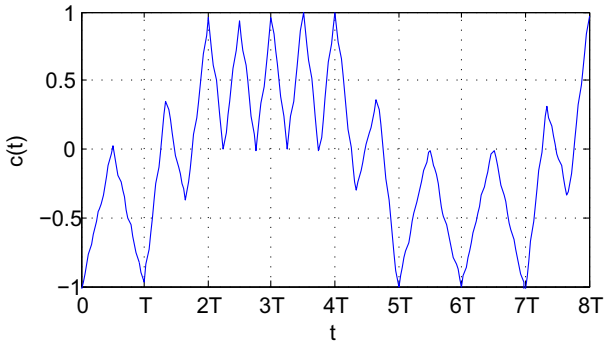

Figure 3.7: Correlation function $c(t)$ at $E_b/N_0 = 30$dB. If $c(kT)$ is positive, the ML decoder decides on zero, otherwise on one, such that the decoded sequence in the figure is "110001110".

As in the rest of the thesis, except explicitly stated differently, only the correlation with the extended pulse form is considered, the superscript of $r_n^{ext}(t)$ and $S_n^{'ext}$ is skipped for better readability, and $r_n(t)$ and $S_n^{'}$ denote the correlation value and zero-mean extended pulse form as defined in Equation (3.21) and Equation (3.22), respectively.

The characteristics of the FM0 encoding result in $r_0[k] = -r_1[k]$ and $r_2[k] = -r_3[k]$ for the two pulse forms encoding a logic '1' and a logic '0', respectively. Thus, considering the absolute values of the correlation values r_n, leads to the same outputs for both pulses encoding a zero and both symbols encoding a one. Furthermore, I define the correlation function $c(t)$ as depicted in Figure 3.7 as:

$$c(t) = \frac{2}{T}\left(|r_0(t)| - |r_2(t)|\right). \tag{3.23}$$

Thus, the ML decision is thus reformulated to:

$$c[k] \begin{cases} > 0 & \ldots \text{ '0'} \\ \leq 0 & \ldots \text{ '1'} \end{cases}, \tag{3.24}$$

with $c[k]$ denoting $c(t)$ sampled at $t = kT$.

Figure 3.8 shows the eyediagram of the correlation function $c(t)$. It shows, that the correlation with the pulses $S_0(t)$ and $S_1(t)$, encoding a zero, does not only feature peaks at the ideal sampling points $t = kT$, but also at $t = kT + T/2$. This becomes obvious when observing a sequence of pulses encoding a zero, as depicted in Figure 3.4.

In general neither the symbol frequency T, which is subject to the strong deviation of $\pm 22\%$, nor the exact sampling timing are known to the reader. Before introducing different synchronisation concepts, the performance loss due to an incorrect sampling time instant is discussed. A sampling timing offset of $\Delta T = T/20$ and $\Delta T = T/10$ already lead to losses of E_b/N_0 of $0.8^2 = 0.64 = -1.9$ dB and $0.6^2 = 0.36 = -4.4$ dB,

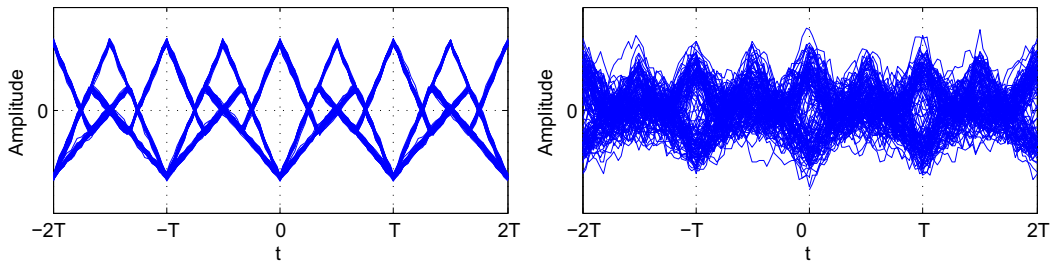

(a) Eyediagram, $E_b/N_0 = 30\,\text{dB}$ (b) Eyediagram, $E_b/N_0 = 10\,\text{dB}$

Figure 3.8: Eyediagram of correlation function $c(t)$ at $E_b/N_0 = 30\,\text{dB}$ and $E_b/N_0 = 10\,\text{dB}$.

respectively, assuming only pulses encoding a zero are transmitted. Even at a very small sampling timing offset, a relatively high fraction of E_b/N_0 is lost. The reason of this high loss compared to other modulation schemes is the use of the encoding together with the rectangular shaped pulses of the on-off keying modulation, producing the triangular shaped correlation function $c(t)$ with its intermediate peaks. The brown curve in Figure 3.9 shows the performance loss for a sampling time offset of $\Delta T = T/10$ (labeled as "timing offset $\Delta T = T/10$).

In general synchronisation mechanisms are distinguished into maximum likelihood timing recovery [129] and Minimum Mean Square Error (MMSE) methods [93, Chapter 16]. While the first class estimates the timing instant as the value, maximising the likelihood function $L(c|\tau)$, the latter estimates the timing instant by minimising the mean square error. In order to achieve a better estimate, several symbols for ML timing recovery are taken into account. This averaging however requires knowledge about the exact symbol period.

3.4.1 Estimation of the Symbol Period

An estimation of the symbol period using the MUltiple SIgnal Classification algorithm (MUSIC) is proposed. The MUSIC algorithm is well suited to estimate the frequency components of a sum of sinusoidal signals in presence of noise, based on a decomposition of the autocorrelation matrix into a signal subspace and a noise subspace [130, 131]. In order to obtain a signal with a strong component of the symbol frequency, an extended preamble is requested for tag uplink signals. This option can be selected by the reader when requesting data from the tag, resulting in an additional 16 symbols encoding a zero before the general preamble. The MUSIC algorithm is applied on this extended preamble signal, thus the signal subspace for the MUSIC algorithm is just one-dimensional. For the simulation results shown below, the `rootmusic` function of Matlab has been used.

3.4.2 Estimation of the Sampling Time Instant

With an estimate of the symbol period, an ML estimate of the optimal sampling instant in the eyediagram is computed, considering K observed received symbols. Consider the correlation signal c(t) with the time offset ς oversampled by a factor of OSR:

$$\begin{aligned} c[\nu] &\triangleq c(kT + \upsilon T/OSR - \varsigma) \\ &= c\left((k \cdot OSR + \upsilon)T/OSR - \varsigma\right) \\ &= c\left(\nu \frac{T}{OSR} - \varsigma\right), \end{aligned} \tag{3.25}$$

with $\upsilon \in [0 \ldots OSR-1]$. The sampling and symbol index are denoted by $\nu = k\,OSR+\upsilon$ and $k \in [0 \ldots K-1]$, respectively. Then, the offset from the optimal sampling instant in the eyediagram is estimated by searching for the maximum absolute value of the averaged symbol pulses:

$$\hat{\varsigma} = \hat{\upsilon} = \arg\max_{\upsilon} \sum_{k=0}^{K-1} |c[\upsilon + k\,OSR]|\,. \tag{3.26}$$

The sum in the above equation essentially delivers a maximum likelihood estimate for the mean $\mu(\upsilon)$ of K observed symbols, at the time instant υ: $\hat{\mu}(\upsilon) = \sum_{k=0}^{K-1} |c(\upsilon+k\,OSR)|$. The timing offset υ resulting in the maximum mean $\mu(\upsilon)$ indicates the widest opening in the eyediagram and hence serves as the timing offset estimate.

The black curve with the label "timing estimation" in Figure 3.9 shows the performance of the sampling time instant estimation, with knowledge of the exact symbol period, and $K = 16$. If additionally the symbol period is estimated using the MUSIC algorithm, the performance of the red curve is achieved (labeled as "frequency and timing estimation"). As expected, this sampling time instant estimation is very sensitive to the exact knowledge of the symbol period. If the symbol period estimate is imprecise, the timing instant estimate may become completely wrong, and then the entire packet is decoded incorrectly. Thus, for the red curve with the label "frequency and timing estimation" in Figure 3.9, the errors are heavily concentrated within a few packets with a wrong symbol period (and thus timing) estimate.

Clearly, the advantage of this synchronisation method is that it is less sensitive to disturbance by noise, due to the averaging over K symbols. However, the algorithm also has two major drawbacks:

- Before any potential timing offset is estimated, an accurate estimate $\hat{T}$ of the symbol period is required. A wrong estimate of the symbol period severely influences the performance of the estimation of the sampling time instant. Additionally, the proposed symbol period estimation requires the use of the optional pilot sequence.

- The synchronisation algorithm requires K symbols of the receive sequence. Thus, the receiver has to wait for K symbols, before it can start to synchronise and decode even the first symbol, resulting in a delay KT. In a real-time system this is often not feasible, but the data is required at latest at a certain delay, which is also called the real-time constraint. According to the EPCglobal standard for UHF RFID [17], the minimum response time of the reader to a received packet is three symbols only. Furthermore, hardware devices such as FPGAs are well suited for data-flow oriented and pipelined designs. The above proposed algorithm is not well suited for a low complexity implementation on such a device as it requires to massively delay the receive sequence by K symbols before the decoder starts. Therefore, Section 3.6 introduces different synchronisation algorithms, that are better suited for a real-time implementation but which tradeoff the performance of the synchronisation.

Additionally, a synchronisation by MMSE techniques has been considered in simulation, according to the stochastic gradient algorithm as described by Barry et al. [93, Chapter 16]. However the performance showed to be worse than the performance of the presented ML technique, and thus was not further considered. In this adaptive algorithm, a small stepsize α guarantees an inertial adaption and thus is less sensitive to noise, which contradicts a fast adaptation to a strong symbol timing offset within a few bits of the preamble. Figure 3.9 shows the performance of the stochastic gradient algorithm for $\alpha = 1/8$, which results in a maximum sampling offset correction of $\Delta\tau_{max} = T/16$ per symbol (labeled as "MMSE $\alpha = 1/8$).

3.5 Performance Simulations

This section compares the performance of the symbol-by-symbol ML decoder and the ML sequence decoder with full knowledge of the channel state and full synchronisation information. Additionally, the performance losses due to the various estimators from this optimal receivers are discussed. The simulated channel is an AWGN channel.

For the simulation, RN16 packets with 16 bit random data and a preamble are considered. Such packets are standardised for the Framed Slotted Aloha (FSA) arbitration scheme of tags, which is executed as the first uplink command in an RFID communication (see Appendix C). A BLF of 625 kHz is selected for the simulation. The Carrier leakage to Signal Ratio (CSR) is set to 70dB.

Figure 3.9 shows the simulation results: The blue and pink curve are the calculated performance results of the ML sequence (Equation (3.17)) and symbol-by-symbol ML (Equation (3.16)) decoder, respectively. The green curve shows the losses of the channel estimation according to Equation (3.19), while the brown curve shows the impact of a sampling time offset of $\Delta T = T/10$, which already leads to a performance loss of almost 4 dB, which demonstrates the influence of improper synchronisation. The black curve

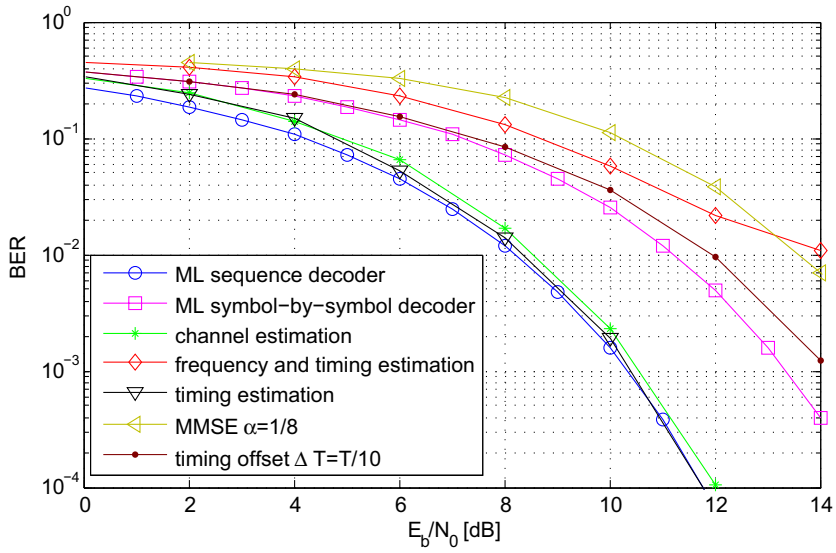

Figure 3.9: Simulated performance of receivers: "ML sequence decoder" is the theoretical performance of the ML sequence decoder according to Equation (3.17), "ML symbol-by-symbol decoder" plots the performance according to Equation (3.16). "Channel estimation" is the ML sequence decoder with channel estimation as presented in Section 3.3. The curve labeled "timing offset $\Delta T = T/10$" is the performance of the ML sequence decoder with an artificially introduced timing offset of $\Delta T = T/10$. The curve with the label "timing estimation" depicts the performance of the ML sequence decoder with estimation of the timing instant according to Equation (3.26). "Frequency and timing estimation" additionally estimates the symbol period by means of the MUSIC algorithm. Eventually, "MMSE $\alpha = 1/8$" plots the performance of the stochastic gradient timing recovery according to [93], with the stepsize α=1/8 for comparison.

illustrates the performance of the sampling timing estimation with perfect knowledge of the symbol period according to Equation (3.26), and the red curve shows additionally the losses due to the symbol period estimation according to Equation (3.24). Although the MUSIC algorithm estimates the symbol period accurately, the timing recovery completely fails in case of a wrong estimation, leading to the total performance loss of approximately 5 dB. The curves only show the influence of the estimation of the described value, while the receiver possesses full knowledge about the remaining parameters.

3.6 Implementation Aspects

This section covers implementation specific considerations of the digital architecture, such as real-time issues and hardware optimised implementations. A block diagram of the entire reader architecture is shown in Figure 3.10.

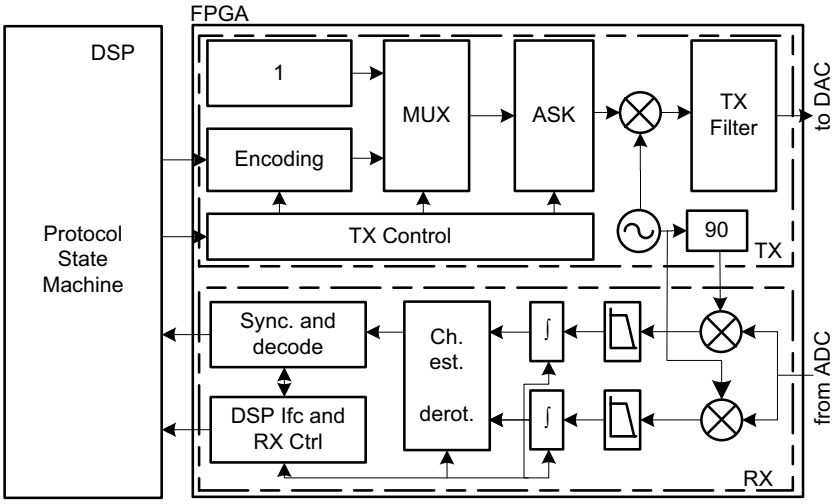

Figure 3.10: Block diagram of the RFID reader architecture.

The transmitter covers the PIE data encoding and continuous carrier generation, the ASK modulation, upconversion and transmit filtering. The encoding and modulation settings can be controlled according to the definitions of the standards and are accessible via registers from the controlling software running on the DSP. The list of registers and accessible parameters is given in Appendix E.

The receiver first downconverts the receive signal using an I/Q downconverter and low pass filters. Each stream is subsequently integrated, which realises the matched filtering. Then, the receiver estimates the constellation points of the absorb and reflect state of the tag in its I/Q plane and equalises the channel. Finally, the receive signal is synchronised and decoded. An RX control block configures the settings of various blocks via registers, which are accessible from the DSP software (Appendix E). As the ADCs exhibit 16 bits and several embedded hardware blocks on the FPGA such as multipliers and memories can be configured with a resolution of 16bits, this bitwidth is used for all buses connecting the subsequent blocks. Appendix D shows measured signals at the output of the single units of the receiver as depicted in the block diagram of Figure 3.10.

3.6.1 Downconversion and Low Pass Filtering

As previously mentioned, backscatter or load modulation offer the advantage, that only one single carrier frequency is present in the system, and hence a downconversion without any frequency offset compensation is feasible. The downconversion can be either realised in the analogue or digital domain [132]:

- Downconversion in the analogue domain: The digital part of the test system generates the baseband signal, and up- and downconversion are achieved in the analogue domain. This approach has the disadvantages of a potential I/Q im-

balance of analogue I/Q demodulators, and two required ADCs for sampling the inphase and quadrature parts. On the other hand, the benefit of this approach is a lower sampling rate ADC and less complexity in the digital domain.

- Up- and downconversion to an intermediate frequency in the digital domain: The digital part upconverts the transmit signal and downconverts the receive signals with an I/Q downconverter to a suitable intermediate frequency that is supported by the DAC and ADC update rate. The up- and downconversion to the target frequency is achieved in the analogue domain. This approach features less I/Q imbalance and just requires a single ADC at the receiver, which samples the intermediate frequency signal. The tradeoff of this approach is the higher required sampling rate to support the selected intermediate frequency [133].

The target hardware exhibits two DACs and two ADCs running synchronously at a sampling frequency of 40 MHz. As the scope of the setup also foresees the implementation of dual receive antenna architectures, I decided for a digital up- and downconversion to an intermediate frequency of 13.33 MHz for the UHF system and directly synthesize 13.56 MHz for up- and downconversion of the HF system. These selected interface frequencies of the digital part are located well within the supported range of the DACs and ADCs.

For the generation of the 13.56 MHz sinusoid of the HF system a Direct Digital Synthesiser (DDS) IP core from Xilinx [134], configured with the Xilinx CoreGenerator, is used. This DDS consists basically of a high precision phase accumulator, a phase quantizer and a look-up table with samples of a sine. The phase truncation is required to limit the address space of the look-up table. The truncated phase $\theta(t)$ is:

$$\theta(t) = \Theta(t) + \epsilon(t), \tag{3.27}$$

where $\Theta(t)$ is the desired phase increment and $\epsilon(t)$ is the phase error due to phase truncation, which has a sawtooth shape [135]. The error signal $\epsilon(t)$ generates spurious emissions in the spectrum of the DDS. The ratio S of the carrier to the maximum spurious emission is [135, 136]:

$$S = 3.992 - 6.02\,m\,\text{dB}, \tag{3.28}$$

where m is the address width of the look-up table. By randomising the phase error by using a technique known as dithering [137], the energy of these spectral spikes is spread across the entire spectrum, with the benefit of lower spectral spikes.

Furthermore, the finite bitwidth n of the look-up table results in an additional quantisation noise term described by SNR $= -6.02\,n - 1.76\,\text{dB}$. Hence, for the HF system, a look-up table with address bitwidth $m = 13$ and output bitwidth $n = 16$, leading to a size of $2^m \times n = 4096 \times 16$ bit, has been selected to achieve a reasonable trade off

between performance and complexity.

UHF RFID systems however impose more stringent conditions on the performance, due to the higher read range and therefore potentially weaker receive signals, leading to a higher carrier to receive signal ratio CSR. As mentioned in Section 3.1, the carrier to receive signal ratio may be as large as 90 dB. In order to achieve a reasonable SNR at the receiver, the carrier noise terms should be well below the CSR. The required bit widths for a carrier to noise ratio of 95 dB for example results in $n = 16$ bit and $m = 17$ bit, leading to a look-up table size of $2^m \times n = 2^{17} \times 16\text{bit} = 262144$ bytes, which exceeds the capacity of conventional FPGAs. Therefore, the intermediate frequency for the UHF system implementation was chosen at 13.333 MHz, which is exactly a third of the 40 MHz clock frequency. Thus, the I/Q synthesiser does not feature phase noise due to truncated memory addresses and only requires $2 \times 3 = 6$ entries with a bit width of $n = 16$.

The I/Q downconversion of the receive signal at $f_c = 13.333$ MHz (Equation (3.5)) by a multiplication with a sine and cosine wave generates signal components in the baseband and at the double carrier frequency $2f_c = 26.666$ MHz:

$$s_I(t) = s^{pb}\sqrt{2}\cos(\omega_c t) = [|h|a(t)(\cos(\varphi) - \cos(2\omega_c t)) + |L|(\cos(\varphi) - \cos(2\omega_c t))],$$
$$s_Q(t) = s^{pb}\sqrt{2}\sin(\omega_c t) = [|h|a(t)(\sin(\varphi) + \sin(2\omega_c t)) + |L|(\sin(\varphi) + \sin(2\omega_c t))].$$

Due to aliasing, the components at the double carrier frequency reappears at a frequency of $f_s - 2f_c = 40$ MHz $- 26.666$ MHz $= 13.333$ MHz, where f_s denotes the 40 MHz sampling frequency. This undesired component is eliminated by a low pass filter. An extremely low complexity low pass filter cutting off the undesired component is realised by:

$$h_{LP}[\nu] = \frac{1}{3}\sum_{m=0}^{2}\delta[\nu - m], \qquad H(\theta) = \frac{1}{3}(1 + e^{j\theta} + e^{j2\theta}), \tag{3.29}$$

which shows a zero at $f_s/3$ and $2f_s/3$. Here, ν is the sample index, $h_{LP}[\nu]$ and $H(\theta)$ denote the discrete time impulse response and the transfer function of the low pass filter, respectively. The transfer function shows a zero exactly at the undesired frequency component and is sufficiently flat in the baseband.

The shape of the signals after the multiplication with the sine and after the low pass filtering during a communication with the tag in a measurement scenario is depicted in Appendix D.

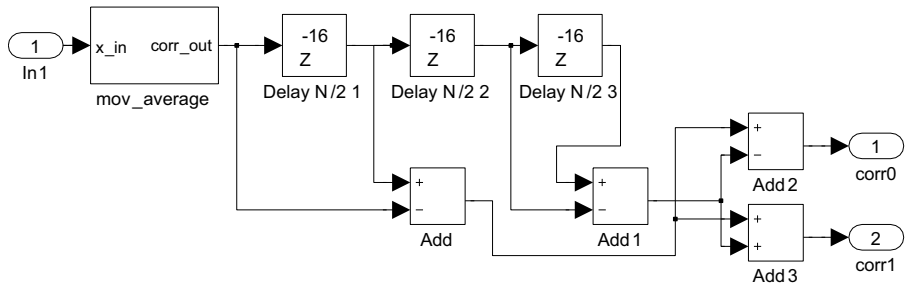

Figure 3.11: Implementation of correlations based on one moving average and FIFOs in Simulink.

3.6.2 Matched Filtering

Reconsider Equation (3.21), which can be reformulated to:

$$r_n^{ext}(t) = \int_{-T/2}^{0} S_n'^{ext}(\tau)a'(t+\tau)d\tau + \int_{0}^{T/2} S_n'^{ext}(\tau)a'(t+\tau)d\tau$$
$$+ \int_{T/2}^{T} S_n'^{ext}(\tau)a'(t+\tau)d\tau + \int_{T}^{3T/2} S_n'^{ext}(\tau)a'(t+\tau)d\tau. \quad (3.30)$$

As the reference symbols are constant in each of the intervals of the individual integrals, the integration in fact averages the receive signal over half a symbol period. Such an integration is efficiently implemented as a moving average in hardware, requiring only one adder and one subtracter and a First In, First Out (FIFO) memory of depth $T/2$. As the symbol duration T is subject to wide variations, the FIFO depth shows the same variations. Additionally, one realises that the absolute value of the second, third and fourth integral are shifted versions of the first one, and thus are obtained by delaying the result of the first moving average block. Depending on the reference symbol, the outputs of the four stages are added and subtracted as shown in Figure 3.11.

The FIFOs of the structure are implemented on embedded block RAM on the FPGA. Their fill-level is controlled by the RX control block, according to the BLF settings.

The structure can easily be extended to support Miller and Manchester encoding schemes as well, by adding additional delay lines to meet the required symbol length and adjusting the adders and subtracters accordingly.

The block with the integration sign in Figure 3.10 denotes the moving average block for the first integral of Equation (3.30). The delays for realising the other integrals are implemented after the channel estimation and derotation circuit. This circuit estimates the constellation points of the tag's reflect and absorb state, subtracts the carrier leakage, and derotates the constellation to the inphase component (compare with Equation (3.12) and the following section). Hence, the output of the circuit is real-valued and thus only the inphase component is considered for the calculation of the correlation. This saves

the delay lines for the quadrature component.

The shape of the integrated and derotated signals is shown in Appendix D.

3.6.3 Channel Estimation

In the implemented architecture, the channel estimation is slightly changed compared to the method proposed in Section 3.3, as Equation (3.19) on the one hand requires accurate knowledge of the interval of the first symbol, and, on the other hand, information if there is a tag response at all, which is in general unknown at the receiver [88]. Before the channel estimation, the signal is integrated. This integration changes the modulation pulses from rectangular to triangular. Figure 3.12 shows the shape of a receive signal in inphase and quadrature component in the plots (a) and (b), respectively. The data was captured during a measurement on the rapid prototyping system. Note the strong amplitude offset, which corresponds to the carrier leakage.

First, the receiver estimates the absorb state $S^{(a)}$ and the noise power $\hat{\sigma}_n^2$ during the time period T_1 as the temporal mean and variance of the receive symbols, as proposed by Equation (3.18). The baseband samples are Gaussian distributed around the absorb state during this period, with a variance equal to the noise spectral density N_0 (compare with plot (c) of Figure 3.12). The receiver defines a circular region around the estimated absorb state $\hat{S}^{(a)}$. The radius r_{absorb} of this region is a design parameter which is proportional to the estimated standard deviation $\hat{\sigma}_n$ (for example $r_{absorb} = 3\hat{\sigma}_n$ in plot (c) of Figure 3.12). If only the noisy carrier leakage is received, a receive sample is located within this region with a probability of $1 - e^{-(r_{absorb})^2/2\sigma_n^2}$. As the noise follows a circularly symmetric Gaussian random process, its amplitude is Rayleigh distributed with the same variance. Thus, the above probability for a sample being located inside the circular region is the Cumulative Density Function (CDF) of the Rayleigh distribution at r_{absorb}/σ_n. However, if a tag response packet is received, the receive samples move to the tag's reflect state, which is located, depending on the E_b/N_0, outside this region. Hence, when an uplink packet is expected, the start of frame is estimated by the time instant the first sample leaves the region around the carrier (plots (c) and (d) of Figure 3.12).

The radius r_{absorb} of the region has a crucial impact: if it is chosen too small, the start of frame may be estimated incorrectly, or even if no tag responds, the receiver starts to decode on the noise. If it is chosen too large however, and only a weak tag signal is received, the receive samples may not move outside the specified region and the receive sequence remains undetected.

As soon as a modulation on the channel is detected, the reflect state $\hat{S}^{(r)}$ of the tag is estimated at the furthest distance from the absorb state $\hat{S}^{(a)}$, during the first symbol period:

$$\hat{k} = \arg\max_k \left| s[k] - \hat{S}^{(a)} \right|_{t_{1symb}}, \quad \hat{S}^{(r)} = s[\hat{k}]. \tag{3.31}$$

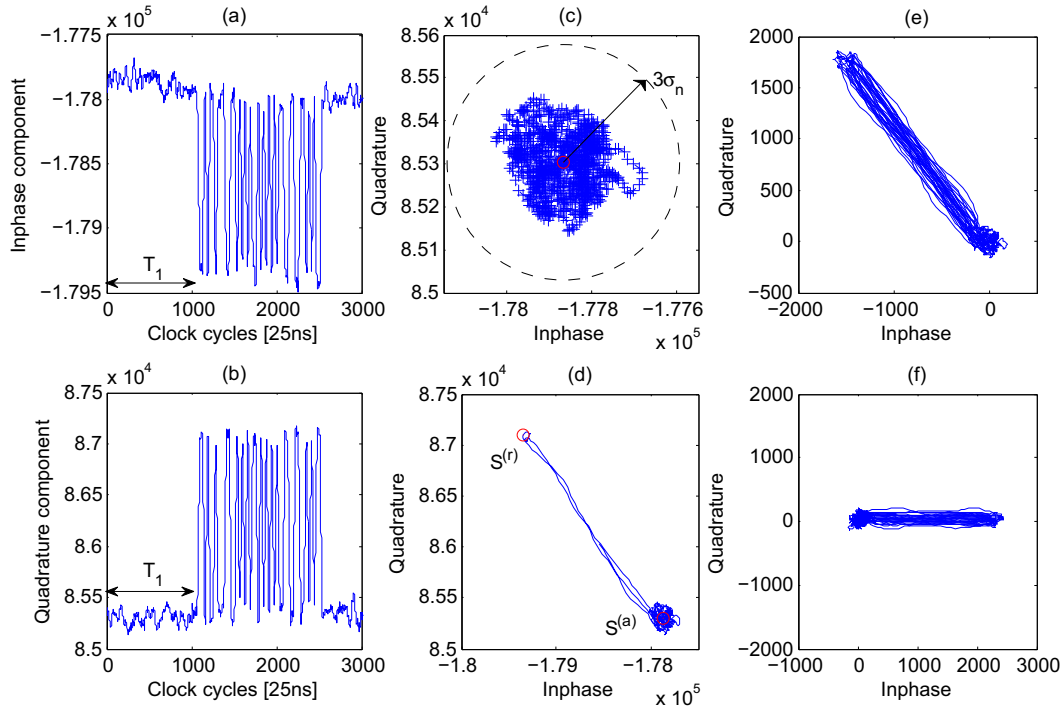

Figure 3.12: Channel Estimation shown on basis of measured receive signals by the rapid prototyping system: (a) Inphase component of receive signal. (b) Quadrature component of receive signal. (c) I/Q constellation during period T_1, estimated carrier leakage (red) and defined region with radius $r_{absorb} = 3\hat{\sigma}_n$. (d) Estimation of reflect state during first receive symbol. (e) I/Q constellation of receive signal with subtracted carrier leakage. (f) I/Q constellation of derotated receive sequence.

Note that, if the optimal sampling instant k is known, the estimator is similar to the one in Equation (3.19), as the moving average outputs the temporal mean over the first half symbol at time instant[3] k. However, this first symbol interval is unknown at the receiver. Thus, the sampling time instant k is first estimated and thereafter the corresponding mean value is taken as the estimate for $S^{(r)}$. Furthermore, the estimation of the first sampling instant $\hat{k}$ may be considered as the estimation procedure described by Equation (3.26), with an averaging over only $K = 1$ symbols. Therefore, the real-time processing capability of this method is traded off with an increased variance of the estimator.

Additionally, the receiver estimates E_b as:

$$\hat{E}_b = |\hat{S}^{(r)} - \hat{S}^{(a)}|^2, \tag{3.32}$$

[3] In Equation (3.19) in contrast I average over the entire symbol. As discussed in the previous section, the integration block before the channel estimation computes the half symbol temporal average, as this is the common part for all possible pulses $S_n(t)$ (see Figure 3.11).

and thus also computes an estimate of $\hat{E}_b/\hat{N}_0$, which is $28.2\,\text{dB}$ for the measurement data applied in Figure 3.12.

Compared to the previously proposed channel estimation method, this method suffers from the following drawback: The estimation of the reflect state requires the knowledge of its sampling time instant, which is estimated by Equation (3.31). While this estimation is unbiased, the estimation of the $S^{(r)}$ tends to an overestimation due to the maximum in Equation (3.31) and the single observation for the estimation of $\hat{k}$.

As soon as both states of the constellation are estimated, the receiver first subtracts the carrier leakage ($\hat{S}^{(a)}$), which shifts the constellation to the origin (plot (e) in Figure 3.12). Thereafter, the constellation is derotated to the real axis (plot (f) in Figure 3.12). This derotation is achieved by a COrdinated Rotation Integrated Circuit (CORDIC) algorithm on the FPGA [138]. The implemented CORDIC uses eight stages. If the reflect state $S^{(r)}$ is in the first or third quadrant at a certain stage, the CORDIC rotates counterclockwise, if it is in the second or fourth quadrant, the CORDIC rotates clockwise. Thereby a rotation to the real axis is achieved. Subsequently only the quadrature component further processed.

The channel estimation and derotation essentially realise the computation of Equation (3.12), except of the normalisation. The complex multiplication with h^* causes a rotation to the real axis, which is realised by the CORDIC algorithm. It is implemented as a finite state machine (FSM), as shown in Figure 3.13. The implementation requires two multipliers, which are utilised in various stages of the algorithm: first for determining the noise variance, later for computing the distance of samples from the estimated symbol $S^{(a)}$, and eventually for searching for symbol $S^{(r)}$.

The state transition from *Idle* to *Delay* is enabled after a command has been sent to the tag. The algorithm remains in the *Delay* state for time t_d, computed as total response between reader and tag commands T_1 minus the greatest power of two value $t_{2max} < T_1$: $t_{2max} = \lfloor \log_2(T_1/T_{clk}) \rfloor T_{clk}$. The value $t_{2max} = T_1 - t_d$ then serves in the state *Detect* $S^{(a)}$ to estimate the symbol $S^{(a)}$. Hence, the number of cycles remaining in this state is a power of two, which facilitates the divisions for the calculation of mean and variance of the receive samples. The EPC global standards [17, 115] define a minimum period T_1 to allow $512 \leq t_{2max} \leq 2048$ at the clock frequency of 40 MHz. The following state is *Find* $S^{(r)}$, which searches for samples outside the region in which only noise is expected. If no samples are detected in this region of interest, it is assumed that there are no tags present in the interrogator's read range. Thus the FSM switches back to the *Idle* state. Otherwise the FSM switches to the *Derotate* state, where it computes the CORDIC algorithm. If after a certain time no receive signal is detected, the FSM switches back to the *Idle* state to wait for the start of the next receive packet.

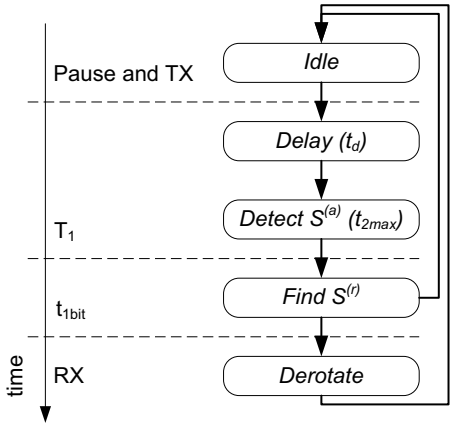

Figure 3.13: FSM states of the implementation of the channel estimation and derotation.

3.6.4 Synchronisation

As stated previously, the above proposed ML synchronisation method is not well suitable for real-time processing, as it requires accurate knowledge of the symbol period and averages over multiple symbols to estimate the sampling time instant, which causes a delay of the averaging length. Furthermore, the computation of the proposed frequency estimation scheme requires an optional preamble, which decreases the flexibility to experiment with all possible settings, and slightly decreases the data throughput. Therefore, a synchronisation method is developed, which does not rely on the optional preamble and which is feasible for real-time computation. It jointly estimates the sampling timing instant and the symbol frequency [89]. The timing recovery selects the time instant that maximises the correlation function within a *single* symbol period, in contrast to the averaging over K symbols in the method described above.

One of the major challenges in RFID reader receivers is, that the nominal symbol rate can vary from 40kHz to 640kHz. Liu et al. [91, 112] present an RFID reader receiver based on correlator banks to support this wide range of nominal frequencies and to synchronise, decode and estimate the frequency offset. They also show a realisation on an FPGA and present an elaborated implementation to reduce the overall hardware cost. However their implementation of 12 parallel correlation banks still exceeds the capacities of average FPGAs. My work however proposes an adaptive downsampling, that leaves exactly OSR samples for each pulse $S_n(t)$ of the receive signal x. This downsampled receive signal x_{OSR} is independent of the actual symbol rate, and is correlated with a reference symbol of fixed length OSR, which can be efficiently implemented. According to the downsampling ratio several receive signal samples are averaged to generate a sample of x_{OSR}.

The nominal symbol period, and thus the nominal oversampling ration OSR is known at the receiver, but subject to a variation ΔOSR. Hence, a window for deciding for

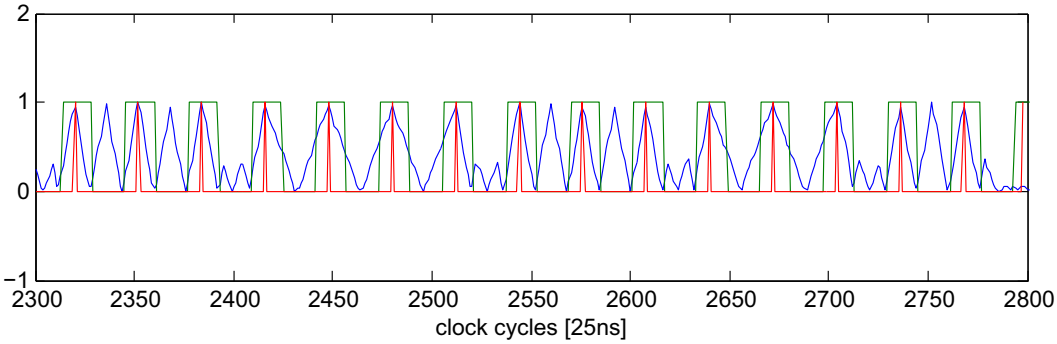

Figure 3.14: Synchronisation algorithm: absolute value of correlation function $|c[\nu]|$ in blue (Equation (3.25)), estimated sampling instants $\hat{\nu}_k$ in red (Equation (3.33)) and considered search intervals in green (Equation (3.34)), at E_b/N_0=30 dB.

symbol S_k^n is defined where the correlation function $c[\nu]$ of Equation (3.25) is considered for synchronisation.

$$\hat{\nu}_k = \arg\max_{\nu}\{|c[\nu]|\}, \tag{3.33}$$

with:

$$\nu \in \{\hat{\nu}_{k-1} + OSR - \Delta\, OSR \ldots \hat{\nu}_{k-1} + OSR + \Delta\, OSR\}. \tag{3.34}$$

Initial symbol timing estimation $\hat{\nu}_0$ is achieved by correlation with the preamble. At the maximum absolute value of the correlation function $|c[\nu]|$ the optimal sample point $\hat{\nu}_k$ is estimated. The estimated receive symbol is selected according to a positive or negative value of $c[\hat{\nu}_k]$, as given by Equation (3.24). Figure 3.14 shows the operation of the algorithm: the blue curve is the correlation function $c[\nu]$, the red curve the estimated symbol timing (Equation (3.33)) and finally the green curve shows the intervals in which the symbol timings are searched for (Equation (3.34)).

The method essentially realises the previously described technique of Equation (3.26), with the distinction that only a single period is considered and its interval is estimated on basis of the previous symbol instant estimation $\hat{\nu}_{k-1}$.

Additionally, the actual symbol rate deviates up to +/-22% from the nominal symbol rate. This deviation is estimated and tracked by the following scheme: We introduce three of the above described correlation units in parallel, but each has a slightly differently downsampled input signal x (see Figure 3.16). The oversampling ratio for the first correlator is selected to be $N-\epsilon$, the second to be exactly N, and finally the third to be $N+\epsilon$ samples per nominal symbol period. The three outputs of the parallel correlators are compared, and the one with the maximum output is assumed to be closest to the actual symbol rate. If the correlator with N samples per nominal symbol period does not give the highest output, the downsampling is updated for the next symbol period. Assume for example the correlator with $N-\epsilon$ samples per reference symbol period gave

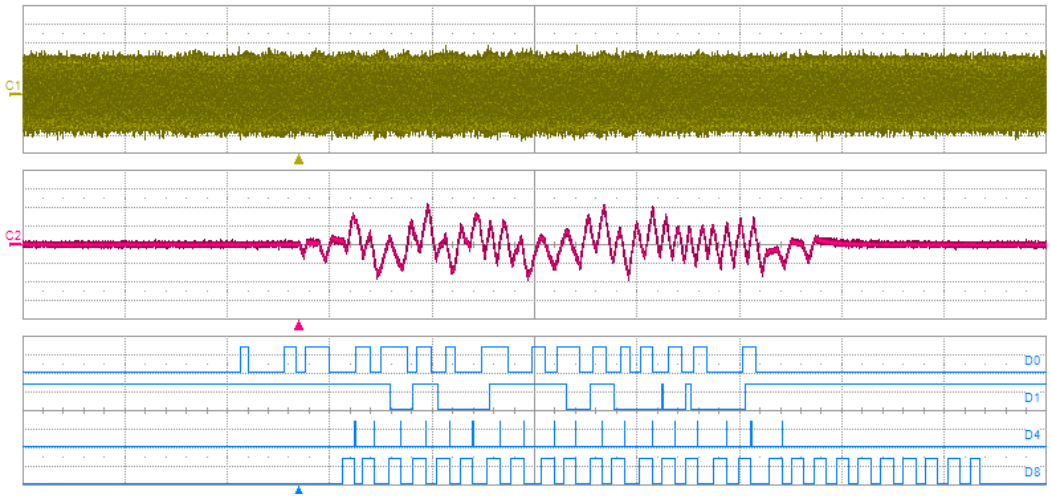

Figure 3.15: Oscilloscope screenshot of synchronisation structure: The top signal (yellow) is the receive signal $s(t)$. Due to the carrier leakage, the tag modulation signal is hardly visible. The signal below in pink depicts the correlation function $c(t)$. The digital lines output the FM0 encoded baseband signal, the decoded data signal, the recovered symbol frequency and finally the windows considered for searching the peaks of the correlation function $c(t)$ (intervals of ν, as given by Equation (3.34)).

the highest output, for the next period the oversample ratios are adjusted to N, $N - \epsilon$ and $N - 2\epsilon$ samples per symbol period. As concrete values for the implementation the following values have been selected: $N = 16$, $\Delta N = 4$, $\epsilon = 1$.

Figure 3.15 depicts an oscilloscope screenshot of the implemented synchronisation signals. The correlation function $c(t)$ is connected to the second DAC of the rapid prototyping board and monitored on the oscilloscope (second signal from the top in pink). Due to a delay and a high pass filter on the RF hardware of the output path, the signal is delayed and filtered. The top signal on the figure (in yellow) is the received signal at the intermediate frequency of 13.33 MHz. Due to the strong carrier leakage, the tag modulation signal is hardly surmised. The digital outputs below depict the recovered FM0 encoded baseband signal, the decoded data, the recovered symbol clock and finally the considered search intervals of the correlation function as defined in Equation (3.34).

Additional measurement results of the entire communication between reader and tag are presented in Appendix D. Moreover, debugging outputs after the single stages of the receiver are shown, which should give an impression about their operation.

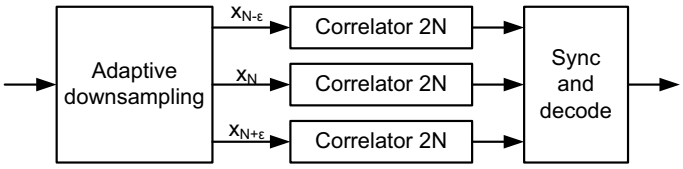

Figure 3.16: Structure of Synchronisation: three parallel correlation banks with slightly differently downsampled input signal to achieve correlation with with deviated reference symbols. The structure is similar to the early-late algorithm [93] which is applied for timing instant estimation, while the structure described here estimates the symbol frequency.

3.7 Performance Evaluation of Implementation

This section compares the performance of the above modifications of the channel estimation and the synchronisation mechanism in simulation, and the finally implemented architecture in measurement.

Figure 3.17 shows the simulation and measurement results. Again, the 16 bit random number packet corrupted by AWGN was used for the BER computation. The blue curve (labeled as "ML sequence decoder") again shows the ML sequence decoder performance with full channel and synchronisation information. The green curve (labeled as "RT Channel Est.") shows the losses due to the channel estimation according to Equation (3.31), which are higher, compared to the previous scheme, due to 1) an averaging over half a symbol period instead of a full period, and 2) the missing synchronisation information during the first symbol period. The red curve (with the label "RT Timing Est.") shows the losses of the real-time (RT) timing recovery according to Equation (3.33). Finally, the light-blue curve (labeled as "RT Channel and Timing Est.") depicts the losses of both, the channel estimation and the synchronisation. The results demonstrate that synchronisation is the most crucial task in RFID reader receivers, and improper synchronisation leads to the highest performance losses.

In order to evaluate the performance of the implemented receiver structure, the bit error ratio of the system was measured by the setup shown in Figure 3.18. At each E_b/N_0 point 10^5 packets are measured to calculate the bit error ratio. The measurement requires the estimation of the E_b and N_0 at the receiver, which is performed as described in Section 3.6.3. An average over all 10^5 packets, corresponding to one measurement point of both, E_b and N_0 is processed, before E_b/N_0 is computed. Different E_b/N_0 scenarios have been realised by adding additional noise before the ADC of the board by means of an analogue noise generator.

The transmitter generates the Query command, but also emulates the RN16 packet as a tag response (Figure 3.18), due to the following two reasons: First, the receiver requires knowledge about the receive data to process the BER. Second, the energy per bit E_b at the receiver is approximately constant, and does not show any variations, as this may

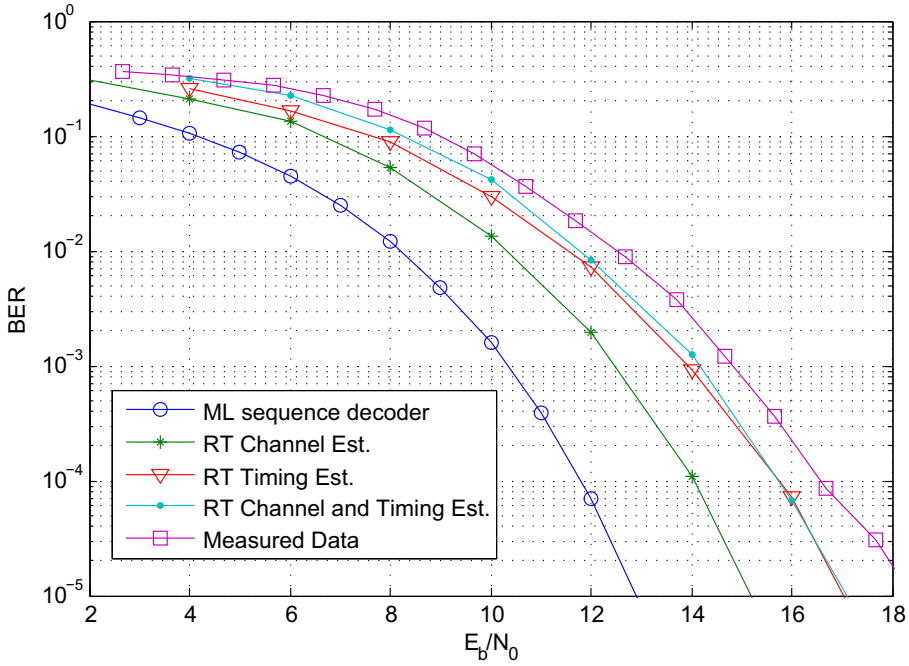

Figure 3.17: Simulated and measured bit error ratio: "ML sequence decoder" is the theoretical performance of the ML sequence decoder. "RT Channel Est." is the performance of ML sequence decoder with Real-Time (RT) channel estimation as presented in Section 3.6.3. "RT Timing Est." is the performance of the ML sequence decoder with RT synchronisation. The curve with the label "RT Channel and Timing Est." includes both, the RT timing and Channel estimation. Finally, "Measured Data" is the measured performance of the implementation.

occurs with real tags. The measured performance of the receiver is depicted in purple in Figure 3.17 (with the label "Measured Data"). Compared to the simulation result with the implemented channel estimation and synchronisation structure, the losses are reasonable.

The measured performance of the implemented receiver in a communication with a commercially available RFID tag is shown in Section 2.3 by means of a measured PER.

3.8 Discussion and Conclusion

RFID systems feature specific characteristics, affecting the design and implementation of reader receiver architectures. These characteristics are identified as 1) the energy supplying carrier leakage, 2) the presence of only a single carrier frequency originating from a single source, and 3) the loose limits on symbol timing precision in the uplink channel. While the advantage of a single oscillator usage permits a downconversion

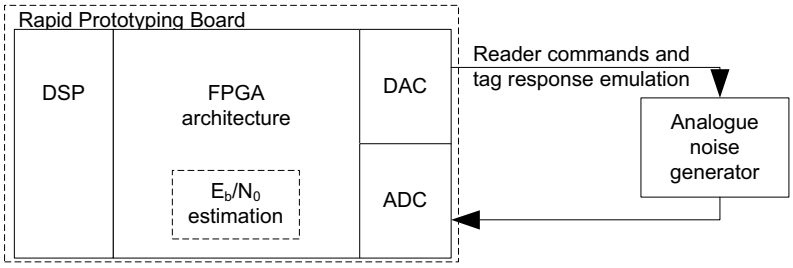

Figure 3.18: Setup for measuring the BER.

without a carrier frequency offset compensation, the presence of the carrier leakage and the wide tolerances in symbol timings on RFID tags severely complicate the design of RFID readers. At least in our static setup with 14 bit ADCs and high performance frontends [106, 107] the carrier leakage could be estimated sufficiently accurately and digitally subtracted from the receive signal, to minimise its impact (compare with the green curve in Figure 3.9). Additionally, the carrier leakage should be minimised before sampling, for example by an active carrier cancellation. In this approach, a fraction of the transmit carrier is modified in amplitude and phase to subtract it from the received carrier leakage [108, 124]. Synchronisation however remains a very critical issue: if accurate knowledge about the symbol frequency exists, an ML estimation taking into account several symbols provides a reasonably well performance (black curve in Figure 3.9). However this knowledge about the symbol frequency is not given, and its potential deviation of $\pm 22\%$ is much stronger than in other wireless communication systems, which prevents to achieve the well performance of state-of-the-art ML and MMSE synchronisation methods. Additionally, rectangular pulses lead to a triangular correlation function, which increases the impact of slight timing offsets. In other wireless communication systems, different pulse shapes, such as the raised cosine are used. With such pulse shapes, a timing offset has a less severe impact, as, these pulses are relatively flat in the vicinity of the ideal sampling instant, compared to the triangular correlation function. Additionally the encoding schemes result in half symbol period peaks, complicating the synchronisation. Furthermore, the short preamble and the relatively short packets in RFID (for instance 16 bits only) demand a fast adaptation of the timing recovery within just a view bits. Eventually, also the channel estimation is affected by the missing synchronisation. May the performance of the synchronisation algorithm can be further improved by applying MMSE techniques with variable stepsizes, that is, a fast adaptation at the beginning of the packet to coarse frequency estimation and after a view receive bits a smaller stepsize for a inertial and more accurate adaptation to the optimal timing instant. Similarly, the search intervals of the proposed ML technique could be tightened with increasing receive time, which is expected to allow for a more accurate adaption. However, due to the increased complexity this approach was not followed.

A flaw of the proposed model for signal constellations and the derivated receivers is

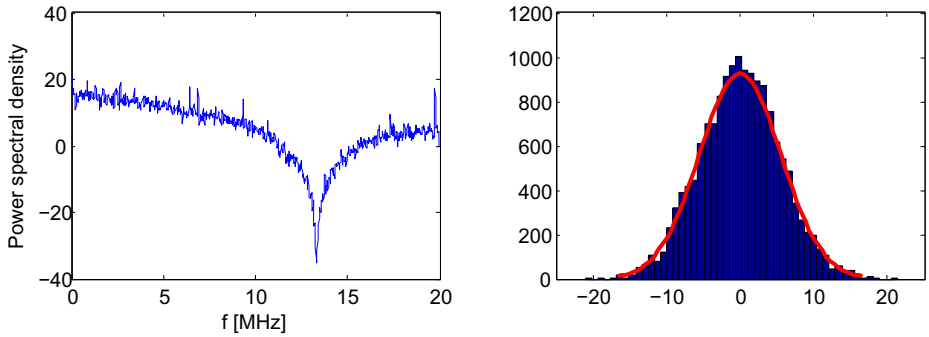

Figure 3.19: Power Spectral Density (PSD) and fit of Gaussian distribution to histogram of measured received samples of carrier leakage with subtracted mean. The sample size is 16384, the PSD is plotted by the Welch method [139] with 16 windows, and the y-axis of the plot has a logarithmic scale.

the assumption of additive white Gaussian noise at the receiver. In RFID, the noise power spectral density may be dominated by the phase noise of the oscillator, as in the frequency domain the tag modulation signal is close to the carrier leakage. The convenient assumption of AWGN however allows for simpler analytic tractability. Furthermore, Figure 3.19 provides an analysis of the noise distribution at the receiver, for 16384 measured samples of an unmodulated receive signal with subtracted carrier leakage (that is the noise signal, compare with Equation (3.8)): The left plot is the estimated power spectral density applying the Welch method [139] to the sampled noise signal, after the downconversion. As the downconversion also requires a low pass filtering to suppress the mirrored frequency component at 13.33 MHz (compare with Section 3.6.1), the shape of the filter can be clearly identified. In the frequency range of interest, that is approximately from zero to two MHz, the noise spectrum is flat, such that the assumption of white noise is reasonable. The right plot in Figure 3.19 shows a fit of the histogram of the receive samples to the Gaussian distribution. This indicates, that the assumption of AWGN at least is valid for our experimental setup with high performance frontends and laboratory equipment serving as oscillators, however might be different with lower performance equipment.

In general, the proposed receiver structures are relatively complex due to the channel estimation and synchronisation. I however tried to achieve a resource optimised implementation on the hardware. During the development of the architecture, it took me quite long to understand the importance of synchronisation in the context of RFID baseband processing. The proposed architecture is tailored to match the EPCglobal standards, for example it utilises certain link timings in the channel estimation and supports the data rates defined there. An adaption to other standards however is expected to be simple, as these parameters are configurable via FPGA registers.

Implementation specific aspects such as the completion of real-time constraints are discussed in this chapter, and a digital RFID reader architecture is proposed. The

performance loss of the real-time channel estimation and synchronisation algorithm is illuminated, and the measured BER of the implementation is shown.

4. RECEIVERS FOR DUAL ANTENNA RFID READERS

UHF RFID systems operate in an environment exposed to fading. The previous chapter showed the development of a single antenna receiver communicating with a single tag, which is extended to a dual receive antenna system in this chapter. While state-of-the-art RFID readers utilise multiple receive antennas with antenna multiplexing in order to deal with the multipath propagation environment, this chapter proposes Maximal Ratio Combining (MRC) at RFID reader receivers. In order to support experimental evaluation of maximal ratio combining, the rapid prototyping environment is extended to a dual receive antenna setup. The previously developed model of receive signal constellations (Chapter 3) is expanded to multiple receive antennas. With that model, I design a receiver estimating the channel coefficients and realising maximal ratio combining of the received signals, thus achieving the optimum combination of receive signals in terms of SNR maximisation. In an environment with low fading, the *same* receiver also estimates the Direction Of Arrival (DOA). Underlying assumptions on the receive signals at the RFID reader for the design of the receiver are cross-verified with measurements. Finally, the receiver is implemented on an FPGA and its performance is compared with random antenna selection receivers by measurements.

In passive UHF RFID, the propagation channel is strongly impaired by fading. Thorough theoretical analysis of the propagation channel from the reader transmitter to the tag backscatter and back to the reader receiver has been performed by Nikitin et al. for a single antenna reader receiver [125]. They also verified their models by measurements. A general model for both, a multiple antenna reader and a multiple antenna tag is proposed by Ingram et al. [97]. Griffin et al. [34] identify the theoretical performance increase of multiple antenna readers and multiple antenna tags by calculations and simulation, especially focusing on multiple antenna tags. Additionally, Nikitin et al. [96] present experimental results on read range increase and orientation insensitivity of RFID tags with multiple RF ports. Wang et al. [140] sketch a reader receiver performing maximal ratio combining, however do not present any realisation. The novel contributions of this chapter are the development, implementation and experimental evaluation of maximal ratio combining at reader receivers with two antennas.

In order to combat multipath propagation, state-of-the-art RFID readers utilise several

receive antennas with antenna switching (or equivalently named Random Antenna Selection (RAS)[1]), such as for example the RFID reader by Feig Electronics [24]. They simply switch between the receive antennas alternately.

To my knowledge, in this thesis the first design of a digital RFID reader receiver performing maximal ratio combining is presented. It combines the signals of two antennas in an optimal way, with respect to the total signal to noise ratio (SNR) output. The advantage in contrast to antenna multiplexing is obvious: First, antenna multiplexing needs to multiplex all N_r receive antennas to identify the antenna with the highest SNR. Second, MRC always results in a stronger SNR than each of the single antenna receive paths. The tradeoff is the duplication of the reader receive frontend and the increased signal processing complexity. The receiver has been implemented for a dual receive antenna reader, however it can be easily extended to multiple receive antennas.

While the maximal ratio combining receiver shows a diversity gain in a fading environment, the same receiver can also be applied in low fading environments to estimate the direction of arrival of RFID tags [98]. While work by Kim et al. [141] estimate the direction of arrival by tracking the receive signal strength of two directional antennas depending on their orientation, the phase difference at distinct array elements is considered for direction of arrival estimation in this thesis. Additionally, several authors, for instance [73, 101] propose to use multiple readers and reader-to-tag distance estimation to localise an RFID tag. Other authors [142, 143] propose to apply smart antennas to estimate the DOA and provide a theoretical analysis of the performance, while this thesis also shows experimental results. Salonen et al. [144] show a phased array realisation for blindly scanning an area with a beam. During the writing of this thesis, two very recent publications on DOA estimation on RFID readers have been published at the IEEE International Conference on RFID in spring 2010: Nikitin et al. [99] compare different techniques of DOA estimation by utilising a phase difference. They propose to exploit a phase difference of a) multiple consecutive measurements of a moving tag (time domain), b) multiple consecutive measurements of a static tag with different carrier frequencies (frequency domain), and c) multiple receive antennas (spatial domain). While the spatial domain approach in their paper is of conceptual nature, I also show experimental results on this topic in this chapter. Furthermore, Hekimian et al. [100] propose a DOA estimation in active RFID systems by combining two RFID reader modules. Both modules are synchronised by applying an external clock. As they use active RFID, they also need to compensate the carrier offset after downconversion. Their paper shows excellent experimental results. Ranging in passive RFID by means of Frequency Modulated Continuous Wave (FMCW) and multiple frequency continuous wave radars, additionally has been demonstrated in [145, 146], respectively.

[1] Throughout this chapter I use the terms antenna switching and random antenna selection as synonyms.

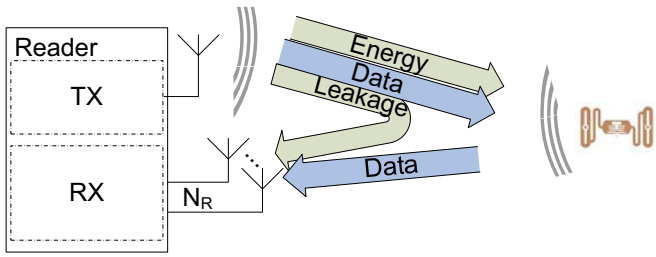

Figure 4.1: Communication between an RFID reader with multiple RX antennas and an RFID tag.

4.1 Signal Model

Figure 4.1 shows the basic communication between a tag and a reader receiver with N_R antennas. While the forward channel and tag backscatter modulation remains equal to the single receive antenna case described by Equation (3.5), the tag signal adds with the carrier leakage at the receive antenna j:

$$\begin{aligned} s_j^{pb}(t) = \sqrt{2}|h_j^b|\sqrt{|\Delta\sigma|}|h^f|a(t)\sin(\omega_c t + \varphi^f + \varphi_j^b + \varphi^{\Delta\sigma}) \\ +\sqrt{2}|L_j|\sin(\omega_c t + \varphi_j^{leak}) + n_j^{pb}(t). \end{aligned} \tag{4.1}$$

The terms $|h_j^b|$ and φ_j^b denote the backward channel attenuations and phase shifts from the tag to the j'th reader receive antenna, while $|L_j|$ and φ_j^{leak} are the magnitude and phase shift of the carrier leakage at the j'th receive antenna. Again, the power of the transmitted continuous carrier signal is normalised to one.

Again, a downconversion without a frequency offset compensation is feasible at each antenna, as only a single frequency source (the oscillator in the transmitter of the reader) exists in the system. The complex-valued baseband signal at antenna j hence is:

$$s_j(t) = h_j^b\sqrt{\Delta\sigma}h^f a(t) + L_j + n_j(t), \tag{4.2}$$

where $h_j^b = |h_j^b|e^{j\varphi_j^b}$ is the complex-valued backward channel coefficient, $L_j = |L_j|e^{j\varphi_j^{leak}}$ denotes the static and complex-valued carrier leakage, and $n_j(t)$ is the complex-valued circularly symmetric white Gaussian noise with noise power spectral density N_0. Equivalently, we can reformulate Equation (3.7) to:

$$s_j(t) = h_j a(t) + L_j + n_j(t), \tag{4.3}$$

where $h_j = h^f\sqrt{\Delta\sigma}h_j^b$ is the channel coefficient of the equivalent dyadic channel from the transmitter of the reader to the tag and back to the j'th receive antenna of the reader. Again, also the modulation behaviour of the tag is modeled by the channel coefficient h (term $\sqrt{\Delta\sigma}$). By stacking the receive signals $s_j(t)$, channel coefficients h_j, carrier

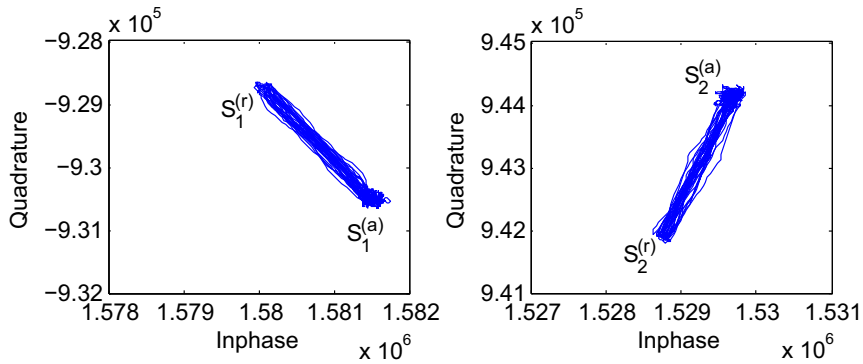

(a) Antenna 1 (b) Antenna 2

Figure 4.2: Measured tag response signals in baseband: inphase and quadrature constellations on both antennas.

leakage L_j and noise components $n_j(t)$ of all N_R receive antennas into the $N_R \times 1$ vectors $\mathbf{s}(t)$, $\mathbf{h}$, $\mathbf{l}$ and $\mathbf{n}(t)$, respectively, Equation (4.3) is equivalently reformulated to:

$$\mathbf{s}(t) = \mathbf{h}a(t) + \mathbf{l} + \mathbf{n}(t). \tag{4.4}$$

As in the single antenna receiver, a tag absorb state $S_j^{(a)}$ and a tag reflect state $S_j^{(r)}$ are identified in the I/Q baseband plane of each receive antenna j. While the tag absorb state $S_j^{(a)} = L_j$ corresponds to the carrier leakage at antenna j, the reflect state $S_j^{(r)} = L_j + h_j$ additionally includes the backscatter modulation. Again, the location of the states in the I/Q baseband plane is arbitrary to the reader receiver, and depends on the extent of the carrier leakage L_j as well as on the channel coefficients h_j (compare with Section 3.1 and Figure 3.3). The magnitude and phase of L_j and h_j depend on the spatial setup of reader and tag antennas as well as of the environmental scattering, and on the transmitter to receiver decoupling scheme. The situation on both antennas can be completely diverse, as shown in the example of measured data in Figure 4.2 for phase and magnitude of both, the carrier leakage and the tag modulation.

4.2 Dual Receive Antenna Rapid Prototyping System

In order to verify the above model by measurements, the rapid prototyping system is extended to a dual receive antenna RFID reader platform [107, 147]. Each receive antenna is interfaced with the digital baseband hardware by an ADC, again at the intermediate frequency of 13.33 MHz. Both ADCs sample synchronously with a sampling rate of 40 MHz. In a first step, samples captured after the two independent ADCs on the rapid prototyping system during a measurement have been imported into Matlab

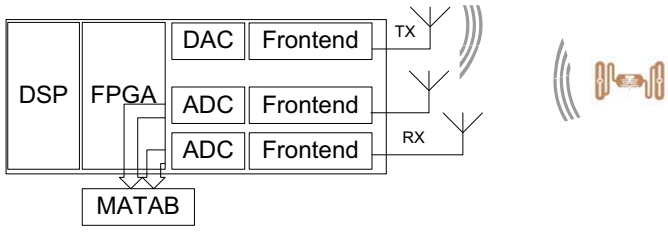

Figure 4.3: Measurement setup: capture signals at two RX antennas.

(see Figure 4.3).

Figure 4.2 shows the measured receive sequences after offline I/Q demodulation and integration, in the baseband of the reader receiver for each antenna. One can clearly determine the two receive states $S_j^{(a)}$ and $S_j^{(r)}$ in both I/Q diagrams. As with the single receive antenna system, an integration over a half symbol period is performed (compare with Section 3.6). Due to that integration and the triangular shape of the signals, the receive samples move between the absorb and reflect state. The offset from the origin results from the carrier leakage L_j. As expected by the above model, both states $S_j^{(a)}$ and $S_j^{(r)}$ on both antennas are at an arbitrary location in each I/Q plane for the reader receiver, depending on L_j and h_j.

In the following an MRC receiver is developed, combining the signals of the N_R receive antennas. The measurement data is applied as example data to demonstrate the various steps of the receiver.

4.3 Maximal Ratio Combining Receivers

In terms of maximum SNR, the optimal combination method of multiple independent copies of the receive signal is maximal ratio combining:

$$\hat{a}(t) = \Re\left\{\frac{1}{c}\sum_{j=1}^{N_r}(s_j(t) - L_j)\ h_j^*/\sigma_j^2\right\}. \tag{4.5}$$

Here, σ_j denotes the noise power at antenna j, h_j^* is the complex conjugate of h_j and $c = \sum_j |h_j|^2/\sigma_j^2$ is a normalisation factor. Equation (3.12) essentially is the single antenna case of Equation (4.5). As maximal ratio combining requires the knowledge of the channel coefficients h_j and the noise power σ_j^2, channel and noise power estimation is required. The extension of the single antenna receiver to a multiple antenna MRC receiver solely affects the channel estimation and combination stage, while the synchronisation on the recovered modulation signal $a(t)$ is achieved equally as with the single antenna receiver.

The channel coefficients h_j are estimated separately for each antenna j and are concluded

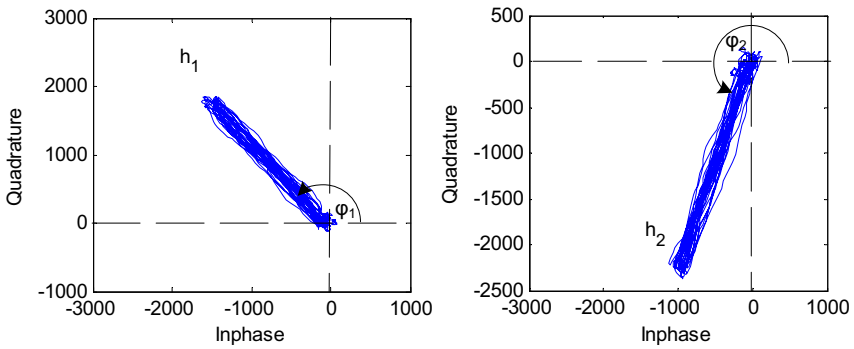

(a) Antenna 1 (b) Antenna 2

Figure 4.4: Tag response in baseband with removed carrier leakage: inphase and quadrature constellations on both RX branches

from the tag states according to Equation (3.20). The estimation at each antenna is equal to the single antenna case according to Equation (3.18) and Equation (3.31).

As soon as both states on all antennas are estimated, the carrier leakage, which does not carry any information is subtracted according to Equation (4.5). This basically shifts the I/Q constellation of both antennas to the origin, as depicted in Figure 4.4. The shifted tag reflect state is now comprised of the channel coefficient h_j only. While the forward channel coefficient h^f and the normalised differential radar cross section $\Delta\sigma$ are equal for both channel coefficients h_j, only the backward channel h_j^b is exposed to distinct fading realisations. Although diversity is only exploited in the backward channel, MRC nevertheless guarantees the maximum SNR at the combined output. The terms h^f and $\Delta\sigma$ may be considered as an equal scaling of the channel coefficient on all antennas.

It is important to note that the SNR on the various receive antennas may result from different receive signal powers or different noise levels in the individual receiver chains. A different receive signal strength is caused by different fading realisations on the various antennas. Distinct noise power levels can also result from different transmitter / receiver decoupling schemes: If all receive branches are decoupled from the transmitter by separated antennas, equal noise power is expected, and thus σ_j^2 can be omitted in Equation (4.5). If however the transmitter and one receive branch share one single antenna and the decoupling is achieved via a circulator or directional coupler, the noise power in this receive branch may be significantly higher, as noise generated by the transmit power amplifier leaks into the receiver via the circulator [123].

After the estimation of the channel coefficients the various receive paths are combined according to Equation (4.5). The complex multiplications in Equation (4.5) are split into phase shifts and multiplications of magnitudes. The phase shift rotates the constellation at each antenna to 0 degrees. Figure 4.5 displays the rotated constellations of the

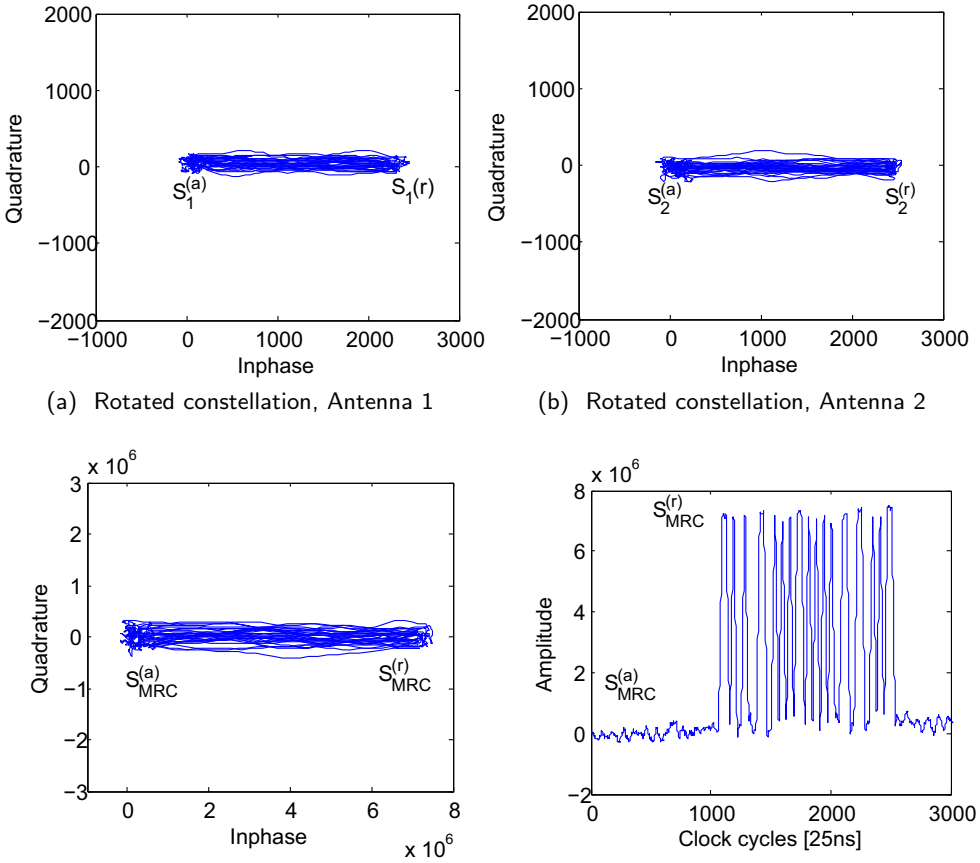

(a) Rotated constellation, Antenna 1

(b) Rotated constellation, Antenna 2

(c) Combined constellation, I/Q

(d) Combined constellation, inphase component

Figure 4.5: Tag response in baseband: maximal ratio combining.

measured data for both antennas. Figure 4.5c shows the I/Q constellation diagram of the combined signal (without normalisation) according to Equation (4.5). Finally, Figure 4.5d plots the MRC combined signal in the time domain. After the maximal ratio combining, the combined signal is synchronised and decoded as with the single antenna receivers. The estimated E_b/N_0 of the example data are 31.2dB and 32.4dB for Antenna 1 and Antenna 2, respectively, while the E_b/N_0 for the combined signal is 33.8dB.

4.3.1 Implementation

The presented algorithm achieves the following: It estimates the absorb and the reflect states on each antenna individually, and concludes the channel coefficient. The complex multiplication in Equation (4.5) is realised by a phase shift and a multiplication of magnitudes, while the division by the noise term is avoided by expanding the fraction

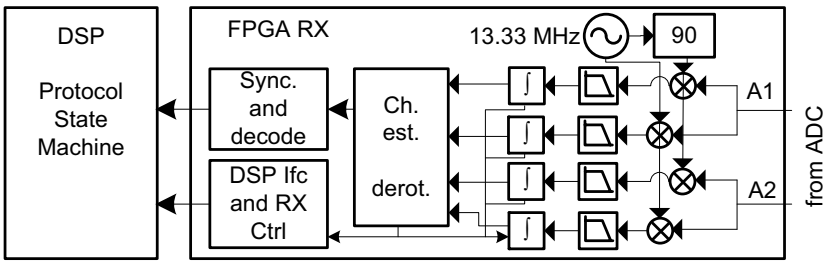

Figure 4.6: Block diagram of the receiver.

and thus turning it into a multiplication. As all the steps are processed sequentially (estimation of absorb state, estimation of reflect state, rotation to inphase component, multiplication of magnitudes and summation), the algorithm is suitable for real-time processing in a pipelined design. It has been implemented on the FPGA of the established RFID prototyping system.

A block diagram of the implemented receiver is shown in Figure 4.6: The signals of both receive antennas are sampled at ADCs, I/Q downconverted and integrated over a half symbol period, as in the single antenna receiver. The channel estimation and maximal ratio combining are implemented as a finite state machine (FSM) in the subsequent block. The output signal is synchronised and decoded, before the receive bits are forwarded to the DSP for protocol processing. Registers and interrupts are utilised to exchange control information between DSP and FPGA. The estimation of the phase of the constellation and the rotation of the constellation on the hardware has been realised by a CORDIC algorithm [138] (compare with Section 3.6).

4.4 Direction of Arrival Estimation

Reviewing Equation (4.3), the subtraction of the estimated carrier leakage from the receive signal at each antenna $s_j(t) - L_j = h_j a(t) + n_j(t)$, directly shows the channel coefficient modulated by the data, as depicted in Figure 4.4. In contrast to the carrier leakage, only the receive signal from the tag carries information about its location. The angles φ_j of the constellation in the I/Q plane are composed of the forward channel phase shift φ^f, the phase shift due to the tag modulation $\varphi^{\Delta\sigma}$ and the backward channel phase shift φ_j^b:

$$\varphi_j \triangleq \varphi^f + \varphi^{\Delta\sigma} + \varphi_j^b. \tag{4.6}$$

As φ^f and $\varphi^{\Delta\sigma}$ affect both receive antenna constellations equally, a phase difference $\Delta\varphi = \varphi_j - \varphi_{j-1}$ in the constellation of the receive paths j and $j-1$ ($j \geq 2$) solely results from a distinct phase shift $\varphi_j^b - \varphi_{j-1}^b$ in the backward channels h_j^b and h_{j-1}^b. Assuming Line Of Sight (LOS) communication from the tag to the reader, a linear array of equidistant elements with spacing d and the tag-to-reader distance D much larger

than the array size $D \gg (N-1)d$ (Figure 4.7), the phase difference between two neighbouring elements $\Delta\varphi$ is:

$$\Delta\varphi = kd\cos(\phi). \tag{4.7}$$

Here, $k = 2\pi/\lambda$ is the wave number, λ denotes the wavelength and ϕ is the Direction Of Arrival (DOA). Based on the estimation of the channel coefficients h_j, the DOA is estimated by correlating the channel coefficients with the $N_R \times 1$ steering vector $\mathbf{t}(\phi)$, whose i'th element is $e^{j(i-1)kd\cos(\phi)}$ [148]:

$$\begin{aligned} r(\phi) &= \mathbf{h}^H \mathbf{t}(\phi) \\ &= \sum_{i=1}^{N_R} h_i^* e^{jkd\cos(\phi)(i-1)} \\ &= \sum_{i=1}^{N_R} h_i^* e^{j\psi(i-1)} \\ \hat{\phi} &= \arg\max_{\phi} |r(\phi)|. \end{aligned} \tag{4.8}$$

The sum here essentially is the Discrete Time Fourier Transform (DTFT) of the channel coefficients h_j, with $\psi = kd\cos(\phi)$ denoting the spatial frequency. Consider h_j as the excitation of antenna j, then the DTFT is the array factor. Its maximum serves as the estimate for the DOA ϕ. Due to the above assumptions of LOS and $D \gg (N-1)d$ the path loss on all receive antennas is approximately equal $|h_i| \approx |h_j|$, thus distinct channel coefficients only differ in a phase shift.

On our rapid prototyping platform with only $N_R = 2$ receive antennas and the assumption of $|h_1| \approx |h_2|$, Equation (4.8) reduces to:

$$\hat{\phi} = \arg\max_{\phi} \left| e^{-j\varphi_1} + e^{-j\varphi_2} e^{jkd\cos(\phi)} \right|, \tag{4.9}$$

$$-\varphi_1 = -\varphi_2 + kd\cos(\hat{\phi}), \tag{4.10}$$

$$\hat{\phi} = \arccos\left(\frac{\Delta\varphi}{kd}\right), \tag{4.11}$$

where Equation (4.10) results from Equation (4.9) with the argument, that for maximum magnitude the phases of both terms must be equal (Triangle Inequality).

The argument of the $\arccos(\cdot)$ term in Equation (4.11) must be in the range of -1 to 1, that is $\frac{\Delta\varphi}{kd} \in [-1,\, 1]$. If $d < \lambda/2$, only a single solution is possible. If $d > \lambda/2$ however, multiple solutions are possible, due to the 2π-periodicity of $\Delta\varphi$, for instance two possible solutions for $\lambda/2 < d < \lambda$. These solutions occur due to so-called grating lobes in the beam pattern [148,149] for arrays with element spacing $d > \lambda/2$. However, there is only a single solution within the span $\phi \in [\arccos(\frac{\pi}{kd}),\, \arccos(\frac{-\pi}{kd})]$ for $\lambda/2 < d < \lambda$.

On the rapid prototyping board, the angles φ_1 and φ_2 are determined by the clockwise or

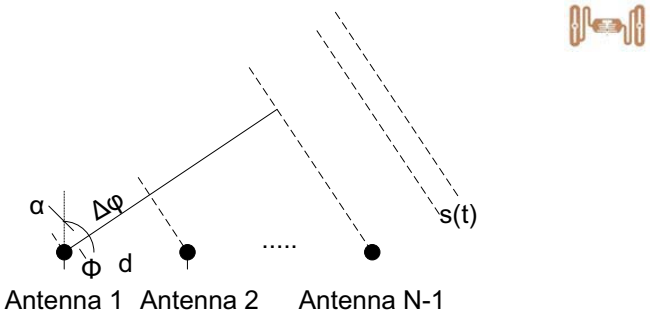

Figure 4.7: Localisation of RFID tag with multiple antennas.

counterclockwise rotation of the CORDIC in each stage, while the rest of Equation (4.11) is processed offline.

4.5 Experimental Evaluation

The performance of the implemented MRC receiver is compared to the performance of a receiver with random antenna selection (or antenna switching) by means of measurements of the receive E_b/N_0 and PER [95]. Additionally, the feasibility of DOA estimation in a scenario with low fading is demonstrated [98].

4.5.1 Measurement Setup

Figure 4.8 depicts the spatial measurement setup. In order to actualise various fading realisations, the tag is moved to distinct spatial locations, by means of a motor driven nylon cord. At each location, the EPC code of the tag is read out by the procedure described in Section 2.3. The readout is repeated for 5×10^4 iterations, in which the receive antenna configuration is switched alternately between single and dual antenna mode. Thus, 2.5×10^4 readouts are performed applying MRC and 1.25×10^4 readouts are performed on each single antenna, adding up to 2.5×10^4 readouts with random antenna selection. An average of E_b, N_0, φ_i as well as the successful readouts for each antenna configuration is recorded at each position.

After the readouts at a certain location are completed, the procedure is repeated at the next position. The actualised positions for the measurements are separated 2 cm in the x-direction and 0.5 m in y-direction. The 2 cm steps in x-direction also allow for a spatial capturing in deep fades. The TX and RX antennas are positioned to minimise the carrier leakage in the receive paths. Furthermore, the dimensions of the measurement room allow for a maximum reader-to-tag distance of 3.4 m, as depicted in Figure 4.8.

All antennas are commercially available RFID patch antennas. The employed transmit antenna has a gain of 9 dBi while the two receive antennas feature a gain of 8 dBi.

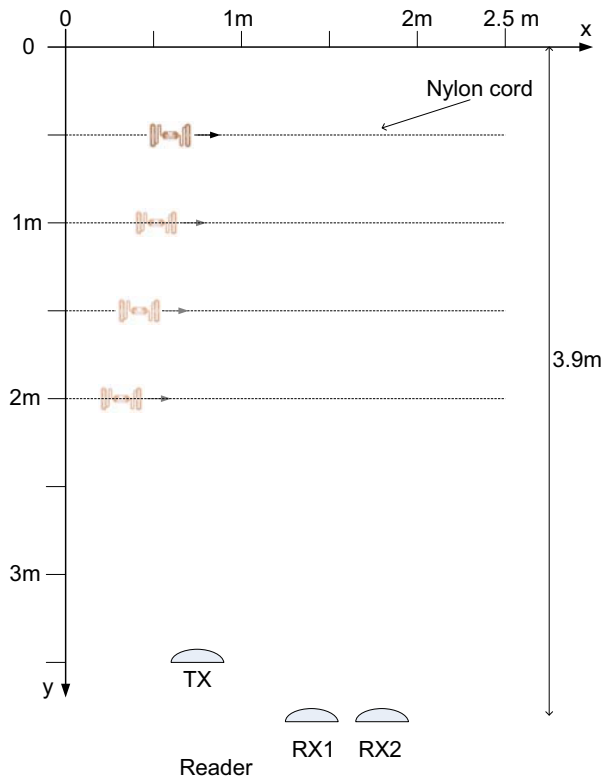

Figure 4.8: Measurement setup: the tag is moved on the nylon cord to positions with 0.5 m y-spacing and 0.02 m x-spacing. At each location, 2.5×10^4 measures with MRC and 2.5×10^4 measures with random antenna selection are performed. The antenna positions are: TX=(0.8m/3.5m), RX1=(1.4m/3.9m), RX2=(1.7m/3.9m).

The measurement is conducted in a measurement room with almost no fading (quasi-anechoic room) for evaluation of the DOA estimation capabilities of the receiver. For the performance comparison of the MRC receiver with random antenna selection, fading is generated artificially by placing metallic reflectors into the measurement room. Figure 4.9 shows a photograph of the scenario with reflectors. The reflectors remain static during the measurement to circumvent a fading evolution on time at a certain location. Hence, the only movement during the measurement is the tag itself, which is mounted on the electrically invisible nylon cord to avoid an influence on the fading due to the fixture of the tag. Additionally, only the antennas of the RFID reader are placed inside the measurement room, while the frontends and digital baseband hardware reside outside. The transmit power is set to 25.5 dBm, the required measurement time to conduct the $x/\Delta x \times y/\Delta y \times$ iterations $= 2500/20 \times 4 \times 5 \times 10^4 = 25 \times 10^6$ readouts is approximately 125 hours.

The measurement is controlled by Matlab, which activates the rapid prototyping board

Figure 4.9: Measurement setup with TX (left) and RX (right) antennas. The tag is moved on the motor driven nylon cord through the measurement room. The fading in the room is generated artificially by placing one dominant ($\approx 2.5\,\mathrm{m}^2$) reflector in back left corner (position x=0 m, y=0 m) and several smaller reflectors in the measurement scenario.

via the Local Area Network (LAN) to read out the tag at a certain position, stores the results after completion, and triggers the tag movement to the neighbouring position, before the next readout is initiated. Throughout the measurement, a single tag is used [150].

4.5.2 Results: Maximal Ratio Combining versus Random Antenna Selection

Figure 4.10 shows the measurement results of the random antenna selection and maximum ratio combining comparison. The x and y direction correspond to the positions as depicted in Figure 4.8. The surface in Figure 4.10c shows the measured average SNR at one antenna $\Gamma = E\{\gamma_j\}$, where $\gamma_j = 1/2|h_j|^2/N_0$ denotes the instantaneous E_b/N_0 at antenna[2] j. The contour plot below all figures also shows the average SNR Γ distribution at a single antenna at the various measurement positions. Figure 4.10a and Figure 4.10b depict the measured PER for random antenna selection and maximal ratio combining, respectively. There are certain locations, where the tag does not respond at all, like in the back left and front right corner. These positions are also indicated by a missing Γ value in the contour plot (blank areas, for example at positions $x < 0.2\,\mathrm{m}$, y=2 m). Obviously, the tag is not supplied with sufficient power, meaning that the

[2] The factor $1/2$ in γ_j results from the on-off keying modulation: $E\{S_n(t)\}$=1/2 (compare with Section 3.1).

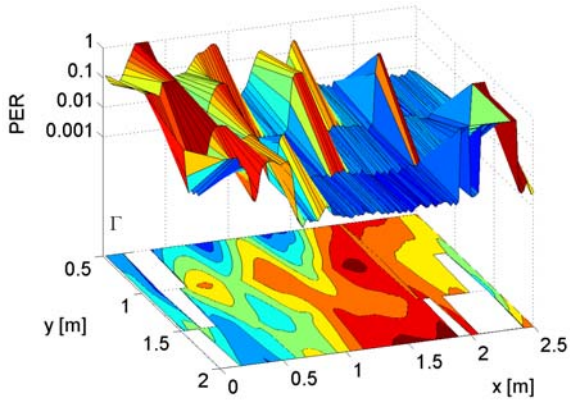

(a) PER with random antenna selection

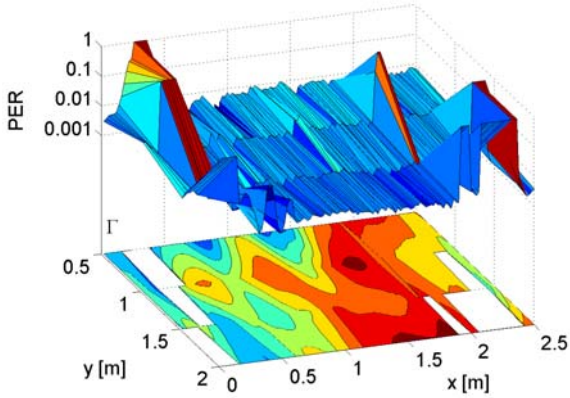

(b) PER with MRC

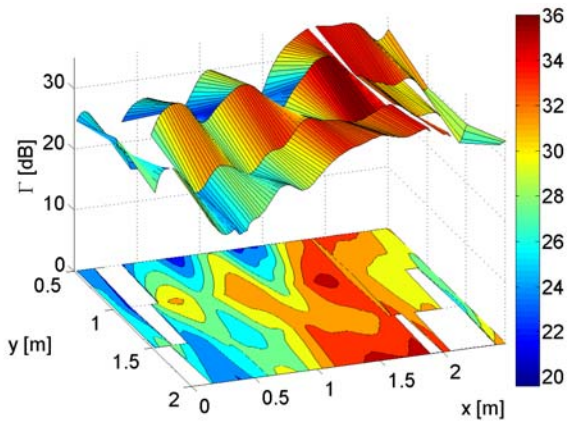

(c) Γ

Figure 4.10: Measurement results: (a) PER with random antenna selection, (b) PER with MRC, (c) Γ: average SNR at one antenna. The contour plot at the bottom of each graph shows the measured Γ at each location.

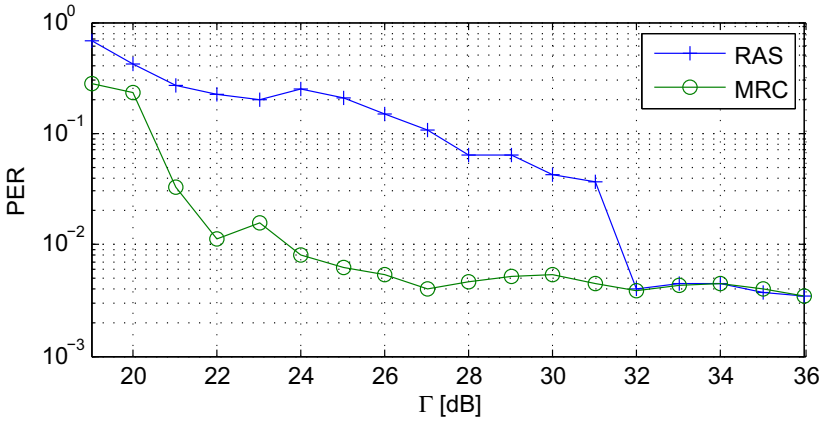

Figure 4.11: PER comparison of MRC and RAS.

reader-to-tag link fades or the position is out of the TX antenna illumination. At these positions, no signal from the tag is observed on the oscilloscope either. Additionally, at the isolated position x=1.76 m, y=1 m, no signal was received, although its surrounding positions show a distribution of a high Γ. This is due to shading at this single position by a metallic pole which was placed as an artificial reflector.

We observe that at positions in front of the RX antennas (x=1.4 m and x=1.7 m) Γ is higher than at positions hardly illuminated by the receive antennas (for example at the left side). Although tags at positions in front of the TX antenna (x=0.8 m) are expected to be perfectly supplied with energy, Γ is higher at regions where the tags are still sufficiently supplied with energy, but are better illuminated by the RX antennas. This matches with the result obtained in Section 2.3, that a higher power supply does not lead to a better receive SNR, due to a decrease of $\sqrt{|\Delta\sigma|}$ with increasing P_{TX} [119, 120]. In regions with a small value of Γ ($x < 1$ m), the maximal ratio combining shows a significantly better performance than the random antenna selection. Consider for instance the case, where one return path suffers from high fading, while the other receive path experiences only little fading. Then, with random antenna selection, the high fading path will show a high number of errors, which dominate the average PER performance. The MRC receiver however always generates a PER smaller than on each individual antenna, and thus even exceeds the performance of the receive path with small fading only.

Moreover, Figure 4.11 compares the performance of the MRC receiver with the random antenna selection. The PER of positions with equal Γ of the measurement (in intervals of size 1 dB) is averaged for random antenna selection and MRC. It is observed that the PER saturates at around 5×10^{-3}. The MRC receiver shows much better performance in the range of 20 dB to 32 dB, while at even higher Γ both receivers show the maximum performance.

Theoretically, the performance of the MRC receiver should monotonically decrease with rising Γ. Especially at the maximum performance the MRC receiver however shows a

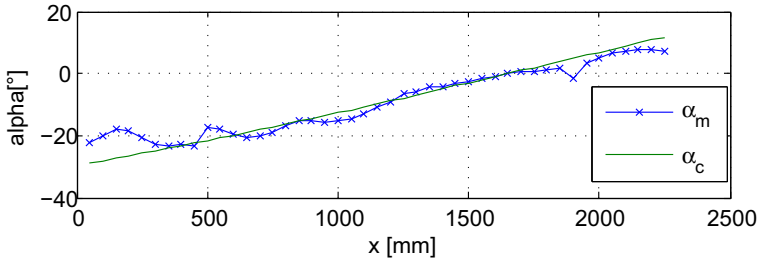

Figure 4.12: Experimental result of DOA estimation: $\alpha = 90 - \phi$.

slight increase at isolated measurement points. This increase is explained by an implemented automatic receive signal scaling to avoid overflows in multiplications at higher receive signal power, which adds additional quantisation noise.

The random antenna selection receiver however may not decrease monotonically with rising Γ, due to the limited number of positions used for averaging at a certain Γ value. Imagine, that on several positions at a certain Γ the E_b/N_0 is very high at one antenna but very low at the other. Then, Γ is mainly influenced by the higher E_b/N_0 value, while the PER is strongly dominated by the antenna with worse E_b/N_0. However, if E_b/N_0 is almost equal on both antennas, a much better average performance is expected. With the limited number of measurement points, it may happen that with increasing Γ the PER increases. Increasing the number of measurement points however is expected to result in a smooth PER behaviour. Moreover, as with the MRC receiver, the implemented automatic scaling of the receive signal at higher receive signal power may cause a performance decrease.

4.5.3 Results: Direction of Arrival Estimation

Figure 4.12 shows the experimental result of the direction of arrival estimation in terms of the incidence angle $\alpha = 90° - \phi$ (see Figure 4.7). The measurement is conducted in the scenario without artificial reflectors (quasi-anechoic), for a y-position at 1 m and variable x-position. The spacing between the two receive antennas is 30 cm, or 0.87λ for the corresponding frequency of 868 MHz. Thus, we in general expect two solutions for solving Equation (4.11). In the area $\phi \in [54.9°, 125.1°]$ however, only a single solution is obtained, which includes the measured area $\phi \in [77°, 118°]$, as depicted in Figure 4.8.

The tracked $\Delta\varphi$ value results from a propagation delay to the two receive antennas, but also from a delay difference in the frontends (for example different cable lengths). Therefore, the DOA estimation is calibrated at $\alpha = 0°$ and subsequently the frontend delay is compensated.

The measured angle α_m is plotted versus the x-position in Figure 4.12, and is compared to the calculated angle $\alpha_c = \arctan \frac{x-x_0}{y_0-y}$, where x_0 and y_0 is the position of the receive antenna. At positions $x > 2.26$ m the tag is outside the coverage area of the transmit

antenna of the reader. The maximum deviation from the calculated α_c is $10°$ on the very left side. This results form a very weak receive signal at these positions and from reflections of the wall close to the tag. The root of the averaged squared error over $N+1 = \frac{x_{max}}{\Delta x} + 1 = \frac{226}{2} + 1 = 114$ positions $\bar{\epsilon}$ is shown to be 3.34°:

$$\bar{\epsilon} = \sqrt{\frac{1}{N+1}\sum_{x=0}^{N}(\alpha_m(x) - \alpha_c(x))^2}. \tag{4.12}$$

The result demonstrates that a DOA estimation even with only two receive antennas is feasible in an environment with a strong LOS component.

4.6 Discussion and Conclusion

In contrast to today's state-of-the-art readers, where receive antennas are simply switched and only one receive antenna at a time is considered, a realisation for maximal ratio combining of a dual antenna reader receiver is shown. The realisation is not restricted to two receive antennas, and an extension to multiple antennas is straightforward. The combination is optimal in the sense of achieving maximum SNR at the reader receiver. The SNR gain comes with the tradeoff of higher hardware and signal processing complexity.

An increase of the receive SNR compared to antenna multiplexing leads to an increase of the system reliability, especially in an environment with severe fading. However, this increase of SNR can also be traded into other performance goals, such as larger readout distance or higher data throughput (compare with Section 2.3).

In fact, maximal ratio combining is a diversity combining technique. Hence, in a rich scattering environment with multipath propagation and fading this receiver exploits a diversity gain. However, if the receiver encounters equal fading realisations on both antennas or even AWGN (additive white Gaussian noise) conditions, it can still exploit an array gain.

As the receiver estimates the channel coefficients on each antenna and combines the signals with the correct phase, no a-priori knowledge of the spatial installation is required. There are no preconditions on the antenna setup. Furthermore, the presented receiver is fully standard compliant, and hence can be applied to any UHF RFID system without any modification of RFID tags. The system performance increase comes with a modification at the reader receiver only.

The maximum ratio combining is implemented on the rapid prototyping system and implementation details are provided. The measurement results show the superior performance to the common random antenna selection, used in state-of-the-art RFID readers.

Additionally, a model for DOA estimation with two antennas is presented, which is realised by the same receiver. The feasibility of direction of arrival estimation using a

dual antenna RFID reader in a quasi-anechoic scenario is demonstrated by experiments.

The proposed MRC receiver is only capable to combat fading in the backscatter link, while fading in the forward link is not addressed with this receiver. Similarly however, this issue is addressed with precoding and multiple transmit antennas, which is not addressed in this thesis but opens future work. Moreover, the DOA estimate in a quasi-anechoic case may be utilised to improve the communication link by transmit beamforming.

Additionally, this chapter treats the topic of diversity combining and DOA estimation experimentally. A qualification of the expected diversity gain is not achieved, neither a channel model is proposed on basis of the measurements. Channel modeling and measuring remains a critical issue in UHF RFID, that only very limited work has been published on [82,85,151,152]. These publications however come to the conclusion, that only general models like a two-way Rician model are feasible for fitting the measurement data, but the fading parameters (such as the K factor in Rician fading) strongly depend on the environment. Furthermore, the channel for multiple antenna readers has not yet been investigated experimentally. Another shortcoming of the experimental result is that it is based on a single tag only. The performance variations repeating the measurement with different tags have not been investigated. However, although I assume slight variations when repeating the experiments with different tags, I expect the multiple antenna diversity combining receiver to always outperform the random antenna selection scheme or the single antenna receiver.

5. SEPARATION OF MULTIPLE RFID TAGS ON THE PHYSICAL LAYER

In the previous chapters I considered the communication of the reader with a single tag. Arbitration of multiple tags in state-of-the-art radio frequency identification systems is accomplished on the medium access control layer. Thereby, all the RFID tags within the coverage area of the reader are scheduled by the Framed Slotted Aloha (FSA) protocol. Currently, only answers of a single tag can be decoded in such a system. If multiple tags respond simultaneously, a collision occurs. In that case, conventional systems discard the physical layer information and a retransmission is executed (also see Appendix C). This chapter introduces how to recover from such collisions on the physical layer and successfully read the data, even in case of a collision. Thus, the previous architectures are extended towards multiple tag communication on the physical layer rather than on the Medium Access Control (MAC) layer. This addresses the topic of throughput increase in high volume tag applications.

Recently different groups started to pay attention on slots with colliding RFID tag signals: Khasgiwale et al. [86] utilise information from tag collisions on the physical layer to estimate the number of tags involved in that specific collision slot. This information enhances the accuracy of RFID tag population estimators [153]. Furthermore, the authors point out the potential to recover from collisions and correctly read the data of the colliding tags. Shen et al. [102] rigorously analyse signal constellations of colliding tag responses. In contrast to this thesis, they focus on Low Frequency (LF) tags. Their model is supported by measurement data, and they propose a recovery algorithm for tag collisions. Additionally, they simulate the error performance in case of multiple colliding tags. Yu et al. [154] combine beamforming with anti-collision techniques, separating the tag population into sectors and running FSA or binary tree search in each sector, but do not try to recover from collisions. Lee et al. [155] identify the potential performance increase by combining smart antennas with binary tree and Slotted Aloha (SA) anti-collision algorithms, while this work focuses on FSA as defined in [17]. Mindikoglu et al. [156] develop a multiple antenna receiver for RFID collision recovery with blind source separation applying the analytic constant modulus algorithm [157]. This algorithm exploits the fact that the on-off keyed data can only be zero or one. They focus on compensation of a residual carrier offset, which in general is not present in RFID, as

pointed out in Section 3.1. In contrast to their work, I propose a channel estimation method and apply different collision recovery receivers. Bletsas et al. [158] improve the throughput in wireless sensor networks with backscatter technology by making use of directive antennas and utilising bandwith efficiently by assigning distinct subcarrier frequencies to the individual sensors.

In this chapter, I exploit the specific characteristics of RFID systems to separate signals from collisions at the physical layer. First I discuss the theoretical performance increase of an FSA system with the capability of recovering from collisions at the physical layer in the following Section 5.1. In Section 5.2 I extend the signal constellation model of the previous chapters to accurately model tag collisions and constellations in the baseband of the receiver. With this model, a channel estimation method is proposed and two classes of receivers that are capable of recovering from collisions in Section 5.3 are presented. The first class achieves a separation of colliding signals with a single antenna by analysing the I/Q constellation of the collision. The second class separates multiple colliding signals by applying multiple receive antennas, and thus exploiting the different spatial signatures of the tags. To the best knowledge of the author, these receivers are the first to be proposed for separating UHF RFID tag signals of collision slots. Both of these receiver classes are tested on measurement data of collisions in Section 5.4. A performance analysis of the proposed receivers is provided in Section 5.5. The last section finally concludes this chapter.

5.1 Framed Slotted Aloha with Physical Layer Collision Recovery

Several RFID standards, as the EPCglobal standard for UHF RFID [17], apply framed slotted aloha to arbitrate the air interface and to schedule the transmission of a tag population of N tags (compare with Appendix C). As depicted in Figure 5.1, the reader starts a frame with K slots, issuing a *Query* command, which announces the framesize K. The tags randomly select one of these following slots for transmission, whose start is indicated by *Query Repeat* commands from the reader. The response of the tags to these *Query* and *Query Repeat* commands is a 16 bit random number (*RN16*). Note that this random number in the response is *not* related with the randomly picked slot. This random number is acknowledged by the reader as a handshake mechanism (*ACK* command). Upon reception of a correct acknowledge, the arbitration process is finished and the tag returns its unique identifier. After the communication with the tag is finished, the reader announces the start of the following slot [17].

It may occur that certain slots are not used by tags for transmitting their random number (empty slots), some are used by one tag (singleton slots) or even more than one tag (collision slots), causing a collision at the air interface. A conventional reader cannot read data in a collision slot, such that data throughput only occurs in singleton slots (for example Slot 0 in Figure 5.1). If a collision occurs, either the reader detects the

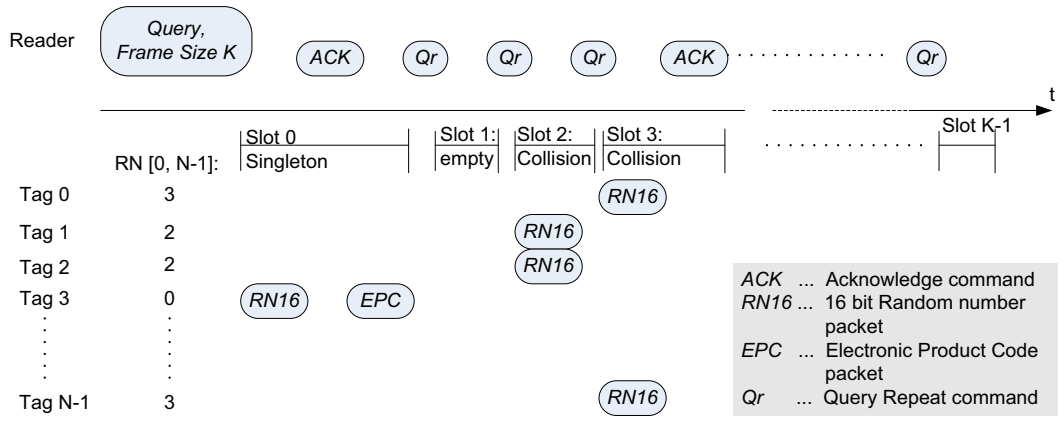

Figure 5.1: Inventory process of multiple tags with a conventional reader ($M = 1$): The reader announces a frame of size K by a *Query* command and the following K slots by the *Query Repeat* command. Tags respond with a 16 bit random number (*RN16* packet) in one of these slots. If a single tag responds in a certain slot (for example in slot 0), the *RN16* is acknowledged (*ACK* packet), as a handshake mechanism. Thereafter the tag returns its EPC code (*EPC*). If the reader detects a collision slot, it does not acknowledge the data, as for instance in slot 2. If multiple tags generate a collision but the reader does not recognise the collision, it tries to acknowledge data, but the acknowledge in Slot 3 for example is wrong. The tags do not return their EPC code. After the K slots are processed, the next frame is announced.

collision and does not acknowledge the tags (for instance Slot 2 in Figure 5.1), or it tries to acknowledge a tag. In case of a collision however, the acknowledged random number is in general wrong (for example Slot 3 in Figure 5.1). Then, the handshake is not successful and therefore the communication is terminated.

Let $\mathcal{X}_R$ be a random variable indicating the number of slots with exactly R tag responses in K slots. Then, the expected number of slots with exactly R tags transmitting is given by:

$$E\{\mathcal{X}_R\} = K\binom{N}{R}\left(\frac{1}{K}\right)^R\left(1-\frac{1}{K}\right)^{N-R}, \tag{5.1}$$

where $E\{\cdot\}$ denotes the expected value. Conventional RFID readers can only read data in singleton slots, leading to the well known maximum average throughput of $\frac{E\{\mathcal{X}_1\}}{K} = 0.368$ successful readouts per slot [159]. This throughput is achieved if the framesize is set equal to the tag population size ($K = N$), as indicated in Figure 5.2.

However, if it is possible to recover from a slot with $R \leq M$ colliding tags, we only encounter an unreadable slot if more than M tags transmit in the same slot. I first consider the case that the reader picks out one of these R tags and acknowledges this single tag, while the other received tag responses are discarded ($J = 1$). A reader with

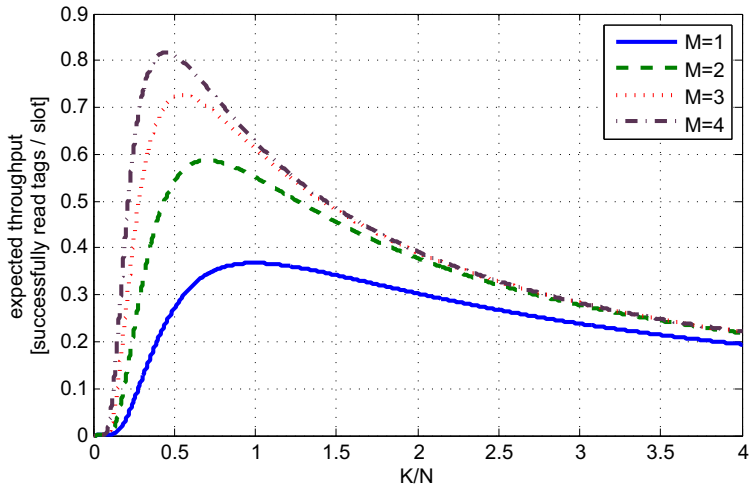

Figure 5.2: Expected throughput for a reader acknowledging one tag per slot $(J = 1)$, depending on framesize to tag ratio K/N.

$M = 2$ for example, could recover from the collision slots 2 and 3 with $R = 2$ tags in Figure 5.1. The reader acknowledges one of the 16 bit random numbers correctly, and the corresponding tag returns its EPC code, while the other tag just receives an invalid acknowledge (the one of the first tag) as in an ordinary collision slot. Then, in each slot with $R \leq M$ one tag is identified, and hence the average throughput $T = \frac{1}{K}\sum_{R=1}^{M} E\{\mathcal{X}_R\}$ can be directly computed from Equation (5.1) by:

$$T = \sum_{R=1}^{M} \binom{N}{R} \left(\frac{1}{K}\right)^{R} \left(1 - \frac{1}{K}\right)^{N-R}. \tag{5.2}$$

In order to maximise the average throughput the optimal framesize K_{opt}, can readily be derived by solving the following equation:

$$\sum_{R=1}^{M} \binom{N}{R} \left(\frac{1}{K_{opt}}\right)^{R+1} \left(1 - \frac{1}{K_{opt}}\right)^{N-R-1} \left(\frac{N}{K_{opt}} - R\right) = 0. \tag{5.3}$$

Figure 5.2 shows the expected throughput of receivers being capable to recover from collisions with up to M tags, for $N = 10\,000$. Compared to a conventional reader $(M = 1)$, a reader that is able to recover from a collision with up to $M > 1$ tags adjusts a shorter framesize for maximal throughput. This result is intuitive, as a reader with $M = 2$ for example, maximises the expected number of slots with a single $(R = 1)$ and two responses $(R = 2)$, while a conventional reader just maximises the expected number of singleton slots.

Clearly, the expected throughput increases with the parameter M, and converges toward one successfully read tag per slot for $M \to \infty$. The optimal values of framesizes

M	K_{opt}/N	expected throughput	relative improvement
1	1	0.368	1.000
2	0.707	0.587	1.595
3	0.550	0.726	1.973
4	0.452	0.817	2.220

Table 5.1: Optimal framesize K_{opt} and expected throughput for readers resolving $M = 1 \ldots 4$ collisions, but only one acknowledgment per slot ($J = 1$).

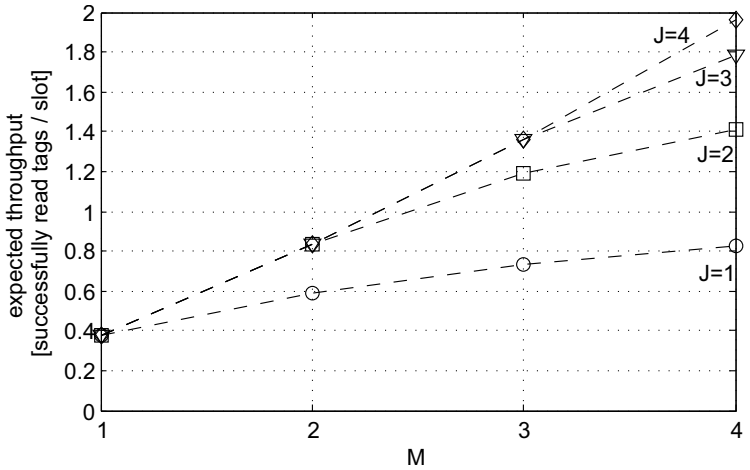

Figure 5.3: Expected throughput with optimal framesize settings for a reader with the capability to recover from a collision with M tags and to acknowledge up to J tags.

related to the tag population size and the average throughput is shown in Table 5.1 for $M = 1, \ldots, 4$. A reader with the capability to recover from a collision with two tags ($M = 2$), already achieves a theoretical increase of the expected throughput of 1.6 times the throughput of a conventional reader, motivating the development of such a receiver. Further below, I develop a signal model for collisions in the following Section 5.2, and propose corresponding reader receiver architectures with $M = 2$ in Section 5.3.

Until now we have considered the case where the reader selects one out of the decoded tags and acknowledges only this tag, while the other received signals are discarded ($J = 1$). If however the reader additionally manages to acknowledge up to J tags simultaneously (J out of the M received tags, $J \leq M$), the theoretical throughput is further increased. In the example of the collision slot 2 in Figure 5.1, a reader with $M = 2$ and $J = 2$ would first be able to decode both tags correctly on the receiver, and second would even be capable to acknowledge both tags correctly. The tags get the impression that they communicate in an ordinary singleton slot. Clearly, if both tags are acknowledged correctly, both tags also return their EPC code in the same slot, which again results in a collision that the reader has to recover from.

Consider a reader with $J \leq M$, then in each slot with $R \leq J$, R tags are successfully identified, and for each slot with $J < R \leq M$, J tags are successfully identified. Thus, the theoretical throughput $T = \frac{1}{K}(\sum_{R=1}^{J} E\{\mathcal{X}_R\}R + \sum_{R=J+1}^{M} E\{\mathcal{X}_R\}J)$ is:

$$T = \sum_{R=1}^{J} \binom{N}{R} \left(\frac{1}{K}\right)^R \left(1 - \frac{1}{K}\right)^{N-R} R + \sum_{R=J+1}^{M} \binom{N}{R} \left(\frac{1}{K}\right)^R \left(1 - \frac{1}{K}\right)^{N-R} J. \tag{5.4}$$

Similarly to the derivation above, one can calculate the optimal framesize and expected throughput. Figure 5.3 shows the expected throughput depending on the two parameters M and J. Acknowledging multiple received tags may be accomplished by exploiting the spatial separation of the tags on the transmitter by means of precoding with multiple transmit antennas [83, Chapter 8]. This requires at least partial knowledge about the forward channel, which may be extracted from the backward channel estimate, especially if the forward and backward channel exhibit a strong correlation [33,122]. Such a strong correlation is expected if the same antennas are transmitting and receiving. Moreover, the acknowledgment of multiple received tags may also be achieved by changing the standard to allow the acknowledgment of multiple tags consecutively. In this thesis I however only focus on receivers for recovering from tag collisions and leave precoding at the transmitter for future work.

5.2 Signal Constellations in Tag Collisions

5.2.1 Signal Model of Collisions on the Channel

This section extends the previously developed models of signal constellations for communicating with a single tag to collision slots (compare with Sections 3.1 and 4.1). Figure 5.4 shows the basic communication between several tags and an RFID reader, equipped with N_R receive antennas. The carrier leakage into the j'th ($j \in 1 \ldots N_R$) receive antenna results in:

$$s_j^{leak}(t) = \sqrt{2}|L_j| \sin(\omega_c t + \varphi_j^{leak}). \tag{5.5}$$

As before, the power of the transmitted continuous carrier signal is normalised to one. Given R tags transmitting in a certain slot, each tag i ($i \in 1 \ldots R$) changes from absorbing energy (tag absorb state, $S^{(a)}$) to reflecting energy (tag reflect state, $S^{(r)}$), by mismatching their antenna input impedance. This backscattered signal at tag i is given by:

$$s_{tag,i}(t) = \sqrt{2}|h_i^f|\sqrt{|\Delta\sigma_i|}a_i(t) \sin(\omega_c t + \varphi_i^f + \varphi_i^{\Delta\sigma}), \tag{5.6}$$

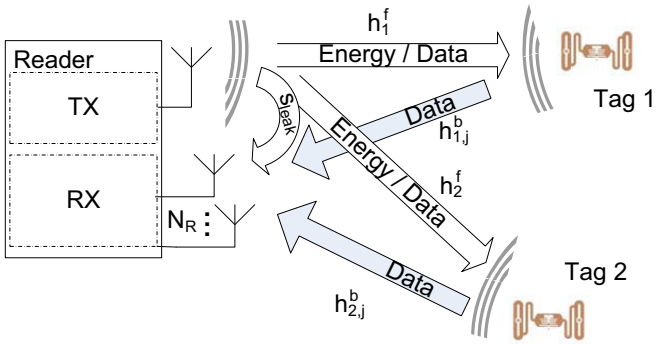

Figure 5.4: Communication between reader and two tags.

where $|h_i^f|$ and φ_i^f are the forward (reader-to-tag) channel attenuation and phase shift, respectively. The term $\varphi_i^{\Delta\sigma}$ describes the phase shift introduced by the modulation of tag i, while $|\Delta\sigma_i|$ is the normalised differential radar cross section of tag i, as defined in Section 3.1. According to the EPCglobal standard [17], each tag modulation signal $a_i(t)$ realises an on-off keying ($a[k] \in [0, 1]$), and features a *different* modulation frequency (by a different symbol period T_i) and a *distinct* delay τ_i delaying the start of the modulation phase (compare with Equation (3.3)):

$$a_i(t) = \sum_k S_i^k(t) * \delta(t - kT_i - \tau_i). \tag{5.7}$$

Here, S_i^k denotes the pulse shape of the k'th encoded symbol of tag i (compare with Section 3.1). At the $j'th$ antenna the R backscattered signals of the collision slot are distorted by the carrier leakage and additive white Gaussian passband noise:

$$s_j^{pb}(t) = \sum_{i=1}^{R} \sqrt{2}|h_{i,j}^b|\sqrt{|\Delta\sigma_i|}|h_i^f|a_i(t)\sin(\omega_c t + \varphi_i^f + \varphi_i^{\Delta\sigma} + \varphi_{i,j}^b) + s_j^{leak}(t) + n_j^{pb}(t). \tag{5.8}$$

The backward (tag-to-reader) channel between each tag i and receive antenna j inserts the attenuation $|h_{i,j}^b|$ and phase shift $\varphi_{i,j}^b$. In this model I again assume that the channel attenuations $|h_i^f|$, $|h_{i,j}^b|$ and phase shifts φ_i^f $\varphi_{i,j}^b$, as well as the tag modulation parameters $\sqrt{|\Delta\sigma_i|}$ and $\varphi_i^{\Delta\sigma}$ do not change significantly during the transmission of one packet (block fading).

5.2.2 Constellations in the Baseband of the Receiver

After receiving the collided signals at the antenna, the reader first downconverts the receive signal to the baseband. Hence, the complex-valued baseband signal at receive

antenna j is:

$$s_j(t) = \sum_{i=1}^{R} h_{i,j}^b \sqrt{\Delta\sigma_i} a_i(t) h_i^f + L_j + n_j(t), \tag{5.9}$$

with $h_i^f = |h_i^f| e^{j\varphi_i^f}$ and $h_{i,j}^b = |h_{i,j}^b| e^{j\varphi_{i,j}^b}$ denoting the complex-valued channel coefficients, $\Delta\sigma_i = |\Delta\sigma_i| e^{j2\varphi_i^{\Delta\sigma}}$ is the complex-valued normalised differential radar cross section, $L_j = |L_j| e^{j\varphi_j^{leak}}$ denotes the complex-valued carrier leakage and finally $n_j(t) = n_j^{pb}(t) e^{j\omega_c t}$ is the complex-valued noise at each antenna j with noise power spectral density N_0. Stacking the receive signals of each antenna into a vector, we can rewrite:

$$\mathbf{s}(t) = \mathbf{H}^b \mathbf{S} \mathbf{A}(t) \mathbf{h}^f + \mathbf{l} + \mathbf{n}(t). \tag{5.10}$$

Here $\mathbf{s}(t)$, $\mathbf{l}$ and $\mathbf{n}(t)$ are the $N_R \times 1$ column vectors with the elements $s_j(t)$, L_j and $n_j(t)$, respectively. The term $\mathbf{H}^b$ denotes the $N_R \times R$ tag-to-reader channel matrix with elements $h_{i,j}^b$ in row j and column i, $\mathbf{A}(t)$ and $\mathbf{S}$ are the $R \times R$ modulation and radar cross section matrices, with $a_i(t)$ and $\sqrt{\Delta\sigma_i}$ as their diagonal elements and 0 elsewhere, respectively, and $\mathbf{h}^f$ is the $R \times 1$ vector with the forward channel coefficients h_i^f. Equation (5.10) can be equivalently reformulated to:

$$\mathbf{s}(t) = \mathbf{H} \mathbf{a}(t) + \mathbf{l} + \mathbf{n}(t), \tag{5.11}$$

where $\mathbf{H} = \mathbf{H}^b \mathbf{S} \mathrm{diag}(\mathbf{h}^f)$ represents the equivalent $N_R \times R$ channel matrix with the elements $h_{i,j} = h_i^f \sqrt{\Delta\sigma_i} h_{i,j}^b$, $\mathrm{diag}(\mathbf{h}^f)$ is the $R \times R$ diagonal matrix with the elements h_i^f on its diagonal and zero elsewhere, and $\mathbf{a}(t)$ is the $R \times 1$ modulation vector with the elements $a_i(t)$.

The system describes basically a multi-user system: again some important properties are identified:

- First, due to the applied backscatter modulation, again all signal components of the receive signal, including both tag signals, are modulated to a single carrier frequency, which originates from the oscillator of the reader. Therefore, it is *feasible to jointly downconvert* all signals without any frequency offset.
- Second, the modulation signals of the R tags involved in the collision, feature a different symbol rate, which deviates up to $\pm 22\%$ between the single tags in a UHF RFID system [17]. Additionally, each tag starts its modulation phase at a different time, as indicated by the delay τ_i terms in Equation (5.7). This asynchronism makes it *unfeasible to jointly sample* all the signals with a single symbol rate.
- Finally the tag receive signals are again impaired by the strong carrier leakage and noise.

Figure 5.5 shows the constellation of two colliding tags in the baseband I/Q plane of one antenna j of the reader receiver: While both tags absorb energy, the reader

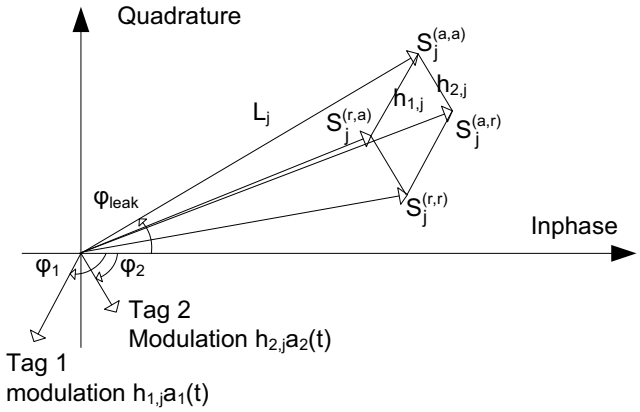

Figure 5.5: Reader baseband I/Q diagram of collision of two tags at antenna j.

only discovers the carrier leakage (absorb state of both tags, $S_j^{(a,a)} = L_j$). If Tag 1 backscatters information to the reader, this signal adds to the carrier interference and gives a second state in the I/Q plane, the Tag 1 reflect state and Tag 2 absorb state ($S_j^{(r,a)} = L_j + h_{1,j}$). The vice-versa situation, where Tag 1 absorbs energy while Tag 2 reflects energy, realises the point $S_j^{(a,r)}(= L_j + h_{2,j})$, and finally, if both tags reflect energy simultaneously, the state $S_j^{(r,r)}(= L_j + h_{1,j} + h_{2,j})$ is generated. In general, we find up to 2^R different states. Hence, the number of different states generated in the I/Q plane indicates the number of tags participating in the collision [86, 102], which can be utilised to enhance tag population estimators [64].

The location of the constellation in the I/Q plane depends on the phase and amplitude of the carrier leakage and on the channel coefficients. In general, the various states of the constellation in the I/Q plane of the receiver is unknown and arbitrary to the reader receiver, hence an estimation is required. Prior to channel estimation, again a matched filter is applied, which is realised by an integration over a half backscatter link frequency period (compare with Section 3.6). This changes the pulse shape of the tag modulation signal from rectangular to triangular. Hence, the signal moves between the states indicated in Figure 5.5. Additionally, due to the asynchronous modulation signals of the tags, the receive signals move basically within the entire area between the four states in Figure 5.6. Two synchronous tags only move on straight trajectories between the various states, as depicted in the simulated constellation of Figure 5.6a. Due to the delay difference $\Delta\tau = \tau_1 - \tau_2$ a constellation as depicted in Figure 5.6b is generated. Finally, if the BLF of both tags is distinct, a constellation as depicted in Figure 5.6c is expected. The signal moves in the entire area between the four limiting states.

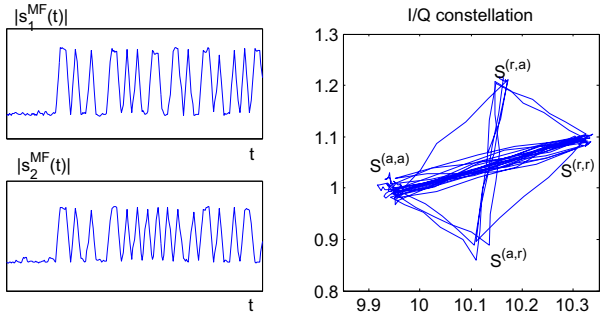

(a) Synchronous tag signals

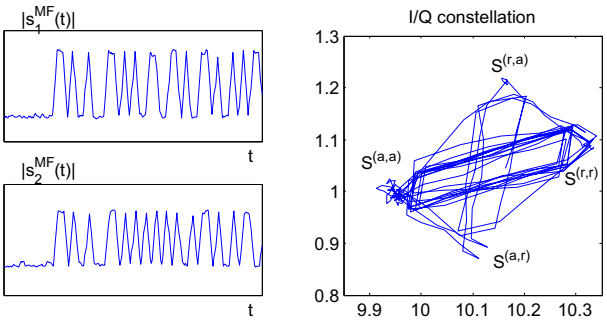

(b) Delay $\tau_1 \neq \tau_2$: $\Delta\tau$=T/10.

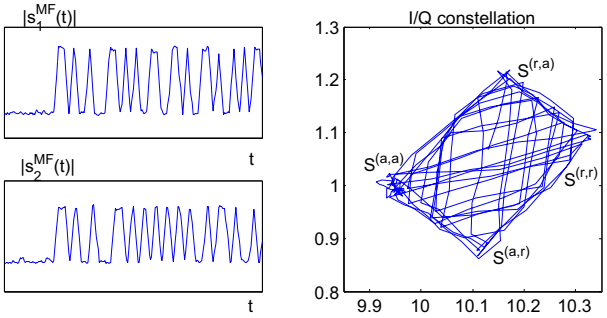

(c) BLF difference: ΔT=T/10.

Figure 5.6: Influence of synchronisation between tag responses in baseband, time domain and I/Q constellation: The signals $s_i^{MF}(t)$ denote the matched filtered baseband modulation signals $a_i(t)$. The channel coefficients and carrier leakage in the simulation are: $h_{1,j} = 0.3e^{j\pi/4}$, $h_{2,j} = 0.2e^{-j0.2\pi}$ and $L_j = 10e^{j0.1}$, respectively. The tag data for each tag in the figures are equal, however (a) depicts synchronised tags, while (b) and (c) show non-synchronous tags due to a different delay term or BLF, respectively.

5.3 Collision Resolving Receivers

With the above developed model in mind, we are now ready to develop two different classes of receiver structures:

- As a first class of receivers I propose single antenna (SA) receivers. These receivers discriminate the signal components from the two colliding tags in the I/Q plane and are capable to recover from a collision with at most two tags.

- As a second class of receivers I propose multiple receive antenna receivers. These receivers exploit the spatial domain in order to discriminate between the signal components of the two tags. I focus here on dual receive antenna receivers, also capable of recovering from slots with two tags at most. However an extension of these receivers to $N_R > 2$ receive antennas, and hence to a separation of up to $M = N_R$ tag signals is straightforward.

Both classes of receivers separate the signals in the collision slot into the components corresponding to the single tags. Synchronisation and decoding is thereafter performed for each resolved tag signal individually. This circumvents joint sampling, as all resolved tag signals may be sampled with their respective symbol frequency. As both classes of receivers require channel knowledge, a technique for estimating the channel at each antenna j for a collision slot with two tags is proposed first.

5.3.1 Channel Estimation

Reviewing Equation (5.11), we find the two tag signals of interest, degraded by the carrier leakage and noise at each antenna. While the tag signals are only active during times of backscatter modulation, the carrier is always leaking into the receiver. Assuming a static carrier leakage during one tag transmission, this carrier leakage is first estimated during times where both tags are in their absorb state $S_j^{(a,a)}$. As with the single tag receivers of the previous Chapters 3 and 4, I propose to utilise the period T_1 immediately before the tags respond, and estimate the carrier interference ($L_j = S_j^{(a,a)}$) and noise power as the temporal mean and variance during that interval T_1:

$$\hat{S}_j^{(a,a)} = E\{s_j[k]\}_{T_1}, \tag{5.12}$$

$$\hat{\sigma}_j^2 = E\{|s_j[k]|^2\}_{T_1} - |E\{s_j[k]\}|_{T_1}^2 . \tag{5.13}$$

$E\{\cdot\}_{T_1}$ again denotes the averaged value over time period T_1, and k is the sample index. For the estimation of the state $S^{(r,r)}$ I again use the preamble, where all tags modulate the same bits at the beginning. Although the tags may start with a distinct delay τ_i (compare with Equation (5.7)), the delay between two tags $\tau_1 - \tau_2$ is smaller than a half pulse period [17] (also see Appendix C). As the first symbol of the preamble has a steady level in FM0 encoding, the state $S_j^{(r,r)}$ is estimated during this first symbol of the preamble (t_{1bit}), which is determined at the largest deviation from $S_j^{(a,a)}$ in the I/Q plane:

$$\hat{S}_j^{(r,r)} = \max\left\{|s_j[k] - \hat{S}_j^{(a,a)}|\right\}_{t_{1bit}} . \tag{5.14}$$

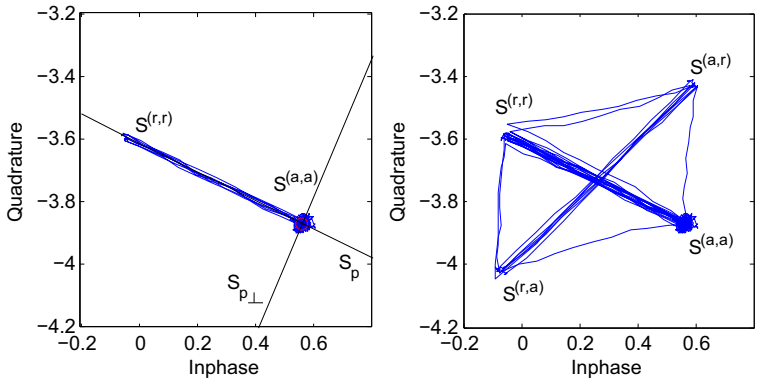

Figure 5.7: Channel estimation: simulated constellation during preamble and entire RN16 transmission for two synchronous tags.

As stated above and depicted in Figure 5.6, a matched filter is applied to the receive signal, which integrates the signal over one half symbol period and thus changes its shape from rectangular to triangular. The peaks of this triangular function thus serve as an estimate of the average over half a symbol interval of the reflection state. During the preamble, the receive signal moves between the two states $S_j^{(a,a)}$ and $S_j^{(r,r)}$, as shown in the left plot of the simulated constellation in Figure 5.7.

Finally, the realisation of the remaining states $S_j^{(a,r)}$ and $S_j^{(r,a)}$ depends on the generated data (16 bit random numbers, RN16). As soon as both tags modulate different data, these two states are realised. If only one tag responds in a certain slot, the receive signal is composed of two states and lies in a one-dimensional subspace of the I/Q plane defined by the absorb and reflect state of that tag. This subspace S_P is realised, and the two states are estimated, during the transmission of the preamble. However, if several tags generate a collision, we also find signal components in the orthogonal subspace ($S_{P\perp}$) of the preamble subspace S_P. These two orthogonal subspaces are indicated by the lines in the left plot of Figure 5.7. The states $S_j^{(a,r)}$ and $S_j^{(r,a)}$ are then estimated at the points with maximal signal strength in this orthogonal subspace component:

$$\hat{S}_j^{(a,r)} = \max_k\{s_\perp[k]\}, \quad \hat{S}_j^{(r,a)} = \min_k\{s_\perp[k]\}. \tag{5.15}$$

Here, $s_\perp[k]$ denotes the signal component located in ($S_{P\perp}$). It is insignificant if we exchange $S_j^{(a,r)}$ and $S_j^{(r,a)}$ in this estimation, as it is irrelevant which decoded signal belongs to which tag.

As the modulation signals $a_1(t)$ and $a_2(t)$ are assumed to realise perfect on-off keying, and as depicted in Figure 5.5, the channel coefficients directly correspond to:

$$\hat{h}_{1,j} = \hat{h}_1^f\sqrt{\Delta\sigma_1}\hat{h}_{1,j}^b = \hat{S}_j^{(r,a)} - \hat{S}_j^{(a,a)}, \tag{5.16}$$

$$\hat{h}_{2,j} = \hat{h}_2^f\sqrt{\Delta\sigma_2}\hat{h}_{2,j}^b = \hat{S}_j^{(a,r)} - \hat{S}_j^{(a,a)}. \tag{5.17}$$

In summary, the receiver distinguishes between zero ($R = 0$), one ($R = 1$) or more than one ($R > 1$) receive signals whether there are signal components in the subspaces S_P and $S_{P\perp}$, or if only noise is assumed in the respective components. The proposed channel estimation allows for an estimation of the states for two colliding tags, thus M is restricted to two with this algorithm. Clearly, if more tags generate a collision, a separation of the signals into two orthogonal subspaces is not sufficient to estimate all the generated states. In the case of more than two colliding tags ($R > 2$), the reader may estimate the states incorrectly, leading a fault readout of the tag data (RN16), which in general always happens for $R > M$. In that case, the acknowledged data is wrong, terminating the communication with the tags. As expected, this case (collision slot $R > M$) leads to a throughput of zero tags in that certain slot. The access of the unread tag is handled by the protocol: All tags that are not acknowledged, again participate in the following arbitration frame [17].

This thesis treats the channel estimation for collisions of two tags, an estimation for collisions of more tags is left for future work. This may be approached without applying a matched filter, but directly sampling the rectangular shaped baseband signal [86, 102]. Then, the baseband samples only realise the states corresponding to the various combinations of reflection and absorption at all the tags (as the transitions are instantaneous). In order to sample the rectangular signal shape, the supported bandwidth must be much larger than in the case of matched filtering. Therefore, this approach sacrifices on E_b/N_0, and non-synchronous tags still hamper this approach, as states do not change with a single symbol rate.

5.3.2 Single Antenna Receivers

Single Antenna Zero Forcing (SAZF) Receiver

The first proposed receiver capable of recovering from a slot with two tags colliding, is a single antenna zero forcing receiver. It separates one signal from the constellation by treating the other as interference. The signal constellation is projected into the (one-dimensional) subspace that completely cancels the interference, that is the subspace ($S_{i\perp}$) orthogonal to the interfering component (S_i, see Figure 5.8). These projected signals $\tilde{s}_i$ move between the projected states $\widetilde{S}_i^a$ and $\widetilde{S}_i^r$. The projection $\tilde{s}_i$ of each tag signal is thereafter synchronised, sliced and decoded separately (Figure 5.9).

This projection also degrades the signal strength of the desired signal, while the noise power in the projected component remains equal. Hence also the Signal to Noise Ratio (SNR) is degraded by the projection. The degradation depends on the angle between the two tag modulation signals and is proportional to $\sin(\varphi_1 - \varphi_2)$, where $\varphi_i \triangleq \varphi_i^f + \varphi_i^{\Delta\sigma} + \varphi_i^b$. Hence, if the two tag signals transmitting in the slot are close to orthogonal in the I/Q plane, the loss is small. However if the angles of the receive signals are almost equal, a high fraction of receive signal power is lost by this projection. Reviewing the signal

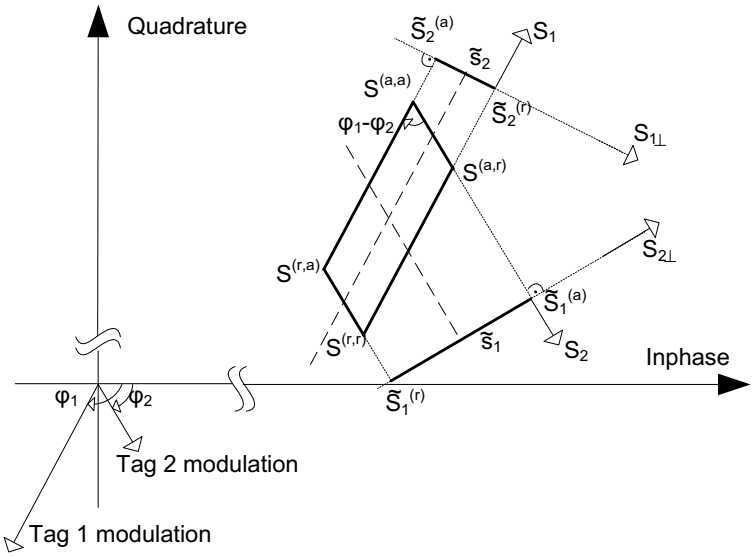

Figure 5.8: Single Antenna Zero Forcing (SAZF) receiver with projection of the constellation into the orthogonal subspace of the interference.

model, we find that the angle $\varphi_1 - \varphi_2$ is random to the receiver and distributed uniformly in $]-\pi, \pi]$.

Equivalently, the receiver can be viewed as solving Equation (5.11) with a single receive antenna:

$$s(t) = h_1 a_1(t) + h_2 a_2(t) + L + n(t), \tag{5.18}$$

with the complex-valued channel coefficients h_1 and h_2, and unknown, real-valued modulation signals $a_1(t)$ and $a_2(t)$ by:

$$\begin{aligned} \hat{a}_1(t) &= \tfrac{1}{|h_1 h_2|} \Im\left\{(s(t) - L) h_2^*\right\} \\ \hat{a}_2(t) &= \tfrac{1}{|h_1 h_2|} \Im\left\{(s(t) - L) h_1^*\right\} \end{aligned} \tag{5.19}$$

The shifted constellation $s(t) - L$ is multiplied by the complex conjugate of the channel coefficient of the the signal which is treated as interference. Thus, this signal component becomes real-valued. The selection of the imaginary part $\Im\{\cdot\}$ of the remaining signal, only constitutes the desired component.

Moreover, the zero forcing receiver can also be interpreted as a receiver, setting two separate decision thresholds inside the area spanned by the four constellation points $S^{(a,a)}$, $S^{(a,r)}$, $S^{(r,a)}$ and $S^{(r,r)}$, as indicated by the dashed lines in Figure 5.8. These decision regions are different from those of a maximum likelihood receiver. As mentioned above, the four expected constellation points are only realised if both tags realise a certain state simultaneously. Due to the asynchronous symbol rates of both tags however, the signal moves inside the area spanned by the four states, making a decision in the decision

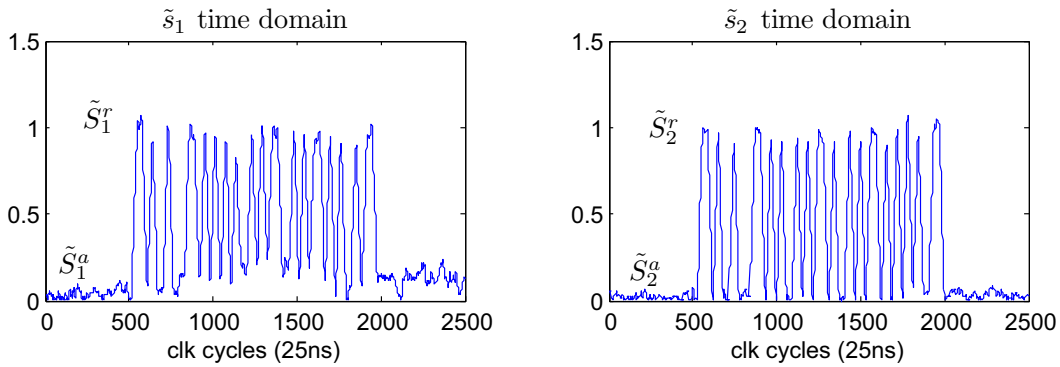

Figure 5.9: Recovered tag signals with single antenna ZF receiver (measurement data).

regions of the maximum likelihood receiver infeasible.

I explicitly underline, that this receiver is only capable of recovering from slots with two tags. If more than two tags create the signal constellation, it is not possible to find a subspace $S_{i\perp}$ which is orthogonal to both interferers in the two-dimensional I/Q space.

Single Antenna Ordered Successive Cancellation (SAOSUC) Receiver

Furthermore, I propose a single antenna ordered successive cancellation receiver, that is decoding the streams sequentially. First it selects the stream with higher receive signal power (reflected by h_i), which is first decoded by the zero forcing receiver as described above. Thereafter, the result is remodulated and subtracted from the signal constellation. Assuming the decision process was correct, the interference for the second stream is canceled [160]. Hence, the remaining signal is only composed of the signal component of the second tag. In a final step the remaining signal is sliced separately. This receiver exploits the fact, that the above described projection loss just affects the signal that is decoded first.

5.3.3 Multiple Antenna Receivers

Zero Forcing (ZF) Receiver

In order to separate the signal components by exploiting multiple receive antennas, I first propose the well known zero forcing receiver [83]:

$$\hat{\mathbf{a}}_{ZF} = (\hat{\mathbf{H}}^H \hat{\mathbf{H}})^{-1} \hat{\mathbf{H}}^H (\mathbf{s} - \hat{\mathbf{I}}). \tag{5.20}$$

The superscript $\mathbf{H}^H$ denotes the Hermitian transpose (conjugate transpose) of the matrix $\mathbf{H}$. In contrast to the single antenna receiver, it exploits the different spatial signatures

in order to separate the signals. Thus, the receiver does not suffer from a projection loss.

Minimum Mean Square Error (MMSE) Receiver

It is well known in literature [83], that the zero forcing receiver suffers from a noise enhancement due to the inversion of the matrix. The MMSE receiver takes into account both, the interference and the noise, and balances the error. Following Kay [161], the MMSE receiver of the form

$$\hat{\mathbf{a}}_{MMSE} = \mathbf{G}(\mathbf{s} - \hat{\mathbf{I}}) + \mathbf{c} \tag{5.21}$$

is based on two conditions: first, the orthogonality principle:

$$E\{(\mathbf{a} - \hat{\mathbf{a}}_{MMSE})(\mathbf{s} - \hat{\mathbf{I}})^H\} = 0, \tag{5.22}$$

and second, the condition for an unbiased receiver:

$$E\{\mathbf{a} - \hat{\mathbf{a}}_{MMSE}\} = 0. \tag{5.23}$$

Inserting Equation (5.11) in Equation (5.23) leads to the result

$$\mathbf{c} = \left(\mathbf{I} - \mathbf{G}\hat{\mathbf{H}}\right) E\{\mathbf{a}\}. \tag{5.24}$$

Proceeding with the insertion of Equations (5.21) and (5.11) into the first condition (Equation (5.22)), results in:

$$\mathbf{G} = \mathbf{C}_{aa}\hat{\mathbf{H}}^H(\hat{\mathbf{H}}\mathbf{C}_{aa}\hat{\mathbf{H}}^H + N_0\mathbf{I})^{-1}, \tag{5.25}$$

where $\mathbf{C}_{aa} = E\{(\mathbf{a} - E\{\mathbf{a}\})(\mathbf{a} - E\{\mathbf{a}\})^H\}$ denotes the covariance matrix of the data. Due to the on-off keying modulation, we find $\mathbf{C}_{aa} = \frac{1}{4}\mathbf{I}$, where $\mathbf{I}$ denotes the $N_R \times N_R$ identity matrix. Equation (5.25) is finally reformulated to:

$$\mathbf{G} = \hat{\mathbf{H}}^H(\hat{\mathbf{H}}\hat{\mathbf{H}}^H + 4N_0\mathbf{I})^{-1}. \tag{5.26}$$

Ordered Successive Cancellation (OSUC) Receiver

Another approach follows the above described idea of a cancellation receiver [162]. First the strongest signal component, characterised by $\max_i ||\hat{\mathbf{H}}(:,i)||_F$, is decoded, using either an MMSE or ZF receiver as proposed above (in the simulations in Section 5.5 it uses the MMSE). Here, $\|\cdot\|_F$ denotes the Frobenius norm, and $\hat{\mathbf{H}}(:,i)$ denotes the i'th column of $\hat{\mathbf{H}}$. Thereafter, the signal is remodulated and subtracted from the constellation. Assuming, this decoding was correct, the remaining constellation only consists of

components of the second tag signal.

Separate and Combine (S&C) Receiver

Another receiver proposed for comparison is what I call *Separate and Combine*. This receiver separates the signal components on each receive antenna individually, utilising the proposed single antenna zero forcing receiver. Thereafter, the signals from each antenna, belonging to the same tag i are combined with maximal ratio combining:

$$\hat{a}_i = \frac{1}{|\tilde{h}_{i1}|^2 + |\tilde{h}_{i2}|^2} \left(\tilde{h}_{i1}^* \tilde{s}_{i1} + \tilde{h}_{i2}^* \tilde{s}_{i2} \right), \tag{5.27}$$

where $\tilde{h}_{1j} = \tilde{S}_{1j}^{(r)} - \tilde{S}_{1j}^{(a)}$ and $\tilde{h}_{2j} = \tilde{S}_{2j}^{(r)} - \tilde{S}_{2j}^{(a)}$ are the channel coefficients h_{1j} and h_{2j} for each antenna j, projected into the subspaces $S_{2\perp}$ and $S_{1\perp}$, respectively (Figure 5.8). It is shown in Section 5.5 that for a $N_R \times R = 2 \times 2$ system the average performance of the S&C and ZF receivers is equal. However, if the channel coefficients for the two tags are correlated, the S&C receiver outperforms the ZF receiver, as it rather separates the signals in the I/Q plane instead of utilising their different spatial signatures.

We observe, that in case of a collision, the reception of both tag sequences does not increase the throughput, compared to the reception of just one of the signals, since a conventional transmitter can only acknowledge one tag at a time ($M = 2$, $J = 1$). In this situation the reader only decodes the stronger of the two tag signals, given by $\max_i |h_i|$ and $\max_i ||\mathbf{H}(:, i)||_F$ for the single and dual antenna receivers, respectively. Clearly, successive cancellation receivers do not provide any performance benefit in that case. However, if the reader manages to acknowledge both tags (either by changing the standard to acknowledge several tags consecutively, or by exploiting spatial separation of the tags using transmit precoding), we can exploit the reception of both tags to increase the throughput as given in Equation (5.4).

5.3.4 Separation of Collisions of more than two Tags by Multiple Antennas

The proposed channel estimation and single antenna receivers are restricted to a separation of two tag signals ($M = 2$). Assuming the channel matrix is known for a collision with more than two tags, the multiple antenna ZF, MMSE and OSUC receivers are capable to recover also from collisions with $R > 2$, as long as $R \leq N_R$. In that case, the channel matrix $\mathbf{H}$ in the corresponding Equations (5.20) and (5.21) is of dimension $N_R \times R$.

Moreover, due to the fact that the modulation signal $a(t)$ is real-valued, the signal model

of Equation (5.11) can be extended to:

$$\begin{pmatrix} \Re\{\mathbf{s}(t)\} \\ \Im\{\mathbf{s}(t)\} \end{pmatrix} = \begin{pmatrix} \Re\{\mathbf{H}\} \\ \Im\{\mathbf{H}\} \end{pmatrix} \mathbf{a}(t) + \begin{pmatrix} \Re\{\mathbf{I}\} \\ \Im\{\mathbf{I}\} \end{pmatrix} + \begin{pmatrix} \Re\{\mathbf{n}(t)\} \\ \Im\{\mathbf{n}(t)\} \end{pmatrix}. \tag{5.28}$$

The real and imaginary parts of **H** are independent, such that the number of equations can be doubled by selecting the real and imaginary parts (this approach is also followed in [157]). Essentially, this is exploited by the SAZF receiver for just a single antenna. This in fact allows to separate up to $R = 2N_R$ tags with N_R available receive antennas. For example, if $N_R = 2$ receive antennas observe a collision slot which is generated by $R = 2 \times N_R = 4$ tags, then the channel matrix **H** has the dimension $N_R \times R$, while the receive signal vector $\mathbf{s}(t)$, carrier leakage **I** and noise $\mathbf{n}(t)$ are of dimension $N_R \times 1$. Thus, the system of equations is under determined, and the conventional ZF, MMSE and OSUC receivers can not be applied. However, with Equation (5.28) the number of independent equations is doubled, such that the system can be solved by the proposed multiple antenna receivers.

Later, based on the example of the single antenna receiver, I will show that the ZF receiver however sacrifices on diversity order, if the above proposed doubling of equations is applied. This is due to the fact, that the selection of the real and imaginary parts do not consider the entire signal component available, while the noise stays constant, such that the SNR degrades due to this selection. In fact, the selection of the real and imaginary parts is exactly the same as the described projection loss of the SAZF receiver.

5.3.5 Complexity Comparison of the Single and Multiple Antenna Receivers

As described above, the SAZF receiver can be viewed as a conventional ZF receiver, by selecting the real- and imaginary part and thus doubling the number of equations. Both, the ZF and MMSE receivers are linear receivers that require the computation of the pseudo-inverse of the channel matrix of size $N_R \times R$, and, in case of the MMSE receiver, two vector additions (as given in Equations (5.21) and (5.26). Note however, that the SAZF receiver requires the solution of a 2×2 system of real-valued equation, while the ZF and MMSE receivers demand the inversion of a complex-valued matrix. For the SAZF receiver, the solution is obtained by Equation (5.19), which again can be efficiently computed on hardware by means of a CORDIC algorithm. The constellation is rotated such that one component is entirely real-valued. Then, the quadrature component is just comprised by the desired signal component. Similarly, the S&C receiver may be implemented as two SAZF receivers with CORDIC structures, with two additional multiplication and one addition for computing Equation (5.27). In contrast to that, the OSUC receivers require the computation of the pseudo-inverse (for either the applied ZF or MMSE receiver) in each step, which is of size $N_R \times R - k + 1$ for the k'th stream.

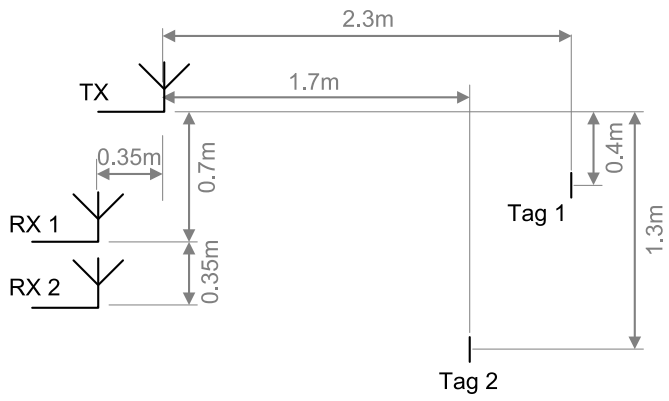

Figure 5.10: Spatial measurement setup for capturing the experimental data. The reader uses separate antennas for transmitting and the two receive paths.

5.4 Verification with Measurement Data

In order to verify both, the above presented collision model for two tags in one slot, as well as the proposed receivers, the presented receivers are run on measurement data of collisions with two commercially available tags [117]. The measurement data was recorded on the rapid prototyping platform in an indoor environment with a strong Line Of Sight (LOS) component and almost no fading. The spatial measurement setup is shown in Figure 5.10. The tags are activated by a Query command from the reader, and the collided 16 bit random number packets (RN16) of the tags at two reader receive antennas are captured after analogue to digital converters (ADC) and imported into Matlab for offline processing (Compare with Figure 4.3). Figure 5.11 shows the measurement data of the inphase and quadrature component in the time domain, as well as the I/Q constellation of the collision, for both antennas. Clearly, one can again determine the various states $S_j^{(a,a)}$, $S_j^{(a,r)}$, $S_j^{(r,a)}$ and $S_j^{(r,r)}$. As assumed in the proposed model, the data samples are located within the area defined by those states. As the modulation signal of both tags is not synchronous, the receive signal moves on trajectories, that are not directly connecting the states, as mentioned in Section 5.2 (mainly due to the delay τ_i in the example of Figure 5.11).

First, the proposed channel estimation algorithm is applied, which correctly detects the appropriate states in the constellation of the measurement data. Then, all receivers of both classes, the single antenna receivers as well as the multiple antenna receivers are applied. Figure 5.9 shows the resolved sequences of the example, applying the single antenna zero forcing receiver: The two subplots show the two projected signals $\tilde{s}_i$ into the orthogonal subspace of the interfering signal. The interference is completely canceled. Each of these resolved signals are thereafter synchronised and decoded individually.

Although the tag sequences can be decoded, a major drawback of the result is, that it is not possible to prove that the resolved sequences are decoded correctly, as the data

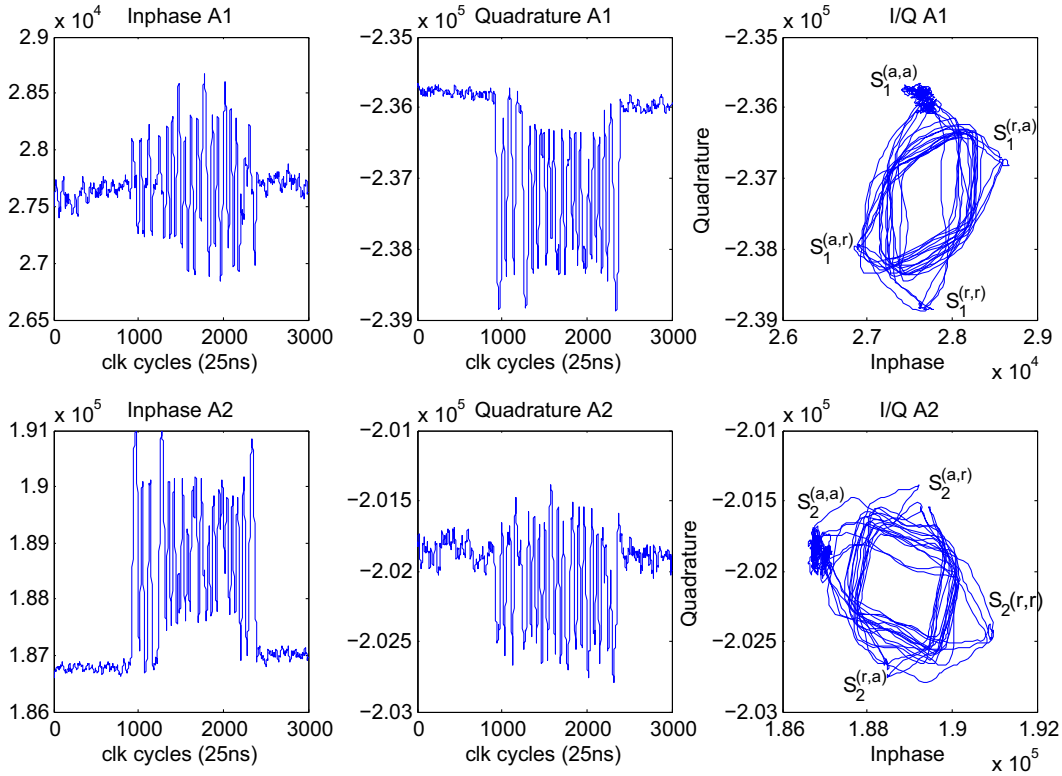

Figure 5.11: Baseband signals of measurement data of collision with two tags.

transmitted by the tags is random (tags transmit a 16 bit random number). A justification for a correct functionality however is, that the separated signals are obviously two independent, correctly encoded FM0 sequences with a valid preamble, as the reader expects them. To further validate the algorithms, the following section provides simulation results, and clearly one can verify the correct decoding of the data and the functionality of the algorithms in simulation. The assumptions in the simulation and the previously proposed model are corroborated by the measurement data. Although all receivers show a cancellation of the interfering tag sequences, exemplarily only the separated sequences of the SAZF receiver are plotted in Figure 5.9. The following performance simulations show, that this receiver actually exhibits the worst performance among all the proposed receivers.

5.5 Performance Analysis

In order to compare the performance of the various proposed receivers, the Bit Error Ratio (BER) is computed by means of Monte Carlo simulations of slots with two tag responses. Two receive antennas are assumed in the simulations for all multiple antenna receivers.

5.5.1 Rayleigh Fading Channel

For the sake of a simple comparison and analytic tractability, I assume that the equivalent channel matrix **H** follows a Rayleigh fading. The single Rayleigh channel coefficients are independent zero mean circularly symmetric complex Gaussian random variables with normalised energy $E\{|h_{i,j}|^2\} = 1$, which implies that the two tags participating in the collision experience the same path loss. Figure 5.12 shows the performance of the various Single Antenna (SA) and dual antenna receivers, decoding both tag signals of uncoded random data depending on the average output SNR $\bar{\gamma} = 1/N_R \sum_j \bar{\gamma}_j$, where $\gamma_j = |h_{i,j}|^2 a_i^2/N_0$ is the instantaneous E_b/N_0 at antenna j for tag i, and $\bar{\gamma}_j = E\{\gamma_j\}$ is the average SNR at antenna j. In addition to disturbance by noise, each stream is interfered by the second tag responding in the same slot, with the same average signal power, and the carrier leakage. The interference from other tags as well the carrier leakage however, have a different impact on the performance than the noise, as they are assumed to be known (estimated) to the receiver.

As expected, the multiple antenna receivers outperform the single antenna receivers. Further, the simple ZF receivers show a worse performance than the MMSE and OSUC (with MMSE for decoding the first stream) receivers.

Furthermore, the performance of the SAZF receiver is analysed analytically: as stated in Section 5.3.2 and depicted in Figure 5.8, the effective receive signal $\tilde{s}_i$ is degraded by the projection loss. In a first step I calculate the statistics of this projected receive signal

$$\tilde{s}_i = s_i \sin(\varphi_1 - \varphi_2), \tag{5.29}$$

where s_i follows a Rayleigh distribution and $\varphi_1 - \varphi_2$ is equally distributed in $]-\pi, \pi]$. Using the statistical independence of the two random variables, the probability density function of the projected signal $\tilde{s}_i$ is calculated by transforming the random variables [130, p. 446]. Hence, in case of Rayleigh fading on the channel, the statistics of $\tilde{s}_i$ are transformed into a Gaussian fading. Equally, the projected channel coefficients $\tilde{h}_{i,j}$ follow a Gaussian fading, with $E\{|\tilde{h}_{i,j}|^2\} = 1/2\, E\{|h_{i,j}|^2\}$.

The Bit Error Probability (BEP) for each tag signal is calculated as

$$P_b(E) = \int_0^\infty P_b(E|\gamma) p_\gamma(\gamma) d\gamma, \tag{5.30}$$

where the index of the instantaneous SNR γ is skipped as there is only a single antenna. As the modulation follows an on-off keying, the conditional BEP $P_b(E|\gamma)$ is:

$$P_b(E|\gamma) = Q(\sqrt{\gamma}), \tag{5.31}$$

where $Q(\cdot)$ denotes the Q-function. The integral is evaluated by employing the alterna-

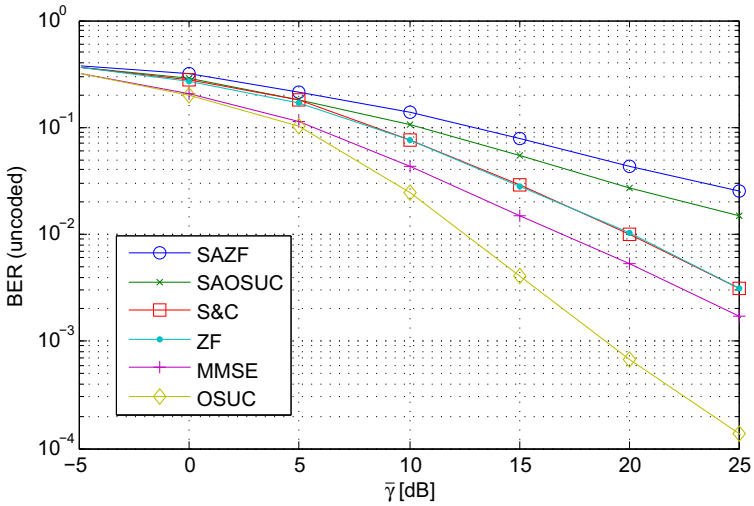

Figure 5.12: Bit Error Ratio for single and multiple antenna receivers in Rayleigh fading channel in collision slots of two tags (R=2). In the simulation, *both* tag sequences are resolved.

tive description of the Q-function by Craig [163]:

$$Q(x) = \frac{1}{\pi} \int_0^{\pi/2} \exp\left(-\frac{x^2}{2\sin^2\phi}\right) d\phi, \tag{5.32}$$

and the approach shown by Alouini et al. [164]. With the Gaussian distribution for the fading of the projected signal $\tilde{s}_i$, the distribution $p_\gamma(\gamma)$ of the instantaneous SNR γ follows a Gamma distribution. Inserting the description of the Q-function in Equation (5.32) into Equation (5.30), the bit error probability is:

$$P_b(E) = \frac{1}{\pi} \int_0^{\infty} \int_0^{\pi/2} \exp\left(\frac{-\gamma}{2\sin^2\phi}\right) d\phi\, p_\gamma(\gamma) d\gamma. \tag{5.33}$$

Changing the order of integration, the inner integral gives the moment generating function of the Gamma distribution, which is found in [164, Eq. (30)]. Hence, the BEP yields:

$$\begin{aligned} P_b(E) &= \frac{1}{\pi} \int_0^{\pi/2} \left(1 + \frac{\bar{\gamma}}{\sin^2\phi}\right)^{-1/2} d\phi. \\ &= \frac{1}{\pi\sqrt{\bar{\gamma}}} \int_0^{\pi/2} \left(\frac{\sin^2\phi}{\frac{\sin^2\phi}{\bar{\gamma}} + 1}\right)^{1/2} d\phi. \end{aligned} \tag{5.34}$$

With $\lim_{(\bar{\gamma}\to\infty)} \frac{\sin^2\phi}{\bar{\gamma}} = 0$, the BEP for large $\bar{\gamma}$ becomes

$$P_b(E) \cong \frac{1}{\pi}\bar{\gamma}^{-1/2}. \tag{5.35}$$

Hence, at high SNR $\overline{\gamma}$, the diversity order of the single antenna zero forcing receiver is found to be $1/2$, while the diversity order of the dual antenna ZF receiver is well known to be $N_R - R + 1 = 1$ [83]. Thus, by doubling the number of receive antennas from the SAZF receiver to the dual antenna ZF receiver, also the diversity order is doubled.

With the Separate and Combine (S&C) receiver, the diversity order is again improved to one. In fact the average performance of the S&C receiver and the ZF receiver is equal (Figure 5.12): In order to show that, the post-processing SNR at the output of the two receivers is compared. As both receivers scale the signal power at the output equally, the post-processing SNR is equal to the post-processing noise power.

First, the noise power $\sigma^2_{ZF,i}$ of the i'th output stream of the ZF receiver is computed, which is the element in the i'th row and i'th column (denoted by the subscript $_{ii}$) of the matrix:

$$\begin{aligned} E\left\{\mathbf{n}_{ZF}\mathbf{n}_{ZF}^H\right\} &= E\left\{(\mathbf{H}^H\mathbf{H})^{-1}\mathbf{H}^H\mathbf{n}\mathbf{n}^H\mathbf{H}((\mathbf{H}^H\mathbf{H})^{-1})^H\right\} \\ &= \sigma_n^2 E\left\{((\mathbf{H}^H\mathbf{H})^{-1})^H\right\}, \\ \sigma^2_{ZF,i} &= \sigma_n^2 E\left\{(\mathbf{H}^H\mathbf{H})^{-1}\right\}_{ii}. \end{aligned} \tag{5.36}$$

It is shown by Winters et al. [165] and Gore et al. [166], that the term $1/\{(\mathbf{H}^H\mathbf{H})^{-1}\}_{ii}$ follows a Chi-Square distribution with $N_R - R + 1$ degrees of freedom. Thus, in the actual case of $N_R = R = 2$ the expected value in Equation (5.36) is:

$$E\left\{(\mathbf{H}^H\mathbf{H})^{-1}\right\}_{ii} = \frac{1}{\sigma_h^2}, \tag{5.37}$$

with $\sigma_h^2 = E\{|h_{ij}|^2\}$. Hence, the post-processing noise power is $\sigma^2_{ZF,i} = \sigma_n^2/\sigma_h^2$.

Reviewing Equation (5.27), the noise $n_{S\&C,i}$ at the i'th output stream of the S&C receiver calculates to:

$$n_{S\&C,i} = \frac{1}{\tilde{\mathbf{h}}_i^H\tilde{\mathbf{h}}_i}\left(\tilde{\mathbf{h}}_i^H\mathbf{n}\right). \tag{5.38}$$

Here, I stack the elements $\tilde{h_{ij}}$ of Equation (5.27) into the $N_R \times 1$ vector $\tilde{\mathbf{h}}_i$. The noise power $\sigma^2_{S\&C,i}$ at the i'th output stream of the S&C receiver hence is:

$$\sigma^2_{S\&C,i} = E\left\{\frac{|\tilde{\mathbf{h}}_i^H\mathbf{n}|^2}{|\tilde{\mathbf{h}}_i^H\tilde{\mathbf{h}}_i|^2}\right\} = \sigma_n^2\, E\left\{\frac{1}{\tilde{\mathbf{h}}_i^H\tilde{\mathbf{h}}_i}\right\}. \tag{5.39}$$

As the single elements $\tilde{h}_{ij}$ exhibit independent Gaussian fading, and in addition to that $E\{|\tilde{h}_{ij}|^2\} = 1/2\, E\{|h_{ij}|^2\}$ it follows that $\tilde{\mathbf{h}}_i^H\tilde{\mathbf{h}}_i$ is Chi-square distributed with N_R

degrees of freedom and $E\{\tilde{\mathbf{h}}_i^H \tilde{\mathbf{h}}_i\} = N_R \sigma_h^2/2$. Thus, in the actual case of $N_R = 2$, the noise power of the i'th stream at the output of the S&C receiver is $\sigma_{S\&C,i}^2 = \sigma_n^2/\sigma_h^2$. Hence, the average post-processing SNR of both receivers is equivalent, resulting in the same average performance in the case of $N_R \times R = 2 \times 2$. However, if we increased the number of receive antennas, we could exploit a higher diversity order with the zero forcing receiver.

5.5.2 Dyadic Backscatter Channel

Finally, the performance of the various receivers in the dyadic backscatter channel [34,97] is simulated, assuming the fading of the forward ($\mathbf{h}^f$) and backward ($\mathbf{H}^b$) links to be uncorrelated, and perfect on-off keying modulation at the tags, that is: $\sqrt{\Delta\sigma_i} = 1$. Channel measurements carried out Lázaro et al. [152] and Kim et al. [151] propose a two-way Rician channel model, which is intuitive in RFID scenarios. They, however, point out, that the Rician factor strongly depends on the environment, and in some scenarios, the best fit to the measurement data is achieved by applying a two-way Rayleigh distribution. As the Rayleigh fading model also serves as a lower bound for Rician fading model, I stick to this assumption in the simulations. Both, forward and backward links, as well as both tags of the collision, are assumed to experience the same path loss. The data packets are FM0 encoded 16 bit random numbers as defined in [17].

Figure 5.13 shows the expected throughput of the receivers and the relative improvement to the theoretical throughput of the conventional system (0.368 tags / slot) in the FSA framework for $M = 2$, $J = 1$, as described in Section 5.1. The receivers only decode one of the two packets involved in the collision, in fact the one with the stronger receive signal, as discussed in Section 5.3. In case of a slot with a single tag response, Maximum Likelihood (ML) sequence decoding of the FM0 code for the single antenna receivers is assumed (compare with Chapter 3), and Maximal Ratio Combining (MRC) for the dual antenna case (compare with Chapter 4). It is observed, that the successive cancellation receivers do not show any further performance increase to the ZF or MMSE receivers, if only one of the packets of the collision slot is decoded. The multiple antenna receivers show a better performance than the single antenna receivers. For high $\bar{\gamma}$ the expected throughput converges towards 0.587, or equivalently, to a relative improvement of 1.595 times the theoretical throughput of the conventional system. For comparison, also the throughput of the conventional system (M=1, J=1) assuming ML sequence decoding is plotted (compare with Equation (3.17)).

Links with a correlation between the forward and the backward channel have been studied by Griffin et al. in [33]. They conclude, that the performance loss is small if the link envelope correlation $\rho_e < 0.6$, which is assumed for setups with sufficiently separated transmit and receive antennas, thus this is not considered here. Moreover, antenna correlation may be caused by not sufficient scattering and closely spaced antennas. In RFID scenarios I expect that the reader receive antenna correlation is small due to

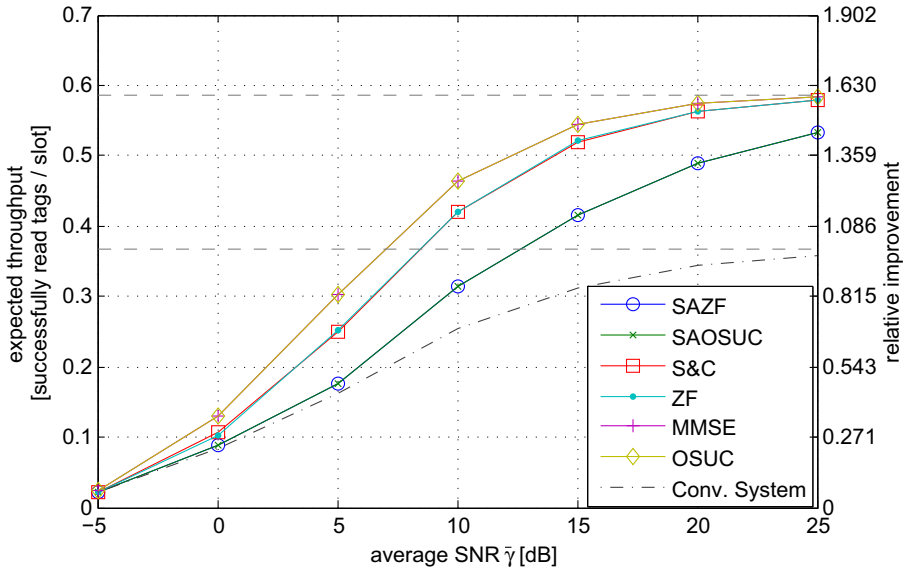

Figure 5.13: Expected throughput of FSA scheme with the capability to recover from a slot with two tags and acknowledge one tag (M=2, J=1) for the various proposed receivers. Moreover, the graph shows the relative improvement over the theoretical throughput of the conventional system (0.368 tags/slot). The two dashed horizontal lines indicate the theoretical throughput of M=1, J=1 and M=2, J=1. The gray curve plots the throughput of the conventional system with a single receive antenna with ML sequence decoding for comparison.

sufficient spacing, while the tag correlation may impacts most due to potentially close tag locations. This is modeled by [83, Chapter 3]: $\mathbf{H}^b = \mathbf{H}^b_{uc}\mathbf{R}_t^{1/2}$ and $\mathbf{h}^f = \mathbf{R}_t^{1/2}\mathbf{h}^f_{uc}$, where $\mathbf{R}_t$ is the tag covariance matrix, and $\mathbf{H}^b_{uc}$ and $\mathbf{h}^f_{uc}$ are the backward and forward channel matrix with independent Rayleigh fading, respectively. Figure 5.14 shows the expected loss in case of tag antenna correlation at $\bar{\gamma} = 10\,\text{dB}$, with $\{\mathbf{R}_r\}_{ii} = 1$ and $\{\mathbf{R}_r\}_{ij} = \rho$ for $i \neq j$. At $\rho = 0$ the throughput is the same as at 10 dB of Figure 5.13, while with full correlation $\rho = 1$ only the throughput of the single slots is achieved (MRC and ML sequence decoding in case of multiple and single antenna receivers respectively). As the S&C receiver separates the signals in the I/Q plane, it is less affected by the antenna correlation as the ZF receiver, which utilises the spatial signatures of the signals. It is observed that for $\rho < 0.6$ the system losses in terms of throughput are marginal. I however want to explicitly point out, that I am not aware of any experimental work that investigates the amount of correlation in the dyadic pinhole channel in realistic scenarios, thus the result should just provide an impression on the expected losses in case of existing antenna correlations. The extent of the correlation however is expected to depend strongly on the setup and environment, and experimental research on this topic is suggested for future work.

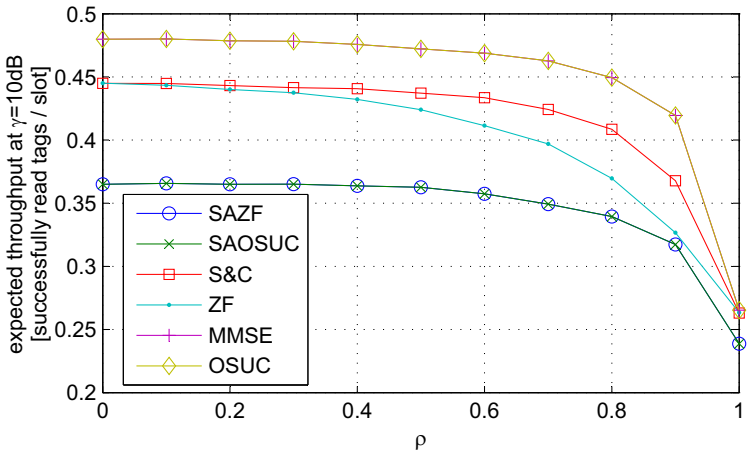

Figure 5.14: Expected throughput of FSA scheme (M=2, J=1) for the various proposed receivers with tag antenna correlation, at $\bar{\gamma} = 10\,\text{dB}$.

5.6 Discussion and Conclusion

In this chapter the theoretical throughput increase of FSA RFID systems with physical layer collision recovery receivers is identified. For a receiver capable of successfully reading and acknowledging one tag of a slot with two tags, a throughput increase of approximately 1.6 times the throughput of a conventional RFID reader is achieved. The author notes, that FSA with physical layer collision recovery is feasible in RFID, as all receive signal components are modulated to the very same carrier frequency. With that potential being identified, an accurate model for tag collisions and baseband constellations in RFID readers is developed, which enables to propose a channel estimation and guides to the development of the desired receivers. The receivers consider the main challenges of RFID systems: First, the tags participating in the collision feature highly distinct symbol rates, due to large tolerances for RFID tags. And second, the tag signals are disturbed by a strong carrier leakage. The channel estimation for $M = 2$ as well as the receivers proposed, are capable of handling these specifics of RFID systems, and assume a slowly changing carrier leakage and channel (block fading), which is true in many realistic RFID scenarios. The validity of the assumptions is corroborated by measurement data, however, in contrast to the previous chapters, the receivers are not yet implemented on the rapid prototyping environment.

The two presented classes of receivers either discriminate the tag signals in the I/Q constellation (single antenna case) or exploit their different spatial signatures (multiple antenna case). The performance of the proposed receivers is analysed analytically and by means of Monte Carlo simulations. As expected, multiple antenna receivers feature higher performance at the tradeoff of higher signal processing complexity. The SAZF receiver shows a diversity order of $1/2$. Combining the signals of two SAZF receiver outputs (S&C) allows to reconstitute the diversity order of 1, which is known to be

equal to the diversity order of the dual antenna ZF receiver. One observes that the proposed channel estimation and single antenna receivers are only capable of recovering from collisions of two tags, while the multiple antenna receivers may recover from a collision of up to $2\,M$ tags if $N_R \geq M$ receive antennas are available.

The increased data throughput of the system comes with a complexity increase at the RFID reader only. Furthermore, the receivers do not require any changes in existing RFID standards, and hence can be directly implemented in RFID receivers to work with commercially available tags, as shown by the measurement data. Although this work concentrates on FSA, the receivers can equally be applied to the binary tree anti-collision protocol.

For future work in this new research field it is intended to investigate channel estimation for multiple tag collisions involving even more than two tags ($M > 2$), which then allows to employ multiple antenna receivers to split more than two tag signals. Additionally, the applicability of multiple antenna transmitters for precoding and thereby acknowledging multiple tags simultaneously ($J > 1$) needs thorough investigation. This also requires models and experimental investigation of correlations between multiple antenna forward and backward channels in different setups. Finally, this work opens potential for higher performance tag population estimators, which utilise the physical layer information of the *exact* number of tags responding in a slot with $R \leq M$.

6 CONCLUSIONS

Although RFID is meanwhile well established in a range of special applications, state-of-the-art RFID systems still lack behind the performance demands of some generic logistic applications. For example, the proposed universal application of automated inventory of goods throughout the supply chain is in the main still fiction. As a main reason for this, the author identifies besides cost, the missing technological maturity to provide a *reliable* detection of tags, especially on the physical layer. This includes on the one hand hardware development such as tag antennas to operate on various materials, high performance RF sections or tag circuits at very low power. On the other hand however, also high performance signal processing techniques are required to push the benchmarks of RFID technology further. While signal processing is well established in other wireless communication systems, such as mobile communications, researchers only have concentrated little on this topic in the field of RFID.

Certain specifics of RFID that affect the development of advanced signal processing algorithms are identified: compared to other wireless communication systems the communication range in the RFID dyadic pinhole channel is very short and in most scenarios a line of sight connection is available. Moreover, a single carrier frequency in the overall system facilitates the design of receivers. Nevertheless, the detection of signals is challenging, due to the inherent carrier leakage of backscatter technology and the loose limits on communication parameters in the uplink communication, such as the symbol rate. Additionally, RFID systems face a strong imbalance of the signal processing load between readers and tags. As tags are only capable to execute simple operations, readers need to compensate this by applying advanced algorithms to increase the performance of the overall signal processing capabilities of the system. Thus, the thesis aims on the establishment and adaption of sophisticated signal processing techniques, which are already well established in other wireless communication systems, and their experimental evaluation. Therefore, the thesis combines the areas of signal processing, embedded systems, wireless communications and experimental techniques.

The contributions of the thesis are:

1. The setup of a flexible RFID rapid prototyping environment, which allows for the exploration of RFID systems by means of simulation and measurement. The rapid prototyping platform provides full access to a range of physical layer parameters and thus allows for the analysis of their impact on the performance of the overall RFID system. Additonally, the rapid prototyping platform supports the exploration

of the system in various scenarios. The design flow for the configuration of the system is automated, in order to accelerate the design process on the one hand, and in order to achieve consistent results between simulation and experiments on the other hand.

2. A model for receive signal constellations is developed for single and multiple receive antenna RFID readers. The model accounts for the specifics of the RFID channel, and establishes simplifying assumptions, that are valid for most RFID applications.

3. Based on that model, the performance losses from the optimal ML sequence decoder due to channel estimation and synchronisation are identified. It turns out, that synchronisation in RFID readers is the most critical task in single tag communications, due to the wide tolerances on symbol frequency in the uplink communication.

4. The single antenna receiver is extended towards a dual antenna diversity receiver. This allows to combat multipath fading and addresses the very important issue of reliability in UHF RFID systems. It is demonstrated experimentally, that diversity combining clearly outperforms random antenna selection, which is currently deployed in state-of-the-art RFID readers.

5. It is demonstrated, that direction of arrival estimation by means of two receive antenna readers is feasible, which allows for a localisation of a specific RFID tag. I could show experimentally, that in a low fading environment, the root of the squared error averaged over multiple positions of the direction of arrival estimation is as small as $3.3°$.

6. I propose physical layer collision recovery in multiple tag environments. The throughput increase of a system being capable to recover from collisions of two tags is shown to be 1.6 times the throughput of a conventional system. In this thesis, a channel estimation and two classes of receiver architectures for physical layer collision recovery, namely single antenna and multiple antenna receivers are introduced.

7. The validity of the underlying model for the development of the receiver architectures is corroborated by measurement data of realistic RFID scenarios. The receivers with single and multiple receive antennas communicating with a single tag are implemented on hardware and operate in real-time in various experimental scenarios.

Additionally, future work in the field of signal processing for RFID is proposed mainly for advanced multiple antenna transmit techniques on RFID readers. This includes beamforming and transmit diversity techniques to increase the reliability of the communication link in a hostile wireless environment. Additionally, in multiple tag environments I expect

physical layer collision recovery to be further enhanced by multiple antenna transmit precoding. Moreover, with physical layer collision recovery, more accurate information of the number of tags participating in a collision is available, which should be applied for tag population estimators. In order to establish sophisticated multiple antenna transmitters, channel measurements and modeling are required. I consider the experimental evaluation of the correlation between the forward and the backward link in the dyadic pinhole channel to be of key interest.

APPENDICES

A LIST OF TERMS AND SYMBOLS

Variable	Description
Latin symbols	
$a(t)$	Modulation signal
$\mathbf{a}(t)$	$R \times 1$ vector of modulation signals $a_i(t)$
BLF	Backscatter Link Frequency, symbol frequency
$c(t)$	Correlation function
c_0	Speed of Light
d	Antenna spacing
$E\{\cdot\}$	Expected value
E_b	Energy per bit
f_s	Sampling frequency
$h = h^f\sqrt{\Delta\sigma}h^b$	Channel coefficient
h^b	Backward channel coefficient (tag-to-reader)
h^f	Forward channel coefficient (reader-to-tag)
$h_{i,j}$	Channel coefficient from tag i to receive antenna j
$\mathbf{H}$	Equivalent channel matrix
i	Tag index
j	Receive antenna index
J	Number of tags a reader can acknowledge simultaneously
k	Wave number
K	Frame size in Framed Slotted Aloha protocol
$\mathbf{l}$	$N_R \times 1$ vector of carrier leakages $l_j(t)$
L	Carrier leakage
$n(t)$	Noise term
$\mathbf{n}(t)$	$N_R \times 1$ vector of noise terms $n_j(t)$
N	Number of tags in the read range of the reader
N_R	Number of receive antennas
N_0	Noise power spectral density
M	Reader recovery factor
OSR	Oversampling ratio
R	Number of tags generating a specific collision
$\mathbf{R}_t$	Tag antenna correlation matrix
$\mathbf{R}_r$	Receive antenna correlation matrix
$s(t)$	Baseband receive signal
$\mathbf{s}(t)$	$N_R \times 1$ vector of receive signals $s_j(t)$
$S^{(a)}$	Tag absorb state

$\tilde{S}_2^{(a)}$	Tag absorb state projected into subspace $S_{1\perp}$
S^k	k'th coded symbol
S_n	FM0 encoded symbol
$S_n(t)$	Pulse shape of symbol S_n
$s^{pb}(t)$	Passband receive signal
$S^{(r)}$	Tag reflect state
T	Symbol period

Greek symbols	
$\alpha = 90° - \phi$	Tag direction
$\mathcal{X}_R$	Random variable indicating the number of slots with R tag responses
γ_j	Instantaneous E_b/N_0 at antenna j
$\bar{\gamma}$	Average output SNR
$\Gamma = E\{\gamma_j\}$	Average SNR at one antenna
$\delta(t)$	Dirac impulse
$\Delta\sigma$	normalised differential radar cross section
φ^{leak}	Phase shift of carrier leakage
φ^b	Forward channel hase shift
φ^f	Backward channel phase shift
$\varphi^{\Delta\sigma}$	Phase shift introduced by backscatter modulation
ϕ	Direction of arrival
λ	Wavelength
ν	Sample index
$\Theta(t)$	Nominal phase increment of DDS
$\theta(t)$	Truncated phase increment of DDS
ρ	Crosscorrelation value between antennas i and $i+1$
σ_j^2	Noise variance at antenna j
σ_n^2	Noise variance
ς	Timing offset
τ	Delay term
$\upsilon \in 0 \ldots OSR$	Sampling time instant
ω_c	Angular frequency

Operators	
$E\{\cdot\}$	Expected value
$E\{\cdot\}_T$	Averaged value over time period T
h^*	Conjugate complex of h
$\mathbf{H}^H$	Hermitian transpose of matrix $\mathbf{H}$
$\Im\{\cdot\}$	Imaginary part
$Q(\cdot)$	Q-function
$\Re\{\cdot\}$	Real part

B LIST OF ACRONYMS

ACK	Acknowledge
ADC	Analogue to Digital Converter
ANSI	American National Standards Institute
ASIC	Application Specific Integrated Circuit
ASK	Amplitude Shift Keying
AWGN	Additive White Gaussian Noise
BER	Bit Error Ratio
BLF	Backscatter Link Frequency
BEP	Bit Error Probability
BER	Bit Error Ratio
CC	Continuous Carrier
CDF	Cumulative Density Function
CORDIC	Cordinated Rotation Digital Circuit
CRC	Cyclic Redundancy Check
CSR	Carrier leakage to Signal Ratio
DAC	Ditital to Analogue Converter
DDS	Direct Digital Synthesiser
DOA	Direction Of Arrival
DR	Devide Ratio
DSP	Ditital Signal Processor
DTFT	Discrete Time Fourier Transform
EDA	Electronic Design Automation
EPC	Electronic Product Code
FIFO	First In, First Out
FPGA	Field Programmable Gate Array
FSA	Framed Slotted Aloha
FSM	Finite State Machine
FT	Frequency Tolerance
HF	High Frequency
IP	Intellectual Property
ISE	Integrated Software Environment
LAN	Local Area Network
LF	Low Frequency
LOS	Line Of Sight
MAC	Medium Access Control
ML	Maximum Likelihood
MMSE	Minimum Mean Square Error

MRC	Maximal Ratio Combining
MSE	Mean Square Error
N/A	Not Applicable
NAK	Not Acknowledged
OSUC	Ordered Successive Cancellation
PA	Power Amplifier
PCB	Printed Circuit Board
PER	Packet Error Ratio
PIE	Pulse Interval Encoding
PW	Pulse Width
R→T	Reader-to Tag-communication
RAM	Random Access Memory
RAS	Random Antenna Selection
RF	Radio Frequency
RFID	Radio Frequency Identification
RMSE	Root Mean Square Error
RN16	16 bit random number packet
RT	Real-Time
RTCal	Reader-to-Tag Calibration Symbol
RX	Receive, Receiver
SAOSUC	Single Antenna Ordered Successive Cancellation
SAZF	Single Antenna Zero Forcing
SNR	Signal to Noise Ratio
S&C	Separate and Combine
T→R	Tag-to-Reader communication
TARI	Type A Reference Interval
TRCal	Tag-to-Reader Calibration Symbol
TX	Transmit, Transmitter
UHF	Ultra High Frequency
ZF	Zero Forcing

C EPCGLOBAL STANDARD FOR UHF RFID

The following Appendix should provide a coarse overview of the main definitions concerning the physical layer communication of the EPCglobal Standard for UHF RFID [17].

C.1 Physical Layer

An Interrogator sends information to one or more tags by modulating an RF carrier using Double Side Band (DSB) or Single Side Band (SSB) amplitude Shift Keying (ASK) using Pulse Interval Encoding (PIE). Tags receive their operating energy from the same modulated RF carrier. An interrogator receivers information from a tag by transmitting an unmodulated RF carrier and listening for a backscattered reply. Tags communicate information by backscatter-modulating the amplitude and / or phase of the RF carrier. The encoding format, selected in response to interrogator commands, is either FM0 or Miller modulated subcarrier. The communication link between the reader and tags is half-duplex. The communication is always initiated by the interrogator. The UHF RFID systems operate in a frequency range from 860-960 MHz.

C.1.1 Reader-to-Tag Communications

Data Encoding: The Reader-to-Tag link uses PIE encoding, as depicted in Figure C.1. The Type A Reference Interval (Tari) is the reference time interval for reader-to-tag signaling, and is the duration of a data-0. High values (A) in Figure C.1 represent the transmitted Continuous Carrier (CC), while low values (B) represent the attenuated CC, according to the ASK modulation. The parameter range of Tari, Pulse Width (PW), and the ASK modulation parameters is depicted in Table C.1. The PIE encoding with only small fractions of time transmitting the low power level guarantees a high energy transfer to the tags.

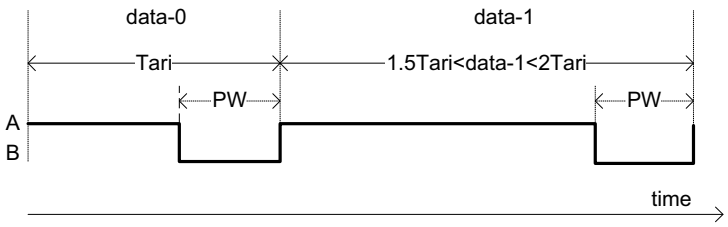

Figure C.1: Pulse Interval Encoding (PIE) for reader-to-tag communications.

Parameter	Symbol	Minimum	Typical	Maximum	Units
Type A Reference Interval	Tari	6.25		25	μs
Pulse Width	PW	max(0.265Tari, 2)		0.525Tari	μs
Modulation Depth	(A-B)/A	80	90	100	%

Table C.1: PIE encoding parameters.

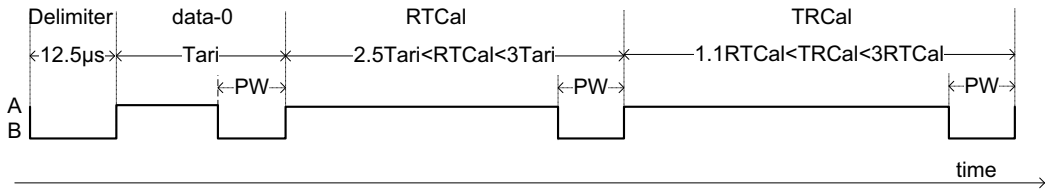

Figure C.2: Preamble for reader-to-tag communications.

Reader-to-Tag Preamble: New inventory rounds are denoted by a Query command, which starts with a preamble as depicted in Figure C.2. The preamble starts with a delimiter, followed by a data-0 symbol and the Reader-to-Tag Calibration (RTCal) and Tag to Reader Calibration (TRCal) symbol. The length of the RTCal symbol is the length of the data-0 and data-1 symbol. Thus, the tags interpret a symbol as data-0 if the symbol is smaller than RTCal/2 and as data-1, if the symbol is larger than RTCal/2.

C.1.2 Tag-to-Reader Communications

A tag communicates with a reader using backscatter modulation, in which the tag switches the reflection coefficient of its antenna between two states in accordance with the data being sent.

Modulation: Tags backscatter information to the reader by applying Amplitude Shift Keying (ASK) and / or Phase Shift Keying (PSK) modulation.

Data Encoding: Tags encode the backscattered data either using FM0 or Miller encoding. In this thesis I only focus on FM0 encoding, an extension to Miller encoding is however straightforward. Figure C.3 shows the preamble of FM0 encoding. If an extended preamble is requested by the reader, the tags modulate twelve additional '0' symbols before the preamble as shown in Figure C.3.

Data Rates: The TRCal symbol defines the Backscatter Link Frequency of the tag,

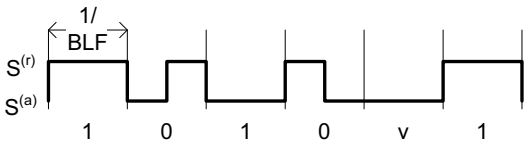

Figure C.3: FM0 preamble for tag-to-reader communications.

DR: Divide Ratio	TRcal[1] (µs +/– 1%)	LF: Link Frequency (kHz)	Frequency Tolerance FT (nominal temp)	Frequency Tolerance FT (extended temp)	Frequency variation during backscatter
64/3	33.3	640	+ / – 15%	+ / – 15%	+ / – 2.5%
	33.3 < TRcal < 66.7	320 < LF < 640	+ / – 22%	+ / – 22%	+ / – 2.5%
	66.7	320	+ / – 10%	+ / – 15%	+ / – 2.5%
	66.7 < TRcal < 83.3	256 < LF < 320	+ / – 12%	+ / – 15%	+ / – 2.5%
	83.3	256	+ / – 10%	+ / – 10%	+ / – 2.5%
	83.3 < TRcal ≤ 133.3	160 ≤ LF < 256	+ / – 10%	+ / – 12%	+ / – 2.5%
	133.3 < TRcal ≤ 200	107 ≤ LF < 160	+ / – 7%	+ / – 7%	+ / – 2.5%
	200 < TRcal ≤ 225	95 ≤ LF < 107	+ / – 5%	+ / – 5%	+ / – 2.5%
8	17.2 ≤ TRcal < 25	320 < LF ≤ 465	+ / – 19%	+ / – 19%	+ / – 2.5%
	25	320	+ / – 10%	+ / – 15%	+ / – 2.5%
	25 < TRcal < 31.25	256 < LF < 320	+ / – 12%	+ / – 15%	+ / – 2.5%
	31.25	256	+ / – 10%	+ / – 10%	+ / – 2.5%
	31.25 < TRcal < 50	160 < LF < 256	+ / – 10%	+ / – 10%	+ / – 2.5%
	50	160	+ / – 7%	+ / – 7%	+ / – 2.5%
	50 < TRcal ≤ 75	107 ≤ LF < 160	+ / – 7%	+ / – 7%	+ / – 2.5%
	75 < TRcal ≤ 200	40 ≤ LF < 107	+ / – 4%	+ / – 4%	+ / – 2.5%

Figure C.4: Backscatter Link Frequency ranges and defined deviations (from [17]).

together with the Divide Ratio (DR) setting as: BLF=DR/TRCal. The DR setting is communicated by the reader interrogation command and is either set to 8 or $8/3$. The adjustable BLF range is 40 kHz≤BLF≤640 kHz. UHF tags utilise an on-chip oscillator for timing the uplink communication. The oscillator is a multiple frequency of 640 kHz. In order to ensure low power consumption, its frequency does not exceed 1.92 MHz (=3×640 kHz). For calibrating the uplink communication, the tag samples the TRCal symbol with its internal clock (T_{clk}), and divides it by DR: $T = \left\lfloor \frac{TRCal}{DR \cdot T_{clk}} \right\rfloor T_{clk}$. Due to the relatively low internal clock frequency, the rounding operation introduces a high frequency deviation of up to $\pm 22\%$ from its nominal value at certain BLF settings [127]. Figure C.4 depicts the allowed deviations in the various selected frequency ranges.

C.1.3 Link Timings

Figure C.5 depicts the link timing parameters for a single and multiple tag communication. The parameter ranges for the timings $T_1 - T_4$ are shown in Table C.2.

C.2 Protocol Processing

The communication between a reader and one or multiple tags is split into three phases: Selection, Inventory and Access.

Selection: The process by which a reader selects a tag (sub-) population for inventory and access. The reader utilises the *Select* command, defining a certain bit-pattern in the memory of the tags to be selected. For instance, the reader may selects all tags for the next communication cycle, starting with the EPC code "0xBEEF".

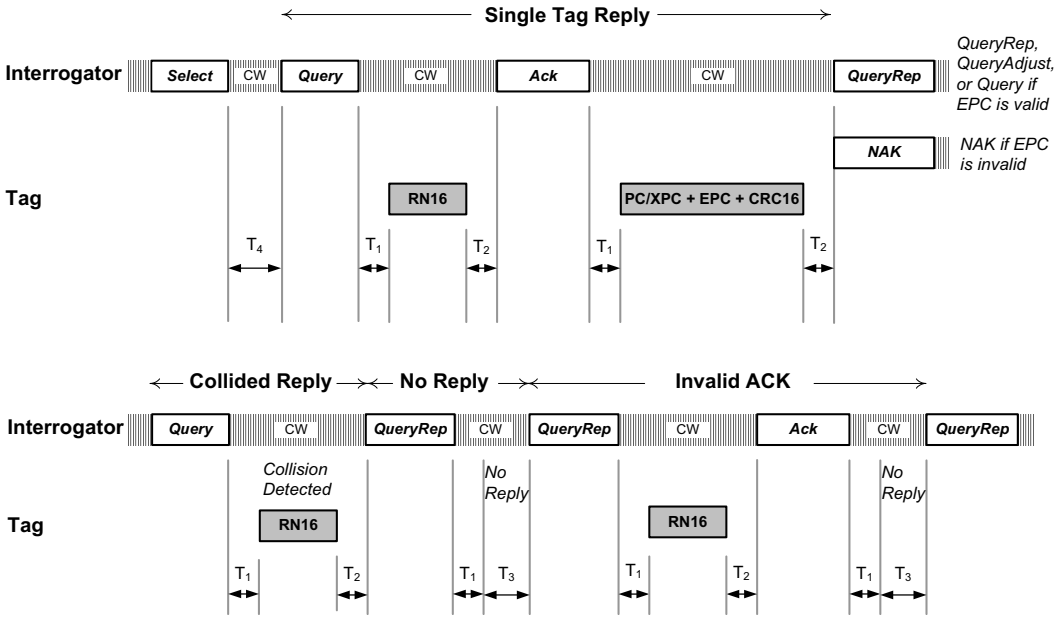

Figure C.5: Link timing parameters.

	Description	Minimum	Typical	Maximum
T_1	Time between downlink and uplink commands. FT is the Frequency Tolerance defined for the selected BLF range.	max(RTCal, 10/BLF) (1-FT) -2μs	max(RTCal, 10/BLF)	max(RTCal, 10/BLF) (1+FT) +2μs
T_2	Time between uplink and downlink commands	3/BLF		20/BLF
T_3	Time the reader waits after T_1 before issuing another command	0		
T_4	Minimum time between reader commands	2 RTCal		

Table C.2: Link timing parameters.

Inventory: Multiple tags are arbitrated by the Framed Slotted Aloha (FSA) protocol, as depicted in Figure 5.1: After selecting a tag population, the reader starts a frame spanned of K slots (framesize K). The framesize is announced by the Q-value of the *Query* command ($K = 2^Q$). All N selected tags then generate a random number smaller than 2^Q, and respond in the slot that corresponds to their random number. The slots are indicated by the reader by a *Query Repeat* command. Additionally, the reader can adjust the framesize before the end of the frame by the *Query Adjust* command. It may happen, that in a certain slot no tags (empty slot), one tag (singleton slot) or multiple tags (collision slot) respond. The tag response packet upon a *Query*, *Query Repeat* or *Query Adjust* is a 16 bit random number, the *RN16* packet (the random number in

the *RN16* command is independent from the random slot the tag selects). In case of an empty slot, no data is transmitted to the reader. In case of a singleton slot, the reader acknowledges the random number of the *RN16* command by the *Acknowledge* command, returning the random number of the *RN16*. If a tag receives a correct *Acknowledge* it returns its EPC code by the *EPC* packet. The *EPC* packet is secured by a 16 bit Cyclic Redundancy Check (CRC), and finishes the inventory phase of a tag.

Access: After a tag is inventoried, the reader may access its memory by one of the following commands: *Request Random Number, Read, Write, Kill, Lock, Access, Block Write, Block Read*. Again, a handshake mechanism with a so called "Handle" is used to guarantee that both sides are ready for communication. This handle again is a random number which is acknowledged by the *Request Random Number* command from the reader.

D MEASURED RECEIVE SIGNALS

The following appendix shows the time domain signals after the single blocks in the FPGA receiver, as depicted in Figure 3.10. The rapid prototyping hardware features two DACs. One DAC outputs the actual transmit signal, while the other is used for debugging purposes. By means of a register, the single signals of the receiver are multiplexed to this DAC, which is connected to the oscilloscope.

Additionally, the hardware provides digital outputs, that are connected to a logic analyser. The logic analyser is integrated in the oscilloscope. The setup for capturing the measurement signals is equal to the setup in Figure 4.8, with the tag located at position (x=1.5 m, y=1.5 m), that is a reader-to-tag distance of approximately 2 m. The transmit power was set to 25 dBm, the tag datasheet is found in [150].

D.1 Communication between Reader and Tag

Figure D.1 shows the oscilloscope screenshot of an EPC code readout. The top line depicts the receive signal at the intermediate frequency of 13.33 MHz, before sampling at the ADC. In the first group of digital signals below (in pink), the transmitter debug signals are shown. The first line is the PIE encoded modulation signal, before the ASK modulator of Figure 3.10. Below, the "transmit active" signal is shown, which is high

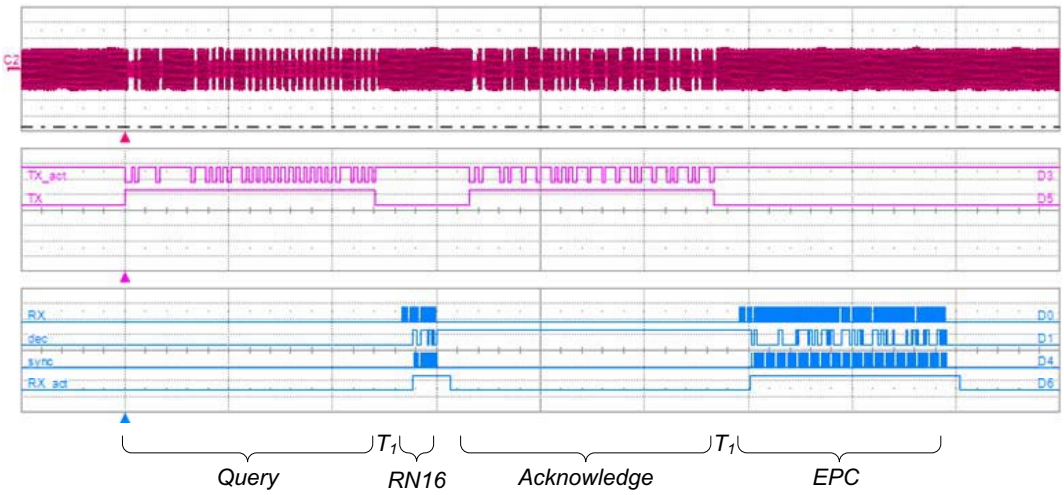

Figure D.1: Measurement of communication between reader and tag. The reader inventories the tag by reading its EPC code (compare with Appendix C).

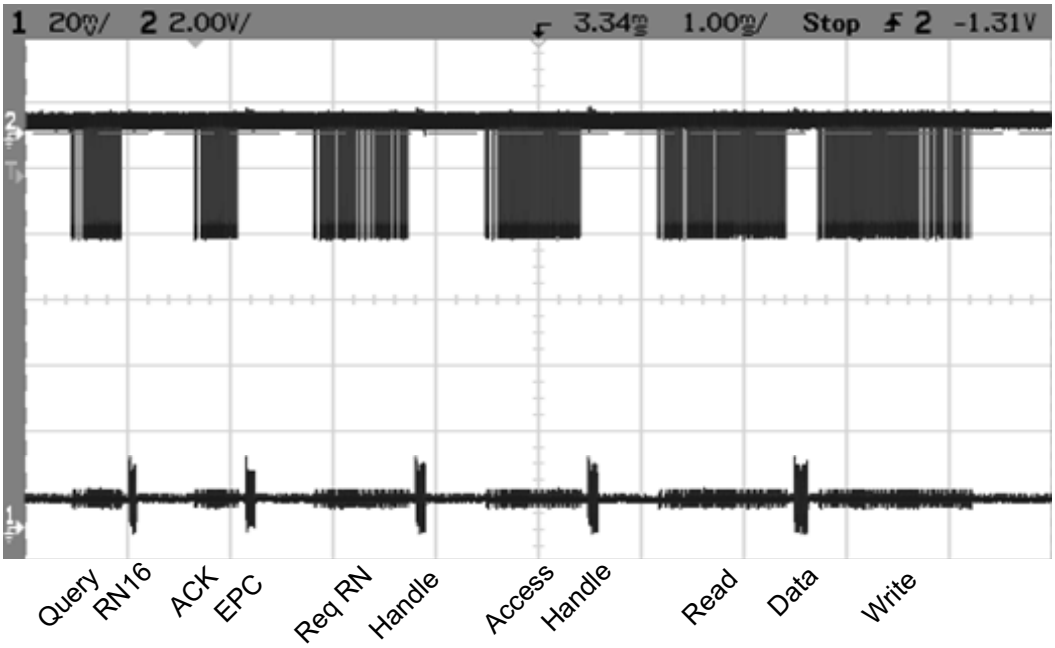

Figure D.2: Measurement of communication between reader and tag according to the EPCglobal draft standard for the HF band. The reader inventories the tag and by reading its EPC code and later accesses the tag's memory with the *Read* and *Write* commands (compare with Appendix C).

during downlink sequences. In the second group of digital signals (in blue), the receiver debug signals are shown. The top most one of this group, is the detected FM0 encoded baseband signal, below the decoded receive bits are shown. The third signal from the top is the recovered symbol clock and finally the bottom signal "receive active" is high during uplink sequences.

The transmitter always provides a constant carrier except during times of downlink modulation. The communication commands in Figure D.1 are a *Query* command of the reader, followed by the *RN16* command of the tag. The 16 bit random number is thereafter acknowledged by the reader by the *Acknowledge* command, upon which the tag returns its EPC code (*EPC* command).

Additionally, Figure D.2 provides an oscilloscope screenshot of a tag's memory access communication according to the EPCglobal draft standard for the HF domain [115]. The upper signal is the digital downlink sequence, while the lower signal depicts the reader receive packets, measured after the integration block in the receiver (Figure 3.10). According to the protocol, the tag is first inventoried, then a handshake mechanism is repeated to open the access to the tags memory issuing the *Reqest Random Number (ReqRN), Handle, Access, Handle* commands. Then, the data of a certain memory location of the tag is requested by the *Read* command, which is then returned by the tag with the *Data* packet. Finally, the reader writes data to the memory of the tag by the *Write* command (compare with Appendix C).

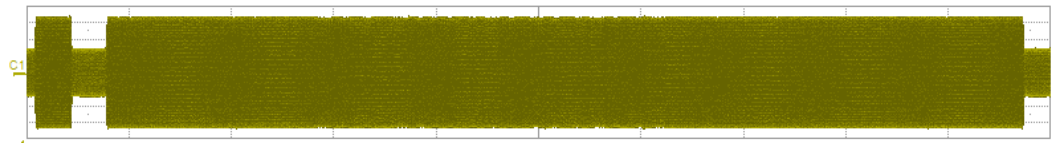

(a) ADC receive signal.

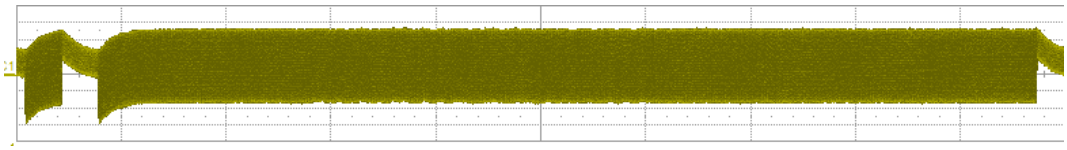

(b) Signal after sine multiplication (Q-component).

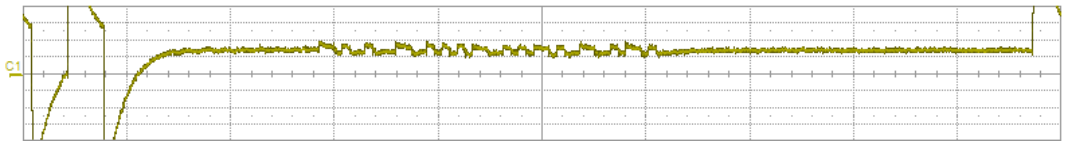

(c) Signal after low pass filter (Q-component).

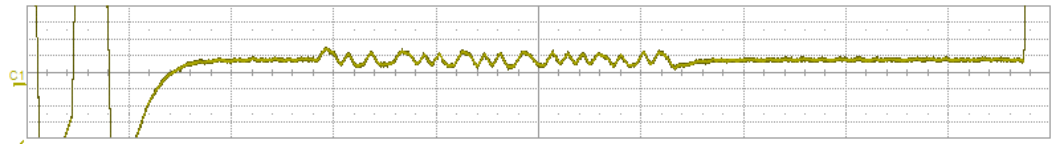

(d) Signal after integration (Q-component).

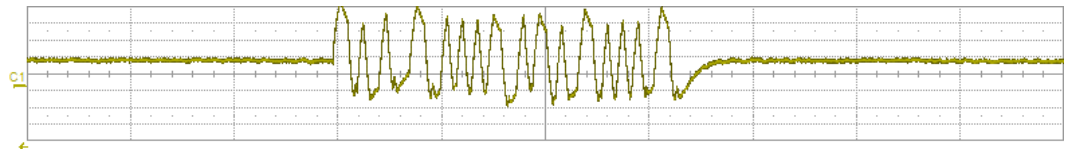

(e) Signal at the output of the channel estimation and derotation.

Figure D.3: Measurement signals after single components of the receiver (*RN16*).

D.2 Measured Signals after individual Modules of the Receiver

Figure D.3 depicts the receive signal after the single units of the receiver as given in the block diagram of Figure 3.10. The measured sequence is the 16 bit random number command (*RN16*). At the very left of the screenshots the tail of the *Query* command is still visible, and at the very right, the *Acknowledge* command follows. Figure D.3a is the sampled receive signal forwarded to the second available DAC and connected to the oscilloscope. Due to the carrier leakage, the tag receive sequence is in fact not visible. Below, in Figure D.3b the signal after the multiplication with the sine is shown. As described in Section 3.6.1, the signal contains a frequency component at 26.66 MHz which is mirrored to 13.33 MHz. Figures D.3c and D.3d depict the outputs of the subsequent low pass filter and integrator, respectively. Finally, Figure 4.5 shows the output after the derotation.

E FPGA REGISTER MAP

The following list shows the FPGA registers, which are accessible from the DSP software to control and configure the communication parameters. All registers are 16 bit wide. R stands for read only access, R/W stands for read and write access and W indicates a write only access. N/A stands for Not Applicable. The heading "A1/A2_" in the register names indicates that this register is implemented twice, once for receive path 1 and once for receive path 2.

TX LENGTH R/W

15	14:0
EN	length of TX message in bits

Number of bits of transmit command. EN is the enable bit to trigger the transmission.

RX LENGTH R

15:0
length of RX message in bits

Number of bits of decoded receive message.

TX CTRL R/W

15:10	9	8	7:2	1	0
N/A	ISO15693	Emulate Tag	N/A	Write Command	Preamble / Frame Sync.

ISO15693 generates transmit commands according to the ISO15693 protocol. Emulate Tag allows for receive signal emulation (compare with Section 3.7). The write command requires specific timings, and Preamble/Frame Sync. selects the type of preamble in downlink communications.

TARI R/W

15:0
Tari value in 40 MHz samples

MOD DEPTH R/W

15:12	11:8	7:4	3:0
N/A	high level	N/A	low level

High and low level of downlink ASK modulation. The levels are given in steps of 1/16 of the maximum transmit level.

RTCAL R/W

15:0
RTCAL value in 40 MHz samples

TRCAL R/W

15:0
TRCAL value in 40 MHz samples

RXCTRL R/W

15:6	5	4	3:2	1	0
N/A	ADC input / digital input	forward un-decoded / decoded stream	FM0, Miller, Manchester decoding	DR bit	Ext. preamble

Bits 5 and 4 are debugging options. Bits 3:2 selects the uplink encoding, bit 1 is the devide ratio bit and bit 0 selects the extended preamble in uplink communications (compare with Appendix C)

CTRL R/W

15:1	0
N/A	HF / UHF

PW R/W

15:0
PW in 40 MHz samples

PW is the pulsewidth as defined in Appendix C.

OUT MUX R/W

15:4	3:0
N/A	Debug output

Debug output signal on second DAC: ADC receive signal, I/Q demodulation signals, low pass filtered signals, matched filtered signals, correlation function c(t). Exemplary outputs are presented in Appendix D.

A1/A2_I_S0 R

15:0
Inphase Coordinate S0

A1/A2_Q_S0 R

15:0
Quadrature Coordinate S0

A1/A2_I_S1 R

15:0
Inphase Coordinate S1

A1/A2_Q_S1 R

15:0
Quadrature Coordinate S1

A1/A2_ANGLE R

15:0
Constellation Angle

The angle is given as the counter-/clockwise shifts of the single CORDIC stages for rotating the constellation to the real axis (Chapter 4).

T1 R/W

15:14	13:0
t_{2max}	t_d

Timing T_1 split in indication for t_{2max} and t_d as described in Section 3.6.3.

BLF R/W

15:0
Backscatter Link Frequency in 40 MHz samples

RX SELECTION R/W

15:2	1:0
N/A	RXSel

RXSel selects Receive antenna 1 ("01"), Receive antenna 2 ("10") and maximal ratio combining ("11").

BIBLIOGRAPHY

[1] S. Sarma, D. Brock, and D. Engels. Radio frequency identification and the electronic product code. *IEEE Micro*, 21(6):50–54, Nov./Dec. 2001.

[2] F. Michahelles, F. Thiesse, A. Schmidt, and J. R. Williams. Pervasive RFID and near field communication technology. *IEEE Pervasive Computing*, 6(3):94–96, July-Sept. 2007.

[3] S. Hodges and D. McFarlane. Radio frequency identification: technology, applications and impact. *Auto-ID Labs White Paper Series*, (1), 2005.

[4] C. M. Roberts. Radio frequency identification (RFID). *Computers & Security*, 25(1):18 – 26, 2006.

[5] L. Satpathy and A. J. Mathew. RFID assistance system for faster book search in public libraries. In *Proc. of the CHI '06 extended abstracts on Human factors in computing systems*, pages 1289–1294, Montréal, Canada, 2006.

[6] D. Molnar and D. Wagner. Privacy and security in library RFID: issues, practices and architectures. In *Proc. of the 11th ACM conference on Computer and Communications Security*, pages 210–219, Washington DC, USA, 2004.

[7] M. Gormish. Interaction between paper and electronic documents. In *Proc. of DocEng '05: ACM symposium on Document engineering*, Bristol, United Kingdom, 2005.

[8] P. Blythe. RFID for road tolling, road-use pricing and vehicle access control. *IEE Colloquium on RFID Technology (Ref. No. 1999/123)*, 1999.

[9] S.L. Garfinkel, A. Juels, and R. Pappu. RFID privacy: an overview of problems and proposed solutions. *IEEE Security & Privacy*, 3(3):34–43, May-June 2005.

[10] Z. Li, R. Gadh, and B. S. Prabhu. Applications of RFID technology and smart parts in manufacturing. In *Proc. of DETC04: ASME 2004 Design Engineering Technical Conferences and Computers and Information in Engineering Conference*, Salt Lake City, USA, Sept. 2004.

[11] K. Finkenzeller. *RFID Handbook*. John Wiley and Sons LTD, 2004. second edition, ISBN 0-470-84402-7.

[12] K.V.S. Rao. An overview of backscattered radio frequency identification system (RFID). In *Proc. of Microwave Conference, 1999 Asia Pacific*, pages 746–749 vol.3, 1999.

[13] K. Seemann and R. Weigel. The system design of integrated passive transponder devices. In *Proc. of Asia Pacific Microwave Conference*, 2006.

[14] H. Stockman. Communication by means of reflected power. *Proceedings of the IRE*, 36(10):1196–1204, Oct. 1948.

[15] D. M. Dobkin. *The RF in RFID: Passive UHF RFID in Practice*. Elseviewer, 2008.

[16] ISO / IEC. ISO / IEC 18000, RFID for Item Management: Air Interface. Part 5: Parameters for Air Interface Communication at 5.8 GHz, Jan. 2000.

[17] EPCGlobal. EPC Radio-Frequency Identity Protocols Class-1 Generation-2 UHF RFID, Oct. 2008. Version 1.2.0, http://www.epcglobalinc.org.

[18] NXP Semiconductors. UCODE G2XM, UCODE G2XL ultra high frequency smart label ICs, Dec. 2007. Document Number: 939775016225, http://www.nxp.com/acrobat_download2/literature/9397/75016225.pdf.

[19] Hitachi. Mu chip data sheet. http://www.hitachi-eu.com/mu/Products/Mu%20Chip%20Data%20Sheet.pdf.

[20] Kathrein. RRUI4, RFID UHF reader. http://www.kathrein.de/de/rfid/download/9363343d.pdf.

[21] Impinj. Indy r1000 reader chip, May 2009. www.impinj.com.

[22] austriamicrosystems AG, http://www.austriamicrosystems.com.

[23] WJ Communications, http://www.wj.com.

[24] Feig Electronic. Fixed RFID UHF long range reader, 2009. www.feig.de.

[25] S. Kobayashi, K. Sakamura, and T. Morokuma. A dynamic retargetable multi-protocol RFID reader/writer. In *Proc. of the 21st International Conference on Advanced Information Networking and Applications Workshops*, volume 2, pages 340 –346, May 2007.

[26] A. Missoni, C. Klapf, W. Pribyl, H. Guenter, and G. Holweg. A triple-band passive RFID tag. In *Proc. of the IEEE International Solid-State Circuits Conference*, San Francisco, USA, Feb. 2008.

[27] A. Missoni, C. Klapf, and G. Holweg. Dual frequency comprehensive transponder with inverse load modulation. In *Proc. of the first International EURASIP Workshop on RFID Technology*, pages 5–8, Vienna, Austria, Sept. 2007.

[28] A. Povalac, M. Zamazal, and J. Sebesta. Firmware design for a multi-protocol UHF RFID reader. In *In Proc. of the 20th International Conference Radioelektronika*, 2010.

[29] C. Floerkemeier and M. Lampe. Issues with RFID usage in ubiquitous computing applications. In *Lecture Notes in Computer Science, Pervasive Computing*, volume 3001/2004, pages 188–193. Springer, Berlin, 2004. ISBN: 978-3-540-21835-7.

[30] P.V. Nikitin and K.V.S. Rao. Performance limitations of passive UHF RFID systems. In *Proc. of the IEEE Antennas and Propagation Society International Symposium*, pages 1011–1014, July 2006.

[31] K. Penttila, L. Sydanheimo, and M. Kivikoski. Performance development of a high-speed automatic object identification using passive RFID technology. In *Proc. of the IEEE International Conference on Robotics and Automation*, volume 5, pages 4864–4868, Apr. 2004.

[32] N. Mohammed, M. Sivakumar, and D. D. Deavours. An RFID tag capable of free-space and on-metal operation. In *Proc. of the IEEE Radio and Wireless Symposium*, San Diego, USA, Jan. 2009.

[33] J. D. Griffin and G. D. Durgin. Link envelope correlation in the backscatter channel. *IEEE Communications Letter*, 11(9):735–737, Sept. 2007.

[34] J. D. Griffin and G. D. Durgin. Gains for RF tags using multiple antennas. *IEEE Transaction on Antennas and Propagation*, 56(2):563–570, Feb. 2008.

[35] R. S. Janka. *Specification and Design Methodology for Real-Time Embedded Systems*. Kluwer Academic Publishers, 2002.

[36] M. Rupp, C. Mehlführer, S. Caban, R. Langwieser, L. W. Mayer, and A. L. Scholtz. Testbeds and rapid prototyping in wireless system design. *EURASIP Newsletter*, 17(3):32–50, Sept. 2006.

[37] M. Rupp, A. Burg, and E. Beck. Rapid prototyping for wireless designs: the five-ones approach. *Signal Processing*, 83(7):1427–1444, 2003.

[38] T. Kaiser, A. Wilzeck, M. Berentsen, and M. Rupp. Prototyping for MIMO systems - an overview. In *Proc. of the XII European Signal Processing Conference*, pages 681–688, Vienna, Sept. 2004.

[39] Lyrtech, http://www.lyrtech.com.

[40] Pentek Inc., http://www.pentek.com.

[41] Nallatech Inc., http://www.nallatech.com.

[42] MATLAB / Simulink are trademarks of MathWorks, http://www.math works.com.

[43] Synopsys offers various EDA tools, http://www.synopsys/Tools/Pages/ default.aspx.

[44] Mentor Graphics EDA tools, http://www.mentor.com/products.

[45] Xilinx ISE and SystemGenerator are EDA tools especially for FPGA design and automatic conversion from Simulink to VHDL, http://www.xilinx.com.

[46] Quartus and DSPBuilder are FPGA design EDA and Simulink to VHDL conversion tools by Altera, http://www.altera.com/products/software/.

[47] Coware is an EDA tool supplier, http://www.coware.com.

[48] LabVIEW is a trademark of National Instruments, http://www.ni.com.

[49] M. Vasilko, L. Machacek, M. Matej, P. Stepien, and S. Holloway. A rapid prototyping methodology and platform for seamless communication systems. In *Proc. of the 12th International Workshop on Rapid System Prototyping*, pages 70–76, Monterey, USA, 2001.

[50] V. Derbek, C. Steger, R. Weiß, D. Wischounig, J. Preishuber-Pfluegl, and M. Pistauer. Simulation platform for UHF RFID. In *Proc. of the Design, Automation and Test in Europe - Conference and Exhibition*, Nice, France, 2007.

[51] V. Derbek, C. Steger, S. Kajtazovic, J. Preishuber-Pfluegl, and M. Pistauer. Behavioral model of UHF RFID tag for system and application level simulation. In *Proc. of the IEEE International Behavioral Modeling and Simulation Workshop*, pages 60–63, Sept. 2005.

[52] A. Janek, C. Steger, R. Weiss, J. Preishuber-Pfluegl, and M. Pistauer. Functional verification of future higher class UHF RFID tag architectures based on cosimulation. In *Proc. of the IEEE International Conference on RFID*, pages 336–343, Las Vegas, USA, Apr. 2008.

[53] I. Mayordomo, Roc Berenguer, D. Valderas, J. de No, I. Guruceaga, and I. Gutierrez. A Passive RFID System Design and Analysis focused on Reader Performance. In *Proc. of the Conference on Design of Circuits and Integrated Systems, DCIS 2007*, Nov. 2007.

[54] V. Beroulle, R. Khouri, T. Vuong, and S. Tedjini. Behavioral modeling and simulation of antennas: radio-frequency identification case study. In *Proc. of the International Workshop on Behavioral Modeling and Simulation*, pages 102–106, Oct. 2003.

[55] C. Floerkemeier and R. Pappu. Evaluation of RFIDSim - a physical and logical layer RFID simulation engine. In *Proc. of the IEEE International Conference on RFID*, Las Vegas, USA, 2008.

[56] C. Angerer, B. Knerr, M. Holzer, A. Adalan, and M. Rupp. Flexible Simulation and Prototyping for RFID Designs. In *Proc. of the first International EURASIP Workshop on RFID Technology*, pages 51–54, Vienna, Austria, Sept. 2007.

[57] C. Mutti and A. Wittneben. Robust Signal Detection in Passive RFID Systems. In *Proc. of the first International EURASIP Workshop on RFID Technology*, pages 39–42, Vienna, Austria, Sept. 2007.

[58] Y. Han, Q. Lin, and H. Min. System modelling and simulation of RFID. *AutoID Labs White paper*, Mar. 2006. http://www.auto idlabs.org.

[59] D. Arnitz, U. Muehlmann, T. Gigl, and K. Witrisal. Wideband system-level simulator for passive UHF RFID. In *Proc. of the IEEE International Conference*, pages 28–33, Orlando, USA, Apr. 2009.

[60] D.W. Engels and S.E. Sarma. The reader collision problem. In *Proc. of the IEEE International Conference on Systems, Man and Cybernetics*, volume 3, Oct. 2002.

[61] H. Vogt. Multiple object identification with passive RFID tags. In *Proc. of the IEEE International Conference on Systems, Man and Cybernetics*, volume 3, Oct. 2002.

[62] B. Knerr, M. Holzer, C. Angerer, and M. Rupp. Slot-by-slot maximum likelihood estimation of tag populations in framed slotted ALOHA protocols. In *Proc. of the International Symposium on Performance Evaluation of Computer and Telecommunication Systems*, pages 303–308, Edinburgh, UK, June 2008.

[63] C. Floerkemeier. Transmission control scheme for fast RFID object identification. In *Proc. of the Pervasive Computing and Communications Workshops*, Pisa, Italy, Mar. 2006.

[64] B. Knerr, M. Holzer, C. Angerer, and M. Rupp. Slot-wise maximum likelihood estimation of the tag population size in FSA protocols. *IEEE Transactions on Communications*, 58(2), Feb. 2010.

[65] M. V. Bueno-Delgado, J. Vales-Alonso, and F. J. Gonzalez-Castano. Analysis of DFSA anti-collision protocols in passive RFID environments. In *Proc. of the 35th Annual Conference of the IEEE Industial Electronics Society (IECON)*, Porto, Portugal, Nov. 2009.

[66] S. L. Kin, n. L. Mun, A. R. Grasso, and P. H. Cole. Synchronization of RFID readers for dense RFID reader environments. In *Proc. of the International Symposium on Applications and the Internet Workshops*, Phoenix, USA, Jan. 2006.

[67] M. Bueno Delgado, J. Vales Alonso, C. Angerer, and M. Rupp. A comparative study of RFID schedulers in dense reader environments. In *Proc. of the IEEE International Conference on Industrial Technologies*, Vina del Mar, Chile, Mar. 2010.

[68] Y.M. Lee, F. Cheng, and Y. T. Leung. Exploring the impact of RFID on supply chain dynamics. In *Proc. of the Simulation Conference*, volume 2, Dec. 2004.

[69] S. L. Kin, N. L. Mun, and P. H. Cole. Operational considerations in simulation and deployment of RFID systems. In *Proc. of the 17th International Zurich Symposium on Electromagnetic Compatibility*, pages 521–524, Singapore, Malaysia, Mar. 2006.

[70] E. Egea-Lopez, M. V. Bueno-Delgado, J. Vales-Alonso, J. Garcia-Haro, A. S. Martinez-Sala, S. Costas-Rodriguez, F. Gil-Castineira, C. Lopez-Bravo, and F. J. Gonzalez-Castano. On the implementation of a multi-reader radio frequency identification (rfid) architecture. In *Proc. of the IEEE International Symposium on Industrial Electronics*, pages 2562–2566, June 2007.

[71] P.J. Hawrylak, A. Ogirala, J.T. Cain, and M.H. Mickle. Automated test system for ISO 18000-7 - active RFID. In *Proc. of the IEEE International Conference on RFID*, pages 9–18, Las Vegas, USA, Apr. 2008.

[72] K. M. Ramakrishnan and D. D. Deavours. Performance Benchmarks for Passive UHF RFID Tags. In *Proc. of the 13th GI/ITG Conference on Measurement, Modeling, and Evaluation of Computer and Communication Systems*, 2006.

[73] L. M. Ni, Y. Liu, Y. C. Lau, and A. P. Patil. LANDMARC: indoor location sensing using active RFID. *Wireless Networks*, 10:701–710, 2004. Springer Netherlands.

[74] P. Y. Chen, W. T. Chen, Y. C. Tseng, and C. F. Huang. Providing group tour guide by RFIDs and wireless sensor networks. *IEEE Transactions on Wireless Communications*, 8(6):3059 –3067, June 2009.

[75] A. K. Jones, R. Hoare, S. Dontharaju, S. Tung, R. Sprang, J. Fazekas, J. T. Cain, and M. H. Mickle. An automated, FPGA-based reconfigurable, low-power RFID tag. *Microprocessors and Microsystems*, 31(2):116 – 134, 2007.

[76] A. K. Jones, S. Dontharaju, S. Tung, L. Mats, P. J. Hawrylak, R. R. Hoare, J. T. Cain, and M. H. Mickle. Radio frequency identification prototyping. *ACM Transactions on Design Automation of Electronic Systems*, 13(2):1–22, 2008.

[77] S. Dontharaju, S. Tung, J. T. Cain, L. Mats, M. H. Mickle, and A. K. Jones. A design automation and power estimation flow for RFID systems. *ACM Transactions on Design Automation of Electronic Systems*, 14(1):1–31, 2009.

[78] C. Angerer, M. Holzer, B. Knerr, and M. Rupp. A flexible dual frequency testbed for RFID. In *Proc. of the 4th International Conference on Testbeds and Research Infrastructures for the Development of Networks & Communities*, Innsbruck, Austria, 2008.

[79] S. Tung and A. K. Jones. Physical layer design automation for RFID systems. In *Proc. of the IEEE International Symposium on Parallel and Distributed Processing*, pages 1–8, Miami, USA, Apr. 2008.

[80] A.K. Jones, R. R. Hoare, S. R. Dontharaju, S. Tung, R. Sprang, J. Fazekas, J. T. Cain, and M. H. Mickle. A field programmable RFID tag and associated design flow. In *Proc. of the 14th Annual IEEE Symposium on Field-Programmable Custom Computing Machines*, pages 165–174, Napa, USA, Apr. 2006.

[81] P. V. Nikitin and K. V. S. Rao. LabVIEW-based UHF RFID tag test and measurement system. *IEEE Transactions on Industrial Electronics*, 56(7), Jul. 2009.

[82] J. D. Griffin and G. D. Durgin. Multipath fading measurements for multi-antenna backscatter RFID at 5.8 GHz. In *Proc. of the 2009 IEEE International Conference on RFID*, pages 322 –329, Apr. 2009.

[83] A. Paulraj, R. Nabar, and D. Gore. *Introduction to Space-Time Wireless Communication*. Cambridge University Press, 2003.

[84] A. F. Molisch. *Wireless Communications*. John Wiley and Sons, 2005.

[85] L. W. Mayer, M. Wrulich, and S. Caban. Measurement and channel modeling for short range indoor UHF applications. In *Proc. of European Conference on Antennas and Propagation (EuCAP)*, Nice, France, Nov. 2006.

[86] R. S. Khasgiwale, R. U. Adyanthaya, and D. W. Engels. Extracting information from tag collisions. In *Proc. of the IEEE International Conference on RFID*, Orlando, USA, Apr. 2009.

[87] C. Angerer and R. Langwieser. Flexible Evaluation of RFID System Parameters using Rapid Prototyping. In *Proc. of the IEEE International Confenerence on RFID*, Orlando, USA, Apr. 2009.

[88] C. Angerer. A digital receiver architecture for RFID readers. In *Proc. of the IEEE 3rd International Symposium on Industrial Embedded Systems*, pages 97–102, Montpellier, France, June 2008.

[89] C. Angerer and M. Rupp. Advanced synchronisation and decoding in RFID reader receivers. In *Proc. of the IEEE Radio and Wireless Symposium*, San Diego, USA, Jan. 2009.

[90] M. Simon and D. Divsalar. Some interesting observations for certain line codes with application to RFID. *IEEE Transactions on Communications*, 54(4), Apr. 2006.

[91] Y. Liu, C. Huang, H. Min, G. Li, and Y. Han. Digital correlation demodulator design for RFID reader receiver. In *Proc. of the Wireless Communications and Networking Conference (WCNC 2007)*, pages 1664–1668, Kowloon, China, Mar. 2007.

[92] C. Huang and H. Min. A new method of synchronization for RFID digital receivers. In *Proc. of the 8th International Conference on Solid-State and Integrated Circuit Technology, 2006. ICSICT '06*, pages 1595–1597, Shanghai, China, 2006.

[93] J. R. Barry, E. A. Lee, and D. G. Messerschmitt. *Digital Communication*. Springer, third edition, 2004.

[94] C. Angerer, R. Langwieser, G. Maier, and M. Rupp. Maximal ratio combining receivers for dual antenna RFID readers. In *Proc. of the IEEE MTT-S International Microwave Workshop Series on Wireless Sensing, Local Positioning and RFID*, Cavtat, Croatia, Sept. 2009.

[95] C. Angerer, R. Langwieser, and M. Rupp. Experimental performance evaluation of dual antenna diversity receivers for RFID readers. In *Proc. of the Third International EURASIP Workshop on RFID Technology*, Spain, Sept. 2010.

[96] P. V. Nikitin and K. V. S. Rao. Performance of RFID tags with multiple RF ports. In *Proc. of the IEEE Antennas and Propagation Society International Symposium*, pages 5459–5462, June 2007.

[97] M. A. Ingram, M. F. Demirkol, and D. Kim. Transmit diversity and spatial multiplexing for RF links using modulated backscatter. In *Proc. of the International Symposium on Signals, Systems, and Electronics (ISSSE'01)*, July 2001.

[98] C. Angerer, R. Langwieser, and M. Rupp. Direction of arrival estimation by phased arrays in RFID. In *Proc. of the Third International EURASIP Workshop on RFID Technology*, Spain, Sept. 2010.

[99] P. V. Nikitin, R. Martinez, S. Ramamurthy, H. Leland, G. Spiess, and K. V. S. Rao. Phase based spatial identification of UHF RFID tags. In *Proc. of the IEEE International Conference on RFID*, Apr. 2010.

[100] C. Hekimian-Williams, B. Grant, X. Liu, Z. Zhang, and P. Kumar. Accurate localization of RFID tags using phase difference. In *Proc. of the IEEE International Conference on RFID*, Apr. 2010.

[101] G. Jin, X. Lu, and M. Park. An indoor localization mechanism using active RFID tag. In *Proc. of the IEEE International Conference on Sensor Networks, Ubiquitous, and Trustworthy Computing.*, June 2006.

[102] D. Shen, G. Woo, D. P. Reed, A. B. Lippman, and J. Wang. Separation of multiple passive RFID signals using software defined radio. In *Proc. of the IEEE International Conference on RFID*, Orlando, USA, Apr. 2009.

[103] C. Angerer, G. Maier, M. V. Bueno-Delgado, M. Rupp, and J. Vales-Alonso. Single antenna physical layer collision recovery receivers for RFID readers. In *Proc. of the International Conference on Industrial Technologies*, Viña del Mar, Chile, 2010.

[104] C. Angerer, R. Langwieser, and M. Rupp. RFID reader receivers for physical layer collision recovery. *IEEE Transactions on Communications*.

[105] G. Meindl-Pfeiffer, R. Kloibhofer, F. Kaltenberger, and G. Humer. Multi-standard development and measuring platform for mimo-software defined radio. In *Proc. of the EUSIPCO, European Signal Processing Conference*, Sept. 2005. invited.

[106] R. Langwieser, G. Lasser, C. Angerer, M. Rupp, and A.L. Scholtz. A modular UHF reader frontend for a flexible RFID testbed. In *Proc. of the 2nd Int. EURASIP Workshop on RFID Technology*, Budapest, Hungary, July 2008.

[107] R. Langwieser, C. Angerer, and A.L. Scholtz. A UHF frontend for MIMO applications in RFID. In *Proc. of the IEEE Radio and Wireless Symposium*, New Orleans, USA, Jan. 2010.

[108] R. Langwieser, G. Lasser, C. Angerer, M. Fischer, and A.L. Scholtz. Active carrier compensation for a multi-antenna RFID frontend. In *Proc. of the IEEE International Microwave Symposium*, Anaheim, USA, May 2010.

[109] G. Lasser, R. Langwieser, and A.L Scholtz. Broadband Suppression Properties of Active Leaking Carrier Cancellers. In *Proc. of the IEEE International Confenerence on RFID*, Orlando, USA, Ap. 2009.

[110] N. Roy, A. Trivedi, and J. Wong. Designing an FPGA-Based RFID Reader. *XCell Journal*, pages 26–29, Second Quater 2006.

[111] C. Ying and Z. Fu-hong. A system design for UHF RFID reader. In *Proc. of ICCT 2008: 11th IEEE International Conference on Communication Technology*, pages 301–304, Hangzhou, China, Nov. 2008.

[112] C. Huang, Y. Liu, Y. Han, and H. Min. A new architecture of UHF RFID digital receiver for SoC implementation. In *Proc. of the Communications and Networking Conference (WCNC 2007)*, pages 1659–1663, Kowloon, China, Mar. 2007.

[113] K. Choi, Y. Eo, S. Jung, I. Kwon, H. B. Lee, and Y. j. Kim. A fully integrated CMOS RF transmitter for UHF mobile RFID reader applications. In *Proc. of EuRAD 2007: European Radar Conference*, pages 369–372, Munich, Germany, Oct. 2007.

[114] I. Kipnis, S. Chiu, M. Loyer, J. Carrigan, J. Rapp, P. Johansson, D. Westberg, and J. Johansson. A 900 MHz UHF RFID reader transceiver IC. In *Proc. of ISSCC 2007. Digest of Technical Papers. IEEE International Solid-State Circuits Conference*, pages 214–598, Feb. 2007.

[115] EPCGlobal. EPC Global HF Air Interface Version 2, Document Version 0.1, Nov. 2006.

[116] ISO / IEC. ISO / IEC 15693, Identification Cards - Contactless Integrated Circuit Cards - Vicinity Cards, Jan. 2000.

[117] UPM Raflatac, RFID. Rafsec web paper tag, global UHF C1G2 EPC, May 2007. Product Specification, Version 1.1.

[118] P. V. Nikitin, K. V. S. Rao, and R. D. Martinez. Differential RCS of RFID tag. *Electronic Letters*, 43(8):431–432, Apr. 2007.

[119] L. W. Mayer and A. L. Scholtz. Sensitivity and impedance measurements on UHF RFID transponder chips. In *Proc. of the second International EURASIP Workshop on RFID Technology*, Budapest, Hungary, 2008.

[120] L. W. Mayer. *Antenna design for future multi-standard and multi-frequency RFID systems*. PhD thesis, Vienna University of Technology, 2009.

[121] Impinj. *Impinj Monza EPCglobal Generation 2 RFID, Datasheet*, 2005.

[122] D. Y. Kim, H. S. Jo, H. Yoon, C. Mun, B. J. Jang, and J. G. Yook. Reverse-link interrogation range of a UHF MIMO-RFID system in Nakagami- m fading channels. *IEEE Transactions on Industrial Electronics*, 57(4):1468 –1477, Apr. 2010.

[123] L. W. Mayer, R. Langwieser, and A. L. Scholtz. Evaluation of passive carrier-suppression techniques for UHF RFID systems. In *Proc. of the IEEE MTT-S International Microwave Workshop on Wireless Sensing, Local Positioning and RFID*, Cavtat, Croatia, Sept. 2009.

[124] G. Lasser, R. Langwieser, and A. L. Scholtz. Broadband suppression properties of active leaking carrier cancellers. In *Proc. of the IEEE International Conference on RFID*, Orlando, USA, Apr. 2009.

[125] P.V. Nikitin and K.V.S. Rao. Antennas and propagation in UHF RFID systems. In *Proc. of the IEEE International Conference on RFID*, pages 277–288, Apr. 2008.

[126] Y. Liu, Q. Zhang, and M. Zheng. Signal analysis and design criteria for UHF RFID reader. In *ITS Telecommunications Proceedings, 2006 6th International Conference on*, pages 233–236, Jun. 2006.

[127] Impinj. Gen 2 tag clock rate - what you need to know, 2005. available at: http://www.impinj.com/WorkArea/linkit.aspx?LinkIdentifier=id&ItemID=2541.

[128] F. Cilek, K. Seemann, G. Holweg, and R. Weigel. Impact of the local oscillator on baseband processing in RFID transponder. In *Proc. of the International Symposium on Signals, Systems and Electronics*, pages 231 –234, 2007.

[129] H. Kobayashi. Simultaneous adaptive estimation and decision algorithm for carrier modulated data transmission systems. *IEEE Transactions on Communication Technology*, 19(3):268 –280, June 1971.

[130] T. K. Moon and W. C. Stirling. *Mathemetical Methods and Algorithms for Signal Processing*. Prentice Hall, 2000.

[131] R. Schmidt. Multiple emitter location and signal parameter estimation. *IEEE Transactions on Antennas and Propagation*, 34(3):276 – 280, Mar. 1986.

[132] Y. S. Poberezhskiy and G. Y. Poberezhskiy. Flexible analog front ends of reconfigurable radios based on sampling and reconstruction with internal filtering. *EURASIP Journal on Wireless Communications and Networking*, 2005(3):364–381, 2005.

[133] Y. Wu and J. Li. The design of digital radar receivers. In *Proc. of IEEE National Radar Conference*, pages 207–210, May 1997.

[134] Xilinx. LogiCORE IP DDS Compiler v4.0, Product Specification. http://www.xilinx.com/support/documentation/ip_documentation/dds_ds558.pdf.

[135] H.T. Nicholas H. and Samueli. An analysis of the output spectrum of direct digital frequency synthesizers in the presence of phase-accumulator truncation. In *Proc. of 41st Annual Symposium on Frequency Control*, pages 495–502, 1987.

[136] P. O'Leary and F. Maloberti. A direct-digital synthesizer with improved spectral performance. *IEEE Transactions on Communications*, 39(7):1046–1048, July 1991.

[137] M. J. Flanagan and G. A. Zimmerman. Spur-reduced digital sinusoid synthesis. *IEEE Transactions on Communications*, 43(7):2254–2262, July 1995.

[138] J. E. Volder. The CORDIC trigonometric computing technique. *IRE Transactions on Electronic Computers*, Sept. 1959.

[139] P. D. Welch. The use of fast fourier transform for the estimation of power spectra: A method based on time averaging over short, modified periodograms. *IEEE Trans. Audio Electroacoust.*, 15(2):70–73, June 1967.

[140] J. J. M. Wang, J. Winters, and R. Warner. RFID system with an adaptive array antenna. US Patent, No. 7212116, May 2007.

[141] M. Kim and N. Y. Chong. Direction sensing RFID reader for mobile robot navigation. *IEEE Transactions on Automation Science and Engineering*, 6(1), Jan. 2009.

[142] Y. Zhang, M. G. Amin, and S. Kaushik. Localization and tracking of passive RFID tags based on direction estimation. *International Journal of Antennas and Propagation*, 2007, 2007.

[143] M. J. Abedin and A. S. Mohan. Use of smart antennas for the localization of RFID reader. In *Proc. of the Asia Pacific Microwave Conference*, pages 1036–1039, 2009.

[144] P. Salonen, M. Keskilammi, L. Sydanheimo, and M. Kivikoski. An intelligent 2.45 GHz beam-scanning array for modern RFID reader. In *Proc. of the IEEE International Conference on Phased Array Systems and Technology*, 2000.

[145] J. Heidrich, D. Brenk, J. Essel, G. Fischer, R. Weigel, and S. Schwarzer. Local positioning with passive UHF RFID transponders. In *Proc. of the IEEE MTT-S International Workshop on Wireless Sensing, Local Positioning and RFID*, Cavtat, Croatia, Sept. 2009.

[146] D. Arnitz, K. Witrisal, and U. Muehlmann. Multifrequency continuous-wave radar approach to ranging in passive UHF RFID. *IEEE Transactions on Microwave Theory and Techniques*, 57(5):1398 –1405, may 2009.

[147] R. Langwieser, C. Angerer, A. L. Scholtz, and M. Rupp. Crosstalk and SNR measurements using a multi-antenna RFID reader with active carrier compensation. In *Proc. of the Third International EURASIP Workshop on RFID Technology*, Spain, Sept. 2010.

[148] H. L. Van Trees. *Optimum Array Processing*. Wiley & Sons New York, 2002.

[149] C. Balanis. *Antenna Theory: Analysis and Design*. John Wiley, 1997.

[150] UPM Raflatac, RFID. UPM raflatec dogbone, Feb. 2002. available at:"www.upmraflatac.com".

[151] D. Kim, M. A. Ingram, and W. W. Smith. Measurements of small-scale fading and path loss for long range RF tags. *IEEE Transactions on Antennas and Propagation*, 51(8):1740–1749, Aug. 2003.

[152] A. Lázaro, D. Girbau, and D. Salinas. Radio link budgets for UHF RFID on multipath environments. *IEEE Transactions on Antennas and Propagation*, 57(4):1241–1251, Apr. 2009.

[153] M. V. Bueno Delgado, C. Angerer, J. Vales Alonso, and M. Rupp. Estimation of the tag population with physical layer collision recovery. In *Proc. of the Third International EURASIP Workshop on RFID Technology*, Spain, Sept. 2010.

[154] J. Yu, K. H. Liu, X. Huang, and G. Yan. An anti-collision algorithm based on smart antenna in RFID system. In *Proc. of International Conference on Microwave and Millimeter Wave Technology*, volume 3, pages 1149–1152, Apr. 2008.

[155] J. Lee, T. Kwon, Y. Choi, S. K. Das, and K. Kim. Analysis of RFID anti-collision algorithms using smart antennas. In *Proc. of the International Conference on Embedded Networked Sensor Systems*, Baltimore, USA, 2004.

[156] A. F. Mindikoglu and A. J. van der Veen. Separation of overlapping RFID signals by antenna arrays. In *Proc. of the IEEE International Conference on Acoustics, Speech and Signal Processing, ICASSP 2008*, Apr. 2008.

[157] A-J. van der Veen. Analytical method for blind binary signal separation. *IEEE Transactions on Signal Processing*, 45(4), Apr. 1997.

[158] A. Bletsas, S. Siachalou, and J. N. Sahlos. Anti-collision backscatter sensor networks. *IEEE Transactions on Wireless Communications*, 8(10), Oct. 2009.

[159] N. Abramson. Packet switching with satellites. In *Proc. of the national computer conference and exposition*, New York, USA, June 1973.

[160] P. Patel and J. Holtzman. Analysis of a simple successive interference cancellation scheme in a DS/CDMA system. *IEEE Journal on Selected Areas in Communications*, 12(5):796–807, Jun 1994.

[161] Steven M. Kay. *Fundamentals of Statistical Signal Processing: Estimation Theory*. Prentice Hall, 1993.

[162] G. Golden, G. Foschini, R. Valenzuela, and P. Wolniansky. Detection algorithm and initial laboratory results using V-BLAST space time communication architecture. *Electronic Letters*, 35(1):14–16, Jan. 1999.

[163] J. W. Craig. A new, simple and exact result for calculating the probability of error for two-dimensional signal constellations. In *Proc. of the IEEE Military Communications Conference*, pages 571–575, McLean, VA, 1991.

[164] M. S. Alouini and A. J. Goldsmith. A unified approach for calculating error rates of linearly modulated signals over generalized fading channels. *IEEE Transactions on Communications*, 47(8), Sept. 1999.

[165] J. H. Winters, J. Salz, and R. D. Gitlin. The impact of antenna diversity on the capacity of wireless communication systems. *IEEE Transactions on Communications*, 42(2/3/4), Feb./Mar./Apr. 1994.

[166] D. Gore, R. W. Heath, and A. Paulraj. On performance of the zero forcing receiver in presence of transmit correlation. In *Proc. of the 2002 IEEE International Symposium on Information Theory.*, Lausanne, Switzerland, 2002.